

# Neutral atom dynamics and plasma turbulence in the tokamak periphery

THÈSE N° 7722 (2017)

PRÉSENTÉE LE 30 JUIN 2017  
À LA FACULTÉ DES SCIENCES DE BASE  
SPC - THÉORIE  
PROGRAMME DOCTORAL EN PHYSIQUE

ÉCOLE POLYTECHNIQUE FÉDÉRALE DE LAUSANNE

POUR L'OBTENTION DU GRADE DE DOCTEUR ÈS SCIENCES

PAR

Christoph WERSAL

acceptée sur proposition du jury:

Prof. V. Savona, président du jury  
Prof. P. Ricci, directeur de thèse  
Dr B. LaBombard, rapporteur  
Prof. D. Reiter, rapporteur  
Prof. C. Theiler, rapporteur



ÉCOLE POLYTECHNIQUE  
FÉDÉRALE DE LAUSANNE

Suisse  
2017



# Abstract

Understanding the physical mechanisms at play in the interaction between turbulent plasma and neutral particles is a crucial issue that we approach in this Thesis by using a first-principles self-consistent model of the tokamak periphery implemented in the GBS code. While the plasma is modeled by the drift-reduced two-fluid Braginskii equations, a kinetic model for the neutrals is developed, valid in short and in long mean free path scenarios. The model includes ionization, charge-exchange, recombination, and elastic collisional processes. The neutral kinetic equation is solved by using the method of characteristics.

We identify the key elements determining the interaction between neutrals and the turbulent plasma focusing on a tokamak with a toroidal rail limiter on the high-field side equatorial midplane. For this purpose, we simulate the dynamics of the plasma and the neutrals in a domain that includes both the confined edge region and the scrape-off layer (SOL). It turns out that, in the considered plasma conditions, neither the fluctuations of the neutral moments, nor the friction between neutrals and the plasma impact the time-averaged plasma profiles significantly. Thanks to this study, we derive a simple model for the neutral-plasma interaction, which is helpful to identify and understand the principal physical processes at play in the tokamak periphery.

By studying the dynamics of the neutral-plasma interplay along the magnetic field lines in the SOL, we derive a refined two-point model from the drift-reduced Braginskii equations that balances the parallel and perpendicular transport of plasma and heat, and takes into account the plasma-neutral interaction. The model estimates the electron temperature drop along a field line, from a region far from the limiter to the limiter plates. The refined two-point model is shown to be in very good agreement with the simulation results.

Finally, we self-consistently simulate a diagnostic neutral gas puff, which is often used experimentally as a tool to learn about the turbulence properties in the tokamak periphery. In particular, we investigate the impact of neutral density fluctuations on the  $D_\alpha$  light emission, finding that at a radial distance from the gas puff smaller than the neutral mean free path, neutral density fluctuations are anti-correlated with plasma density, electron temperature, and  $D_\alpha$  fluctuations, while at distances

---

from the gas puff larger than the neutral mean free path, a non-local shadowing effect influences the neutrals, and the  $D_\alpha$  fluctuations are correlated with the neutral density fluctuations.

**Keywords:**

**plasma physics, controlled fusion, scrape-off layer, turbulence, kinetic neutral atom dynamics, fluid simulations, kinetic simulations, drift-reduced Braginskii model, limiter configuration, two-point model, gas puff imaging, neutral fluctuations**

# Zusammenfassung

Das Verständnis der physikalischen Mechanismen im Zusammenspiel von turbulente Plasma und Neutralteilchen ist ein wichtiges Thema, das wir in dieser Dissertation mithilfe eines selbstkonsistenten Modells der Tokamakperipherie angehen. Das Modell ist von physikalischen Grundprinzipien abgeleitet und im GBS-Code implementiert. Das Plasma wird mit den drift-reduzierten Braginskii-Gleichungen zweier Fluide beschrieben. Für die Neutralteilchen entwickeln wir ein kinetisches Modell, anwendbar in Szenarien sowohl mit kurzen als auch mit langen freien Weglängen der Neutralteilchen. Das Modell beschreibt Ionisation, Ladungsaustausch, Rekombination und elastische Kollisionen. Die kinetische Gleichung der Neutralteilchen wird mittels der Methode der Charakteristiken gelöst.

Wir identifizieren die Schlüsselemente der Interaktion zwischen Neutralteilchen und dem turbulenten Plasma in einem Tokamak mit einem toroidalen Begrenzer ("Limiter") auf der hochfeldseitigen äquatorialen Mittelebene. Zu diesem Zweck simulieren wir die Dynamik des Plasmas und der Neutralteilchen sowohl im Randbereich des eingeschlossenen Plasmas als auch in der Abschältschicht ("Scrape-Off-Layer"). Es stellt sich heraus, dass bei den betrachteten Plasmabedingungen weder die Fluktuationen der Neutralteilchen noch die Reibung zwischen Neutralteilchen und dem Plasma die zeitlich gemittelten Plasmaprofile signifikant beeinflussen. Dank dieser Erkenntnisse entwickeln wir ein einfaches Modell für die Interaktion zwischen Neutralteilchen und dem Plasma, das es erleichtert die physikalischen Prozesse in der Tokamakperipherie zu identifizieren und zu verstehen.

Mithilfe der Betrachtung der Wechselwirkung zwischen Neutralteilchen und dem Plasma entlang der Magnetfeldlinien in der Abschältschicht entwickeln wir – ausgehend von den drift-reduzierten Braginskii-Gleichungen – ein verbessertes Zwei-Punkte-Modell, das das Zusammenspiel von parallelem und senkrechtem Transport von Plasmateilchen und Wärme und die Interaktion zwischen Neutralteilchen und dem Plasma beschreibt. Das Modell schätzt die Abnahme der Elektronentemperatur entlang einer magnetischen Feldlinie von einer Region weit entfernt vom Begrenzer zu den Begrenzerplatten ab. Das verbesserte Zwei-Punkte-Modell stimmt sehr gut mit den Simulationsergebnissen überein.

Zuletzt simulieren wir selbstkonsistent einen diagnostischen Neutralteilchen-Gasstoß,

---

der experimentell oft eingesetzt wird um mehr über die Eigenschaften der Turbulenz in der Tokamakperipherie zu erfahren. Wir untersuchen die Auswirkungen der Fluktuationen in der Neutralteilchendichte auf die lokale  $D_\alpha$ -Lichtemission. Es stellt sich heraus, dass in der Nähe des Gasstoßes – bis zu einem radialen Abstand der ungefähr der mittleren freien Weglänge der Neutralteilchen entspricht – die Fluktuationen der Neutralteilchendichte mit den Fluktuationen in Plasmadichte, Elektronentemperatur und  $D_\alpha$ -Emission anti-korreliert sind. In größeren Abständen vom Gasstoß beeinflusst eine nicht-lokale Schattenwirkung die Neutralteilchen und die Fluktuationen der  $D_\alpha$ -Emission sind mit den Fluktuationen der Neutralteilchendichte korreliert.

**Stichwörter:**

**Plasmaphysik, kontrollierte Fusion, Abschältschicht, Turbulenz, kinetische Neutralteilchendynamik, Fluidsimulationen, kinetische Simulationen, drift-reduziertes Braginskii Modell, Limiter, Zwei-Punkt-Modell, Gasstoß-Bildgebung, Neutralteilchen-Fluktuationen**

# Contents

<b>Abstract (English/Deutsch)</b>	<b>i</b>
<b>Contents</b>	<b>v</b>
<b>1 Introduction</b>	<b>1</b>
1.1 Electricity production and fusion . . . . .	1
1.2 The periphery of a tokamak . . . . .	4
1.3 Outline of the present Thesis . . . . .	6
<b>2 A self-consistent model of plasma turbulence and neutral atom dynamics</b>	<b>9</b>
2.1 Introduction . . . . .	10
2.2 The neutral model . . . . .	11
2.3 The plasma model . . . . .	14
2.4 Formal solution of the neutral kinetic equation . . . . .	20
2.5 Numerical implementation . . . . .	26
2.6 First self-consistent plasma turbulence simulations with neutral atom dynamics . . . . .	28
2.7 Convergence properties of the neutral model . . . . .	33
<b>3 Identification of the key elements of the neutral-plasma interaction</b>	<b>39</b>
3.1 Introduction . . . . .	40
3.2 Simulation of the tokamak periphery . . . . .	41
3.3 Fluctuations in the neutral moments . . . . .	46
3.4 The key interaction terms . . . . .	51
3.4.1 Friction interaction terms . . . . .	51
3.4.2 Heat loss and temperature equilibration terms . . . . .	52
3.4.3 Considerations on a simplified neutral model . . . . .	52
3.5 Further considerations . . . . .	53
3.5.1 Averaged plasma-neutral interaction terms . . . . .	53
3.5.2 On the poloidal asymmetry . . . . .	54

## Contents

---

<b>4 Two-point model</b>	<b>57</b>
4.1 Introduction . . . . .	57
4.2 A simple two-point model for the limited SOL . . . . .	59
4.3 Turbulent SOL simulations and comparison with the simple two-point model . . . . .	60
4.4 A refined two-point model for limited SOL . . . . .	61
4.5 Discussion . . . . .	67
<b>5 Gas Puff Imaging</b>	<b>71</b>
5.1 Introduction . . . . .	71
5.2 Simulation and GPI diagnostics . . . . .	73
5.3 Impact of neutral fluctuations on GPI . . . . .	77
5.4 Discussion . . . . .	80
<b>6 Summary and outlook</b>	<b>85</b>
<b>Bibliography</b>	<b>95</b>
<b>Acknowledgements</b>	<b>97</b>
<b>Curriculum Vitae</b>	<b>99</b>



# Chapter 1

## Introduction

### 1.1 Electricity production and fusion

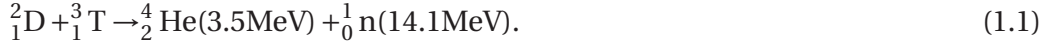
The ever increasing demand for energy is one of the big challenges humanity faces in the 21st century. Currently, electricity accounts for about one quarter of the world's total final energy consumption, and its share is expected to increase significantly in the next decades [1]. While technological advances are increasing the efficiency of electricity usage, they cannot cover its raising demand due to the growing world population and the increasing fraction of people with access to electricity. The demand has to be met under consideration of the power plants' ecological impact, especially the release of carbon-dioxide and air pollutants. While, in principle, a mix of renewable energy sources and nuclear fission power plants could meet the demand for a significantly carbon-dioxide reduced electricity production, the implementation of such an electricity production scenario faces several challenges. Wind and solar electricity production depend on the weather and the regional climate, and they have to be complemented with large energy storage facilities whose development still requires a breakthrough. At the same time, today's nuclear fission power plants produce long-lasting radioactive waste, lack inherent safety against accidents, and increase the availability of potentially dangerous nuclear fission materials, which raises proliferation issues. Furthermore, the amount of nuclear fission fuel available on Earth is limited. The development of a carbon-dioxide-free source of electricity that avoids these issues would be an extremely valuable addition to our capabilities to produce electricity. Fusion power plants may provide this source of energy.

Fusion power plants are expected to use nuclear reactions similar to the ones occurring in the stars, which are their mechanism to release energy. In the stars, hydrogen

## Chapter 1. Introduction

---

nuclei fuse together to form helium (alpha particles) via either the proton-proton chain reaction (dominant in the Sun), or the catalytic carbon-nitrogen-oxygen cycle (dominant in massive stars) [2]. Since both of these processes involve two beta decays (two protons become neutrons), they are very slow and cannot be used in fusion power plants on Earth. The most promising nuclear reaction for fusion power plants is the one between deuterium and tritium,



A large amount of energy (approximately 17.6MeV) is released as kinetic energy of the fusion products in this reaction, with the neutron carrying approximately 80% and the alpha particle approximately 20% of the released energy. Deuterium and tritium energies of the order of 10-100keV are necessary for the reaction to happen, because both nuclei are positively charged and the electrostatic Coulomb repulsion between the two has to be overcome, such that the nuclei can get close enough for the attracting strong nuclear force to dominate. In thermonuclear fusion devices, these high energies are achieved by confining and heating the deuterium-tritium fuel to temperatures of 20-30keV. At this temperature, the fusion fuel is ionized and therefore in the plasma state [3]. While initially the plasma requires external heating sources, it has to self-sustain the high temperature during the steady-state to achieve a positive net energy gain. In the foreseen fusion reactor operation, the produced fast neutrons leave the plasma without interacting and release their kinetic energy to a blanket surrounding the plasma. (The heat is then removed from the blanket and used in conventional steam generators to obtain electricity.) On the other hand, the alpha particles provide the steady-state plasma heating. The condition necessary for a sufficient number of fusion reactions to occur, in order to keep the fusion process going without external heating, is given by the Lawson triple product criterion [4],

$$nT\tau_E \gtrsim 10^{20} \text{ s m}^3 \text{ keV}, \quad (1.2)$$

where  $n$  is the plasma density,  $T$  the plasma temperature, and  $\tau_E$  the energy confinement time (i.e. the ratio between energy loss rate and the total plasma energy).

While several paths are being explored to achieve the condition in Eq. 1.2, currently, the most promising design of a future fusion power plant is based on confining the hot plasma in a toroidal magnetic cage, where on top of a toroidal magnetic field a poloidal component is superimposed, leading to helical magnetic field lines that lie on closed flux-surfaces. In fact, due to the Lorenz force ions and electrons of a plasma gyrate around the magnetic field, and therefore they are confined in the directions perpendicular to it. On the other hand, these particles move freely along the magnetic

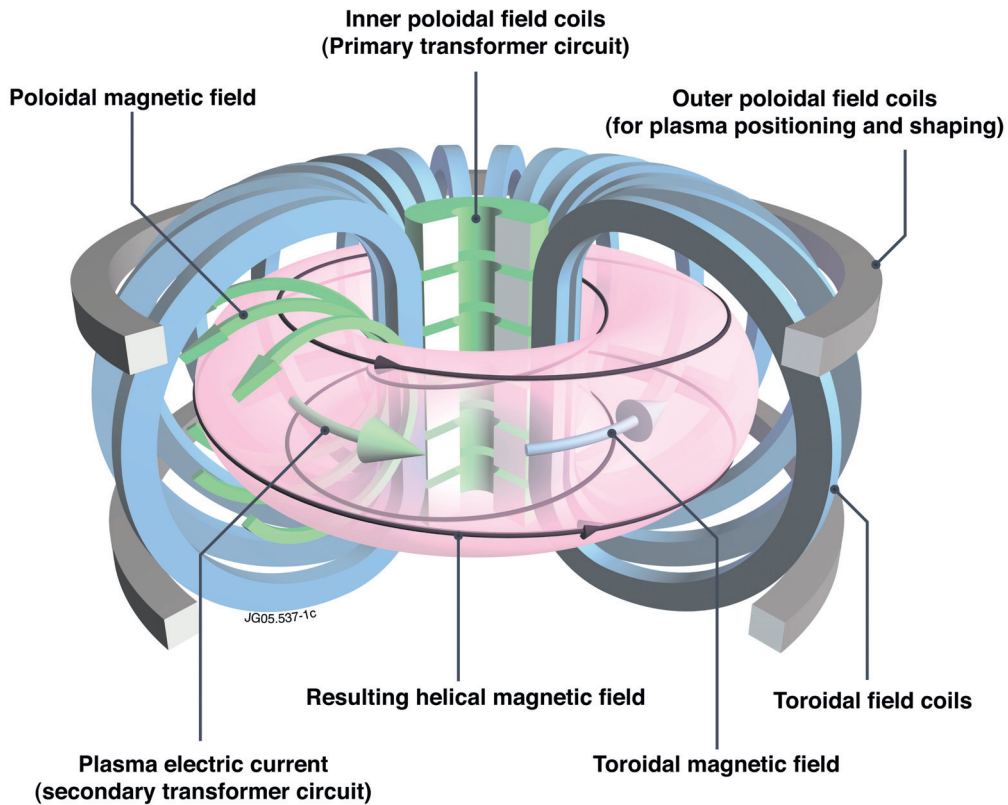


Figure 1.1 – Schematic of a tokamak. The pink volume depicts the hot confined plasma. The blue coils produce the toroidal magnetic field. The green central transformer coil induces the plasma current, which produces the poloidal magnetic field. *Image source: euro-fusion.org*

field lines, which, as a consequence, should not intersect a solid wall. The need of both a toroidal and poloidal component of the magnetic field is due to the fact that charged particles in a purely toroidal magnetic field are not confined, even though the field lines do not intersect a solid wall, because of vertical curvature drifts originating from the magnetic field curvature and gradients [5]. Fusion research has now converged to the development of two devices to confine a hot plasma in such a toroidal magnetic cage: the tokamak [5] and the stellarator [6]. In a stellarator, both field components are created by external magnetic coils, requiring complicated three-dimensionally shaped magnets. In a tokamak, a toroidal plasma current is induced by a central coil, which acts as a primary circuit of a transformer, creating the necessary poloidal component of the magnetic field that is superimposed to a toroidal field, created by a set of poloidal coils. A schematic view of the coils in a tokamak is shown in Fig. 1.1. The present Thesis focuses on the dynamics in the periphery of a tokamak.

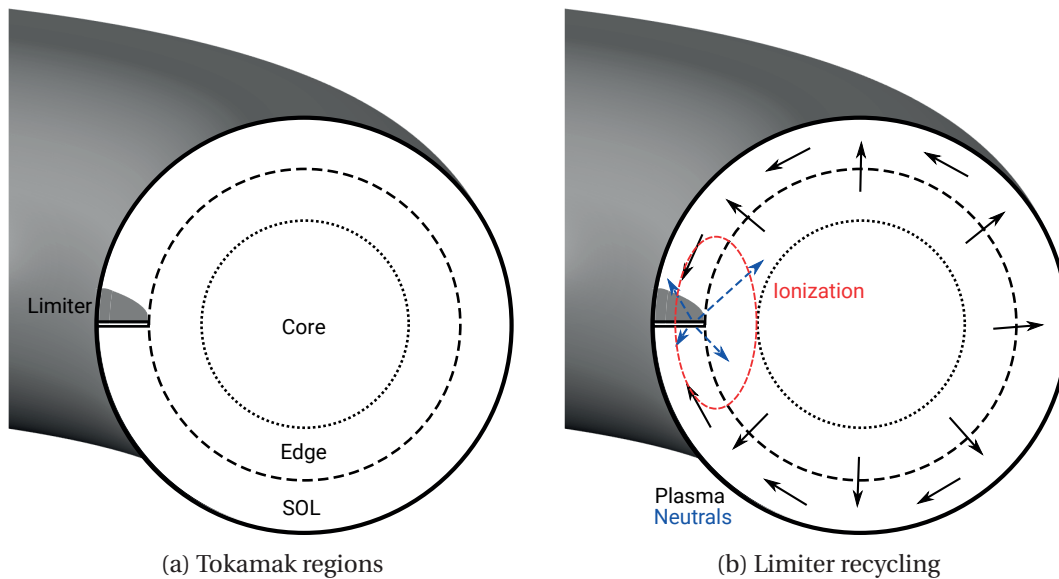


Figure 1.2 – Schematic poloidal cross-section of a tokamak with a toroidal rail limiter on the high-field side midplane. (a) The three main plasma regions, i.e. core, edge, and SOL are indicated. (b) Recycling process: Plasma is transported radially outward from the core and edge into the SOL, where it flows along the field lines to the limiter (black arrows). There, the plasma is recycled and the recycled neutrals (blue arrows) are ionized by the hot plasma (mostly in the red region).

## 1.2 The periphery of a tokamak

Three main plasma regions can be identified in a tokamak, as shown in the schematic poloidal cross-section in Fig. 1.2a. The *core* is the central region where the plasma is far from the wall, hottest and densest, and where the fusion reactions take place. Due to the high temperatures, the collisionality in the core is rather low [7], such that for its description and numerical modeling a kinetic model is necessary. In the core, magnetic field lines lie on toroidal nested closed flux-surfaces. The region that encloses the core is called the *edge* region. In the edge, the field lines also lie on closed flux-surfaces, but the plasma temperature and density decrease rapidly in the direction radially outwards from the core and, in general, the equilibrium gradients become larger than in the core. Since the temperature is lower in the edge than in the core, the collisionality can sometimes be sufficiently high for a fluid description of the plasma dynamics to become applicable. While the separation between the core and edge regions, which form together the *confined* region, is not clearly defined, we will denote as edge region the outermost part of the confined region of the plasma. Finally, the third, outermost, plasma region is called the *Scrape-Off Layer* (SOL). The

SOL is separated from the edge by the last closed flux surface (LCFS or separatrix). In the SOL, the field lines do not lie on closed flux-surfaces, but they intersect the solid walls and, for this reason, they are referred to as *open* field lines. The intersection of the field lines with the solid wall can occur at the main vessel wall, at the surface of a limiter, or at the divertor [8]. A limiter is a structure that is built into the vessel wall to precisely define the extend of the SOL and it can be designed to withstand high heat loads from the plasma, e.g., with active cooling. In Fig. 1.2a a toroidal rail limiter is shown on the high-field side equatorial midplane of the torus. We note that poloidal limiters also exist, and the main wall can be used as a limiter, which is often the case during the initial ramp-up phase in machines that have a divertor, when the magnetic flux-surfaces are pushed against a defined section of the wall [9]. In a diverted plasma, external poloidal magnetic field coils are used to shape the plasma so that the strike points (the points where the LCFS touches the wall) are at a certain distance from the confined plasma region. This is in contrast to the limited configuration, where the strike points are at the limiter corners and, therefore, in direct contact with the confined region (see Fig. 1.2a). The divertor is the part of the vessel wall, typically designed to withstand high heat loads, where the strike points lay. Since it is spatially separated from the confined region, the plasma conditions at the strike points can be very different from the ones in the edge. In fact, it is advantageous to have rather cold plasma in front of the solid wall, since the plasma temperature sets the drop of the electrostatic potential at the wall, which accelerates ions towards the wall [8]. Fast ions lead to sputtering of wall material, and ultimately to impurities in the plasma core and fast degradation of the wall. Since the temperatures in the SOL are lower than in the core and edge regions, the collisionality is higher, and a fluid description of the plasma is often applicable. The SOL and edge regions, together, form the periphery of the fusion plasma.

While single charged particles are well confined by the twisted magnetic field lines, their collective dynamics degrade the confinement. Particles are radially transported due to collisions (classical and neo-classical transport) and due to plasma turbulence, which is driven by steep radial plasma gradients (e.g.,  $T_e \gtrsim 10\text{keV}$  in the core and  $T_e \lesssim 10\text{eV}$  in the far SOL). Despite this, particles still move along the field lines generally much faster than radially. Therefore, ions and electrons that leave the confined region and enter in the SOL region are more likely to arrive at the limiter or divertor by flowing along the field lines, than to travel radially to the main part of the vessel wall. The electrons and ions impacting the solid walls recombine on its surface. The resulting neutral atoms are either reflected following the ion impact, or stick to the wall and combine among themselves to form molecules, which are thermally released from the wall when its surface is saturated. The neutral molecules and atoms are then dissociated and ionized inside the plasma, fueling it. If the ionization takes place

in the SOL, the newly ionized plasma most likely flows back to the wall, where it is recycled again. On the other hand, if the neutrals are ionized in the confined region, the recycled particles can redistribute themselves on the flux-surface before being radially transported out again into the SOL. This recycling process for a tokamak with a toroidal rail limiter on the high-field side midplane is depicted in Fig. 1.2b. In the limited configuration, the strike point, where a large fraction of the recycling occurs, is in direct contact with the confined region, and therefore a large fraction of recycled neutrals are ionized inside the LCFS. In diverted configurations, on the other hand, a large fraction of the recycled neutrals can be ionized close to the strike point in the SOL. In this case, the plasma is said to be in a high-recycling regime.

### 1.3 Outline of the present Thesis

In this Thesis we present the results of our study on the interaction between neutral atom dynamics and turbulent plasma in the tokamak SOL and edge regions. The study was carried out with the three-dimensional turbulence code GBS [10, 11], which evolves the drift-reduced two-fluid Braginskii equations for the plasma, coupled to a kinetic model for the neutral atoms [12].

In Chapter 2 we present the derivation of the model equations, starting from kinetic equations for electrons, ions, and neutral atoms. For the plasma species, we derive a set of fluid equations with the Braginskii closure and apply the drift-reduction valid in typical SOL conditions. The kinetic neutral equation is simplified by assuming simple collision operators and separating time and spatial scales, leading to a formal analytical solution that can be evaluated numerically. We also present numerical convergence test of the solution of the neutral model.

In order to study the importance of the different mechanisms at play in the interaction between neutrals and plasma, in Chapter 3 we present a simulation of the tokamak SOL and edge regions with self-consistent fueling due to neutral gas puffs. We investigate the influence of neutral atom fluctuations on the plasma equilibrium profiles, and we highlight what are the most important terms that set the interaction of the neutrals with the plasma.

In Chapter 4 we present a set of self-consistent turbulence simulations of the tokamak SOL. In these simulations, the plasma density is observed to affect the drop in electron temperature from the low-field side midplane to the region in front of the limiter. We derive a refined two-point model including the neutral-plasma interaction terms as well as the plasma compressibility from the parallel electron heat balance. This model

is in very good agreement with the turbulent simulation results of such an electron temperature drop.

In Chapter 5 we investigate the influence of neutral density fluctuations on  $D_\alpha$  emission, which is often used experimentally to obtain information about plasma turbulence by gas puff imaging (GPI) diagnostics. We include a diagnostic gas puff in a simulation of the tokamak SOL and edge regions to evolve the neutral fluctuations self-consistently with the turbulent plasma structures.

We summarize our findings in Chapter 6 and give an outlook on future work that can be carried out with the neutral atoms model developed in the present Thesis and the GBS code.





## Chapter 2

# A self-consistent model of plasma turbulence and neutral atom dynamics

In this Chapter we present the model that is used throughout this Thesis to simulate the interaction of neutral atom dynamics and plasma turbulence in the tokamak periphery. We also provide a short description of the GBS code that implements this model. The two-fluid drift-reduced Braginskii equations to model plasma turbulence are derived in Refs. [13, 14] and discussed in former publications about the GBS code [10, 11, 15, 16]. The description of the kinetic neutral model and its coupling to the plasma equations is published in Ref. [12]. In fact, this Chapter represents an updated and more detailed version of the model description reported in Ref. [12].

This Chapter is structured as follows. After the Introduction, in Section 2.2 we introduce the model for neutral atoms and in Section 2.3 we introduce the drift-reduced Braginskii equations suitable to describe plasma turbulence in the SOL including the interaction of the plasma with the neutrals. The method to solve the kinetic equation for neutrals is discussed in Section 2.4 and the description of the numerical implementation of the neutral and plasma equations follows in Section 2.5. In Section 2.6, first results of self-consistent simulations of plasma turbulence and neutral dynamics are presented. The numerical convergence properties of the solver are studied in Section 2.7.

### 2.1 Introduction

The first-principles understanding of the processes occurring in the tokamak SOL and edge regions remains an outstanding open issue in the way towards the construction of a fusion reactor. The SOL physics sets the boundary conditions for the plasma core, influencing the performance of the entire device, and it regulates the interaction of the plasma with the solid wall, determining the particle and power flux to the vessel. These have to stay within the material limits to prevent damage to the wall [17, 18].

When ions and electrons outflowing from the SOL impact the solid walls, they recombine and they are re-emitted into the tokamak as neutral atoms and molecules that can penetrate into the SOL and edge region. These recycled neutrals, which interact with the plasma through a number of collisional processes, play an important role in the SOL dynamics, and in regulating the heat and particle flux to the first wall.

To study the interplay between the neutral and the plasma dynamics in the tokamak periphery, plasma simulation codes based on phenomenological models for the turbulent transport are coupled to kinetic Monte Carlo codes that describe the behavior of the neutrals in the SOL (e.g., EIRENE [19, 20], DEGAS 2 [21], NIMBUS [22], and others). The resulting codes (e.g., SOLEDGE2D-EIRENE [23], SOLPS, formerly B2-EIRENE, [24, 25, 20], EMC3-EIRENE [26], UEDGE [27], and others) are the tool of reference for the design of tokamak divertors and they have been used for the ITER divertor [28]. Fluid descriptions of the neutrals were also developed for plasma transport codes [27, 29, 30], which are applicable in cases where the distribution function of the neutrals is close to a Maxwellian through a high collisionality of the neutrals. It was shown that fluid neutral models give similar results as kinetic simulations in some scenarios (e.g., in the detachment regime inside a divertor leg [31]).

Only recently, attempts have been made to include the neutral dynamics in today's SOL codes that are derived from first-principles, i.e., that do not make use of empirical models or experimentally fitted parameters to describe SOL turbulence, such as BOUT++ [32], GBS [10, 11] TOKAM3X [33], HESEL [34], and GRILLIX [35]. In the two-dimensional turbulence simulation code TOKAM2D [36], the ionization of mono-energetic neutrals flying along the radial direction is self-consistently described within a plasma model that evolves the plasma density and the electrostatic potential. Within a simple two-dimensional fluid plasma description, the use of a fluid neutral model was recently reported [37]. A fluid-diffusive neutral model was also developed for BOUT++, being applied to study the interaction of neutrals with three-dimensional plasma turbulence in a linear device [38], and for the two-dimensional HESEL code [39]. The coupling of both BOUT++ and TOKAM3X with the kinetic

EIRENE Monte Carlo code for neutral particles is being attempted.

In the present Thesis, we introduce a kinetic model for neutral atoms in the tokamak periphery, self-consistently evolved with the drift-reduced Braginskii equations [13, 14] that describe the plasma dynamics in typical SOL conditions. The neutral kinetic model allows us to consider both short and long neutral mean free paths. We consider one mono-atomic neutral species, which is subject to four effective collision processes: charge-exchange (that includes elastic ion-neutral collisions), ionization, recombination, and elastic electron-neutral collisions. Although they may become important in detached scenarios, we neglect neutral-neutral collisions, which have a lower reaction rate than charge-exchange and ionization processes in the typical attached SOL parameter regime. We note that additional neutral species, such as molecules, can be included using the same model presented in this Thesis - this might become necessary to consider detachment conditions, or to include the details of the recycling from the main vessel wall.

The model is implemented and numerically solved within the GBS code [10, 11], a three-dimensional numerical code developed to simulate SOL plasma turbulence. By solving the drift-reduced Braginskii equations coupled to the kinetic neutral atom equation, GBS evolves the full plasma and neutral profiles without separation into an equilibrium and fluctuating part, enabling the study of the self-consistent formation of the plasma profiles as the interplay of the plasma outflowing from the core, turbulent transport, the parallel flow towards the limiter, the sheath losses, and the plasma recycling and the neutrals' ionization. GBS uses a proper set of boundary conditions at the presheath entrance [40], and it is able to treat electromagnetic perturbations [41].

## 2.2 The neutral model

We describe the dynamics of the distribution function of a single mono-atomic neutral species,  $f_n$ , by using the following kinetic equation

$$\frac{\partial f_n}{\partial t} + \mathbf{v} \cdot \frac{\partial f_n}{\partial \mathbf{x}} = -v_{iz} f_n - v_{cx} \left( f_n - \frac{n_n}{n_i} f_i \right) + v_{rec} f_i \quad (2.1)$$

being  $f_i$ ,  $n_n$ , and  $n_i$  the ion distribution function, the neutral density, and the ion density, respectively. The ionization, charge-exchange, and recombination processes are described, respectively, through the use of Krook operators with collision frequencies

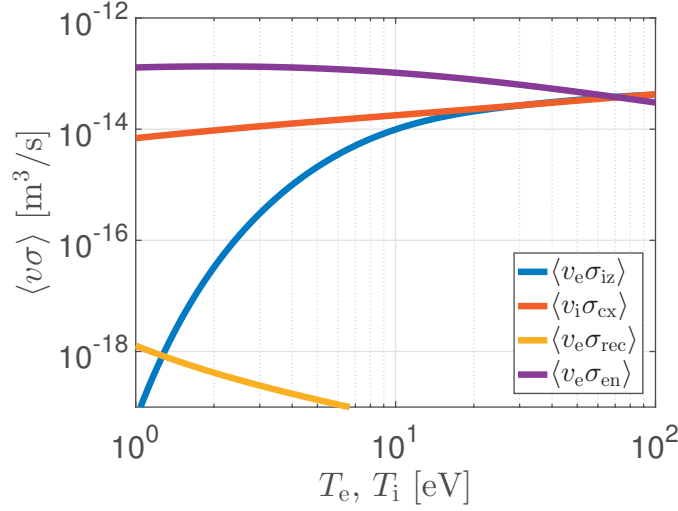


Figure 2.1 – The values of the collision rates,  $\langle v\sigma \rangle_v$ , for ionization, charge-exchange, recombination, and elastic electron-neutral collisions for  $n_0 = 5 \cdot 10^{19} \text{m}^{-3}$ .

defined as

$$v_{iz} = n_e \langle v_e \sigma_{iz}(v_e) \rangle_v \quad (2.2)$$

$$v_{rec} = n_e \langle v_e \sigma_{rec}(v_e) \rangle_v \quad (2.3)$$

$$v_{cx} = n_i \langle v_i \sigma_{cx}(v_i) \rangle_v \quad (2.4)$$

where  $\sigma_{iz}$ ,  $\sigma_{rec}$ , and  $\sigma_{cx}$  are the ionization, recombination, and charge-exchange cross-sections, and  $v_e$  and  $v_i$  are the electron and ion velocities. The collision frequencies,  $v_{iz}$  and  $v_{rec}$ , result from the averaging over the electron distribution function, neglecting therefore the neutral atom velocity, with respect to the electron one, in the evaluation of the relative velocity between the colliding particles. Regarding the charge-exchange collision frequency,  $v_{cx}$ , we note that it depends weakly on the relative velocity between neutrals and ions [8], thus we neglect the neutral velocity in Eq. (2.4) when evaluating the relative velocity of the colliding particles, and we average the cross-section over the ion distribution function. The elastic electron-neutral collisions are neglected in the neutral equation, because of the electron to neutral mass ratio. In the present work, we use effective reaction rates for the ionization, charge-exchange, and recombination  $\langle v\sigma \rangle_v$  terms, which are taken from the OpenADAS<sup>1</sup> database, where they have been calculated using a collisional-radiative model [42]. The cross-sections for the elastic electron-neutral collisions are taken from Ref. [43]. The values of the collision rates,  $\langle v\sigma \rangle_v$ , used in this work are shown in Fig. 2.1 and Table 2.1.

<sup>1</sup>OpenADAS - <http://open.adas.ac.uk>

$T_e, T_i$ [eV]	1	10	100
$\langle \nu_e \sigma_{iz} \rangle$ [m <sup>3</sup> /s]	$5.97 \cdot 10^{-20}$	$9.88 \cdot 10^{-15}$	$4.17 \cdot 10^{-14}$
$\langle \nu_i \sigma_{cx} \rangle$ [m <sup>3</sup> /s]	$6.90 \cdot 10^{-15}$	$1.78 \cdot 10^{-14}$	$4.23 \cdot 10^{-14}$
$\langle \nu_e \sigma_{rec} \rangle$ [m <sup>3</sup> /s]	$1.28 \cdot 10^{-18}$	$6.57 \cdot 10^{-20}$	$5.99 \cdot 10^{-21}$
$\langle \nu_e \sigma_{en} \rangle$ [m <sup>3</sup> /s]	$1.29 \cdot 10^{-13}$	$1.03 \cdot 10^{-13}$	$3.01 \cdot 10^{-14}$

Table 2.1 – The values of the collision rates,  $\langle \nu \sigma \rangle_\nu$ , for ionization, charge-exchange, recombination, and elastic electron-neutral collisions for  $n_0 = 5 \cdot 10^{19} m^{-3}$ .

Since Eq. (2.1) has to be solved in the bounded domain of the tokamak periphery, we now describe its boundary conditions. Being a kinetic advection equation, the boundary conditions for  $f_n$  have to be specified for the inward pointing velocities, that is for  $\mathbf{v}$  such that  $\nu_p = \mathbf{v} \cdot \hat{\mathbf{n}} > 0$ , with  $\hat{\mathbf{n}}$  the normal vector perpendicular to the boundary and pointing into the plasma region. At the limiter or divertor plates, the boundary of the domain over which Eq. (2.1) is solved coincides with the wall. We assume that the wall is saturated, i.e. that all impacting particles, neutrals and ions, are re-emitted from the wall instantly. A fraction of the particles impacting the wall,  $\alpha_{\text{refl}}$ , is reflected as neutrals, the rest is absorbed and released, again as neutrals, with a velocity that depends on the wall properties and that is independent of the impacting velocities. The parameter  $\alpha_{\text{refl}}$  depends on the wall material and the SOL conditions (see, e.g, page 113 in Ref. [8]). We assume  $\alpha_{\text{refl}} = 0.8$  for both neutrals and ions in the simulations in this Thesis. The distribution function of the inflowing neutrals,  $\nu_p > 0$ , is therefore

$$f_n(\mathbf{x}_b, \mathbf{v}) = (1 - \alpha_{\text{refl}}) \Gamma_{\text{out}}(\mathbf{x}_b) \chi_{\text{in}}(\mathbf{x}_b, \mathbf{v}) + \alpha_{\text{refl}} [f_n(\mathbf{x}_b, \mathbf{v} - 2\mathbf{v}_p) + f_i(\mathbf{x}_b, \mathbf{v} - 2\mathbf{v}_p)], \quad (2.5)$$

where  $\mathbf{x}_b$  is the vector position of a point on the boundary, specifically on the limiter or divertor plates in this case, and  $\Gamma_{\text{out}} = \int_{\nu_p < 0} |\nu_p| f_n d\nu^3 + \Gamma_{\text{out},i}$  the flux of ions and neutrals outflowing towards the limiter or divertor plates. In particular,  $\Gamma_{\text{out},i}$  is the outflowing perpendicular ion flux, where we only include the perpendicular part of the parallel ion flow and neglect ion drifts, and  $\mathbf{v}_p = \nu_p \hat{\mathbf{n}}$  is the perpendicular neutral velocity with respect to the boundary. For the reflected part of the inflowing neutral distribution, we use spectral reflexion at the magnetic pre-sheath entrance. In particular, for simplicity, we neglect the acceleration of the ions in the sheath, and we assume unitary energy reflection coefficients (see, e.g., Eq. (3.2) in Ref. [8]). We note that these assumptions can be replaced in future efforts with a kinetic model of the ions in the sheath (see, e.g., Ref. [44]), which might be necessary for quantitative comparison to experimental results. The inflowing velocity distribution,  $\chi_{\text{in}}$ , is set

according to the Knudsen Cosine Law [45] to

$$\chi_{\text{in}}(\mathbf{x}_b, \mathbf{v}) = \frac{3}{4\pi} \frac{m^2}{T_b^2} \cos(\theta) \exp\left(-\frac{mv^2}{2T_b}\right), \quad (2.6)$$

being  $\theta = \arccos(\hat{\mathbf{\Omega}} \cdot \hat{\mathbf{n}})$ ,  $\hat{\mathbf{\Omega}} = \mathbf{v}/v$ , and  $T_b$  the temperature of the inflowing neutrals from the boundary. Often, we use  $T_b = 3\text{eV}$  to mimic typical energies of neutral atoms after Frank-Condon dissociation [46, 8, 47]. The function  $\chi_{\text{in}}$  satisfies the property  $\int_{v_p > 0} v_p \chi_{\text{in}} d^3v = 1$ .

For the sake of simplicity, we place the outer boundary of the computational domain between the LCFS and the vessel wall. We remark that this boundary does not coincide with a physical surface. Particles that flow out through this boundary therefore travel towards the outer vessel wall, impact it, recycle, and then they re-enter the simulation domain. As particles can spread while moving towards the outer vessel wall and re-entering the domain, we evaluate the inflowing distribution function of the neutral atoms by using a local averaging procedure to redistribute the particles outflowing through the surface  $S$  that surrounds the position  $\mathbf{x}_b$  as

$$f_n(\mathbf{x}_b, \mathbf{v}) = \frac{\chi_{\text{in}}(\mathbf{x}_b, \mathbf{v})}{S} \int_S \Gamma_{\text{out}} dS \quad (2.7)$$

for  $\mathbf{v}$  such that  $v_p > 0$ . The surface  $S$  can depend on  $\mathbf{x}_b$ . We remark that, as at the limiter, we neglect ion drifts at the outer boundary in the current implementation of the boundary conditions.

At the boundary towards the tokamak core, we assume that no neutral atoms enter the tokamak periphery, thus  $f_n(\mathbf{x}_b, \mathbf{v}) = 0$  for  $\mathbf{v}$  such that  $v_p > 0$ . Neutral atoms outflowing from the periphery into the core are assumed to be ionized therein, and the ionized plasma is modeled by a source of plasma density at the boundary towards the core (see Section 2.3).

### 2.3 The plasma model

For simplicity, we consider a single ion species plasma. We start our derivation of the drift-reduced Braginskii equations from the kinetic Boltzmann equation of ions and electrons, where we include collision terms in the form of Krook operators to describe the interaction with the neutrals. For the ion species we consider ionization, recombination, and charge-exchange processes, while for the electrons, we consider ionization, recombination, and elastic collision processes. Therefore, the kinetic

equation for the ions is

$$\frac{\partial f_i}{\partial t} + \mathbf{v} \cdot \frac{\partial f_i}{\partial \mathbf{x}} + \mathbf{a} \cdot \frac{\partial f_i}{\partial \mathbf{v}} = \nu_{iz} f_n - \nu_{cx} \left( \frac{n_n}{n_i} f_i - f_n \right) - \nu_{rec} f_i + C_i(f_i, f_e), \quad (2.8)$$

while the kinetic equation for the electrons is

$$\begin{aligned} \frac{\partial f_e}{\partial t} + \mathbf{v} \cdot \frac{\partial f_e}{\partial \mathbf{x}} + \mathbf{a} \cdot \frac{\partial f_e}{\partial \mathbf{v}} = & \nu_{iz} n_n \left[ 2\Phi_e(\mathbf{v}_n, T_{e,iz}) - \frac{f_e}{n_e} \right] \\ & + \nu_{en} n_n \left[ \Phi_e(\mathbf{v}_n, T_{e,en}) - \frac{f_e}{n_e} \right] - \nu_{rec} f_e + C_e(f_e, f_i), \end{aligned} \quad (2.9)$$

where  $\mathbf{a}$  is the particle acceleration due to the Lorentz force,  $\Phi_e(\mathbf{v}, T)$  is a Maxwellian velocity distribution function for electrons,  $C_i(f_i, f_e)$  and  $C_e(f_e, f_i)$  are the Coulomb collision operators including both inter- and intra-species collisions for ions and electrons respectively, and the elastic electron-neutral collision frequency is  $\nu_{en} = n_e \langle \nu_e \sigma_{en}(\nu_e) \rangle \nu$ .

While the interpretation of the collision terms in the ion kinetic equation is straightforward, as they correspond (with opposite sign) to those of the neutral equation, Eq. (2.1), the collision operators in the electron kinetic equation deserve a longer discussion. When a neutral atom is ionized, the impacting fast electron is removed from the system, while two slower electrons appear. As a Krook collision term is used in Eq. (2.9), the loss rate of the fast electrons is proportional to the electron distribution function. Although it is not taken into account that the two resulting electrons might be emitted according to different distribution functions, the model can be reliably used to derive a fluid plasma description, as we do in the following. The two lower-energy electrons appear with a Maxwellian distribution function,  $\Phi_e(\mathbf{v}_n, T_{e,iz})$ , of average velocity  $\mathbf{v}_n = \int \mathbf{v} f_n d\mathbf{v} / \int f_n d\mathbf{v}$  and temperature  $T_{e,iz} = T_e/2 - E_{iz}/3 + m_e \nu_e^2/6 - m_e v_n^2/3$ , where  $T_e$  and  $\nu_e$  are the local electron temperature and fluid velocity respectively. This is deduced by assuming that the electrons are released isotropically in the neutrals' frame of reference, and that the total electron kinetic energy is reduced by the effective ionization energy,  $E_{iz}$ , when an ionization process occurs. We note that the ionization term in Eq. (2.9) takes into account the different paths to ionization (direct or through excited states), by using an effective ionization coefficient. (We also note that  $T_{e,iz}$  can formally become negative, since the finite electron energy threshold for ionization processes is included inside the averaged collisionality  $\nu_{iz}$ . This means that fast and slow electrons have the same probability of ionizing neutral atoms in our simplified description. For low electron temperatures  $\nu_{iz}$  vanishes, which prevents negative electron temperatures in the fluid model that is derived in the following.)

The electron-neutral collisions are modeled in Eq. (2.9) through a loss term pro-

## Chapter 2. Model

---

portional to the electron distribution function and a source with a Maxwellian distribution,  $\Phi_e(\mathbf{v}_n, T_{e,en})$ . In fact, similarly to the ionization process, we impose that the electrons are scattered isotropically in the neutrals' frame of reference. Moreover, assuming that during the elastic electron-neutral collisions the electron kinetic energy is conserved during collisions with much heavier neutrals, one obtains  $T_{e,en} = T_e + m_e(v_e^2 - v_n^2)/3$ . We note that the electron-neutral elastic collision term is neglected in the neutral kinetic equation, Eq. (2.1), because of the small electron to neutral mass ratio.

Following the work of Braginskii [13], we now take the first three moments of the electron and ion kinetic equations, Eqs. (2.8) and (2.9), in the limit  $\omega_c \tau \gg 1$ , where  $\omega_c = qB/m$  is the gyro-frequency and  $\tau$  the typical Coulomb collision time, and with the assumption  $\lambda_{\text{mfp}}/L \ll 1$ , where  $\lambda_{\text{mfp}}$  is the mean free path, and  $L$  the characteristic length of the field lines. In typical SOL conditions, the ion-neutral and electron-neutral collision time is much larger than the electron and ion Coulomb collision time, thus the presence of these collisions does not affect the closure derived in Ref. [13]. In the case of high ion-neutral collisionality,  $\omega_{ci}\tau_{i-n} \leq 1$ , the closure terms have been derived by Helander et al. in Ref. [48].

The Braginskii equations for the electron and ion densities, fluid velocities, and temperatures, derived in Ref. [13], including the additional plasma-neutral interaction terms are

$$\frac{\partial n_e}{\partial t} + \nabla \cdot (n_e \mathbf{v}_e) = n_n v_{iz} - n_i v_{rec} \quad (2.10)$$

$$\frac{\partial n_i}{\partial t} + \nabla \cdot (n_i \mathbf{v}_i) = n_n v_{iz} - n_i v_{rec} \quad (2.11)$$

$$m_e n_e \frac{d_e v_{e\alpha}}{dt} = -\frac{\partial p_e}{\partial x_\beta} - \frac{\partial \Pi_{e\alpha\beta}}{\partial x_\beta} - e n_e [E_\alpha + (\mathbf{v}_e \times \mathbf{B})_\alpha] + R_\alpha + m_e n_n (v_{en} + 2v_{iz})(v_{n\alpha} - v_{e\alpha}) \quad (2.12)$$

$$m_i n_i \frac{d_i v_{i\alpha}}{dt} = -\frac{\partial p_i}{\partial x_\beta} - \frac{\partial \Pi_{i\alpha\beta}}{\partial x_\beta} + Z e n_i [E_\alpha + (\mathbf{v}_i \times \mathbf{B})_\alpha] - R_\alpha + m_i n_n (v_{iz} + v_{cx})(v_{n\alpha} - v_{i\alpha}) \quad (2.13)$$

$$\begin{aligned} \frac{3}{2} n_e \frac{d_e T_e}{dt} + p_e \nabla \cdot \mathbf{v}_e = & -\nabla \cdot \mathbf{q}_e - \Pi_{e\alpha\beta} \frac{\partial v_{e\alpha}}{\partial x_\beta} + Q_e \\ & + n_n v_{iz} \left[ -E_{iz} - \frac{3}{2} T_e + \frac{3}{2} m_e \mathbf{v}_e \cdot \left( \mathbf{v}_e - \frac{4}{3} \mathbf{v}_n \right) \right] \\ & - n_n v_{en} m_e \mathbf{v}_e \cdot (\mathbf{v}_n - \mathbf{v}_e) \end{aligned} \quad (2.14)$$



$$\begin{aligned} \frac{3}{2} n_i \frac{d_i T_i}{dt} + p_i \nabla \cdot \mathbf{v}_i = & -\nabla \cdot \mathbf{q}_i - \Pi_{i\alpha\beta} \frac{\partial v_{i\alpha}}{\partial x_\beta} + Q_i \\ & + n_n (v_{iz} + v_{cx}) \left[ \frac{3}{2} (T_n - T_i) + \frac{m_i}{2} (\mathbf{v}_n - \mathbf{v}_i)^2 \right] \end{aligned} \quad (2.15)$$

where  $\Pi_{\alpha\beta}$  is the  $\alpha\beta$  component of the stress tensor,  $\mathbf{R}$  is the friction force between electrons and ions,  $p$  is the pressure,  $\mathbf{q}$  is the heat flux density,  $Q$  is the heat generated by Coulomb collisions,  $Z$  is the ion charge,  $\mathbf{E}$  and  $\mathbf{B}$  are the electric and magnetic fields,  $d_e/dt = \partial/\partial t + (\mathbf{v}_e \cdot \nabla)$  and  $d_i/dt = \partial/\partial t + (\mathbf{v}_i \cdot \nabla)$  are the electron and ion advective derivatives, and the subscripts e and i stand for electrons and the ion species respectively. The detailed definitions of all fluid quantities can be found in the paper by Braginskii [13].

Despite their simplicity with respect to the kinetic equations, Braginskii's equations, Eqs. (2.10)-(2.15), are not yet suitable to describe the plasma turbulence in the SOL, mainly due to the high computational cost of numerically resolving the electron cyclotron motion. Therefore, we simplify the Braginskii equations in the drift limit, observing that  $d/dt \ll \omega_{ci}$  for typical SOL turbulence. We follow the procedure described by, e.g., Zeiler [14].

To obtain the perpendicular ion velocity, we cross the ion momentum equation, Eq. (2.13), with  $\mathbf{B}$  and rearrange the terms according to their order, writing  $\mathbf{v}_{\perp i} = \mathbf{v}_{\perp i0} + \mathbf{v}_{i-n} + \mathbf{v}_{\text{pol}}$ . The leading order term  $\mathbf{v}_{\perp i0} = \mathbf{v}_E + \mathbf{v}_{\text{di}}$  is the sum of the  $\mathbf{E} \times \mathbf{B}$  drift,  $\mathbf{v}_E = (\mathbf{E} \times \mathbf{B})/B^2$ , and the diamagnetic drift,  $\mathbf{v}_{\text{di}} = (\mathbf{B} \times \nabla p_i)/(enB^2)$ , where we assume quasi-neutrality,  $n_i = n_e = n$ , and  $Z = 1$ . The drift arising from ion-neutral friction due to charge-exchange and elastic collisions,  $\mathbf{v}_{i-n} = (n_n/n)(v_{cx}/\omega_{ci})(\mathbf{v}_{\perp n} - \mathbf{v}_{\perp i}) \times \hat{\mathbf{b}}$ , and the polarization drift,  $\mathbf{v}_{\text{pol}}$ , due to the ion inertia [14], are assumed to be of higher order in  $(1/\omega_{ci})d/dt$  with respect to  $\mathbf{v}_{\perp i0}$ . While the ordering and the expression of  $\mathbf{v}_{\text{pol}}$  have been discussed in detail by many authors (see, e.g., Ref. [14]), we note that  $v_{i-n}$  is much smaller than the leading order term  $v_{\perp i0}$ , as  $v_{i-n} \lesssim v_{\perp i} v_{cx}/\omega_{ci} \ll v_{\perp i0}$  in typical SOL conditions, where we assume that  $v_{cx} \ll \omega_{ci}$  and  $v_{\perp n} \lesssim v_{\perp i}$ . On the other hand, applying the same procedure to the electron momentum equation, Eq. (2.12), leads to  $\mathbf{v}_{\perp e} = \mathbf{v}_E + \mathbf{v}_{\text{de}}$ , with  $\mathbf{v}_{\text{de}} = -(\mathbf{B} \times \nabla p_e)/(enB^2)$ , where the terms proportional to  $m_e$  are neglected.

## Chapter 2. Model

The resulting drift-reduced Braginskii equations in the electrostatic limit are

$$\frac{\partial n}{\partial t} = -\frac{1}{B}[\phi, n] - \nabla_{\parallel}(n v_{\parallel e}) + \frac{2}{eB}[C(p_e) - enC(\phi)] + \mathcal{D}_n(n) + S_n + n_n v_{iz} - n v_{rec} \quad (2.16)$$

$$\frac{\partial \tilde{\omega}}{\partial t} = -\frac{1}{B}[\phi, \tilde{\omega}] - v_{\parallel i} \nabla_{\parallel} \tilde{\omega} + \frac{B^2}{m_i n} \nabla_{\parallel} j_{\parallel} + \frac{2B}{m_i n} C(p) + \frac{B}{3m_i n} C(G_i) + \mathcal{D}_{\tilde{\omega}}(\tilde{\omega}) - \frac{n_n}{n} v_{cx} \tilde{\omega} \quad (2.17)$$

$$\frac{\partial v_{\parallel e}}{\partial t} = -\frac{1}{B}[\phi, v_{\parallel e}] - v_{\parallel e} \nabla_{\parallel} v_{\parallel e} + \frac{e}{\sigma_{\parallel} m_e} j_{\parallel} + \frac{e}{m_e} \nabla_{\parallel} \phi - \frac{T_e}{m_e n} \nabla_{\parallel} n - \frac{1.71}{m_e} \nabla_{\parallel} T_e - \frac{2}{3m_e n} \nabla_{\parallel} G_e + \mathcal{D}_{v_{\parallel e}}(v_{\parallel e}) + \frac{n_n}{n} (v_{en} + 2v_{iz})(v_{\parallel n} - v_{\parallel e}) \quad (2.18)$$

$$\frac{\partial v_{\parallel i}}{\partial t} = -\frac{1}{B}[\phi, v_{\parallel i}] - v_{\parallel i} \nabla_{\parallel} v_{\parallel i} - \frac{1}{m_i n} \nabla_{\parallel} p - \frac{2}{3m_i n} \nabla_{\parallel} G_i + \mathcal{D}_{v_{\parallel i}}(v_{\parallel i}) + \frac{n_n}{n} (v_{iz} + v_{cx})(v_{\parallel n} - v_{\parallel i}) \quad (2.19)$$

$$\frac{\partial T_e}{\partial t} = -\frac{1}{B}[\phi, T_e] - v_{\parallel e} \nabla_{\parallel} T_e + \frac{4T_e}{3eB} \left[ \frac{T_e}{n} C(n) + \frac{7}{2} C(T_e) - eC(\phi) \right] + \frac{2T_e}{3n} \left[ \frac{0.71}{e} \nabla_{\parallel} j_{\parallel} - n \nabla_{\parallel} v_{\parallel e} \right] + \mathcal{D}_{T_e}(T_e) + \kappa_{\parallel e} \nabla_{\parallel} (T_e^{5/2} \nabla_{\parallel} T_e) + S_{T_e} + \frac{n_n}{n} v_{iz} \left[ -\frac{2}{3} E_{iz} - T_e + m_e v_{\parallel e} \left( v_{\parallel e} - \frac{4}{3} v_{\parallel n} \right) \right] - \frac{n_n}{n} v_{en} m_e \frac{2}{3} v_{\parallel e} (v_{\parallel n} - v_{\parallel e}) \quad (2.20)$$

$$\frac{\partial T_i}{\partial t} = -\frac{1}{B}[\phi, T_i] - v_{\parallel i} \nabla_{\parallel} T_i + \frac{4T_i}{3eB} \left[ C(T_e) + \frac{T_e}{n} C(n) - \frac{5}{2} C(T_i) - eC(\phi) \right] + \frac{2T_i}{3n} \left[ \frac{1}{e} \nabla_{\parallel} j_{\parallel} - n \nabla_{\parallel} v_{\parallel i} \right] + \mathcal{D}_{T_i}(T_i) + \kappa_{\parallel i} \nabla_{\parallel} (T_i^{5/2} \nabla_{\parallel} T_i) + S_{T_i} + \frac{n_n}{n} (v_{iz} + v_{cx}) \left[ T_n - T_i + \frac{1}{3} (v_{\parallel n} - v_{\parallel i})^2 \right] \quad (2.21)$$

with  $p = n(T_e + T_i)$ , the total pressure,  $j_{\parallel} = en(v_{\parallel i} - v_{\parallel e})$  the parallel current,  $\kappa_{\parallel e}$  and  $\kappa_{\parallel i}$  the Spitzer heat conduction coefficients, and  $\sigma_{\parallel} = 1.96e^2 n \tau_e / m_e$ , the parallel conductivity, where  $\tau_e$  is the electron collision time. The gyro-viscous contributions are included through the terms  $G_i = -\eta_{0i}[2\nabla_{\parallel} v_{\parallel i} + C(p_i)/(enB) + C(\phi)/B]$  and  $G_e = -\eta_{0e}[2\nabla_{\parallel} v_{\parallel e} - C(p_e)/(enB) + C(\phi)/B]$ , where  $\eta_{0i}$  and  $\eta_{0e}$  are the gyro-viscous coefficients [13]. The source terms ( $S_n$ ,  $S_{T_e}$ ,  $S_{T_i}$ ) mimic the outflow of hot plasma from the confined region to the SOL. The small perpendicular diffusion terms,  $\mathcal{D}_A(A) = D_A \nabla_{\perp}^2 A$ , with the diffusivity  $D_A$ , are included mainly for numerical reasons. The generalized vorticity,  $\tilde{\omega} = \omega + 1/e \nabla_{\perp}^2 T_i$ , is related to the electrostatic potential by  $\nabla_{\perp}^2 \phi = \omega$ , where we use the Boussinesq approximation. The following operators are introduced:  $\nabla_{\parallel} A = \hat{\mathbf{b}} \cdot \nabla A$ ,  $[A_1, A_2] = \hat{\mathbf{b}} \cdot (\nabla A_1 \times \nabla A_2)$ , and  $C(A) = B/2[\nabla \times (\hat{\mathbf{b}}/B)] \cdot \nabla A$ , with  $\hat{\mathbf{b}} = \mathbf{B}/B$ . In this work, we solve the electrostatic equations for circular magnetic flux surfaces in

the large aspect ratio limit,  $\epsilon = a_0/R_0 \simeq 0$ , where  $a_0$  and  $R_0$  are the minor and major radius. The effects of finite aspect ratio on the presented equations were previously discussed in Ref. [49], and the electromagnetic effects in Ref. [41].

We note that the density equation, Eq. (2.16) is derived from the electron density equation, Eq. (2.10), and that the vorticity equation, Eq. (2.17), is obtained by subtracting Eq. (2.10) from Eq. (2.11), applying quasi-neutrality,  $n_i = n_e = n$ , and using the Boussinesq-approximation. The term resulting from the ion-neutral friction drift in Eq. (2.17) has been evaluated by approximating  $\mathbf{v}_{i-n} \simeq (n_n/n)(v_{cx}/\omega_{ci})(\mathbf{v}_{\perp n} - \mathbf{v}_{\perp i0}) \times \hat{\mathbf{b}}$  and assuming  $\nabla \cdot \mathbf{v}_{\perp n} \ll \nabla \cdot \mathbf{v}_{\perp i0}$ , which is true for  $\rho_{s0}/\lambda_{mfp,n} \ll 1$ . ( $\rho_{s0} = c_{s0}/\omega_{ci}$  is the ion sound Larmor radius,  $c_{s0} = \sqrt{T_{e0}/m_i}$  is the plasma sound speed,  $T_{e0}$  is the electron temperature at the LCFS, and  $\lambda_{mfp,n}$  is the mean free path of the neutrals.) The contribution of the electron-neutral friction drift in the vorticity equation, Eq. (2.17), has been neglected due to the small electron to ion mass ratio. We remark that we neglect  $\mathbf{v}_{pol}$  and  $\mathbf{v}_{i-n}$  in the advective derivative  $d/dt$ . We also remark that, for simplicity, we neglect the collisional heat transfer between electrons and ions and the ohmic heating from plasma currents in the  $Q_i$  and  $Q_e$  terms due to the small electron to ion mass ratio. This assumption might have to be removed in future efforts for quantitative comparison to experimental results, especially in high density scenarios. It has been verified *a posteriori* (using the simulation discussed in Section 3.2) that the parallel heat conduction, which is modeled through the Spitzer conductivity, does not exceed the free streaming limit [50],  $q_{e,i}^{FS} \simeq 0.8nT_{e,i}\nu_{th\ e,i}$ , in the quasi-steady state. Therefore, heat flux limiters (as discussed, e.g., in Ref.[50]) are not presently implemented in the GBS code, but will be considered for future simulations with higher temperatures.

The boundary conditions at the magnetic presheath entrance of the limiter plates for the drift-reduced Braginskii equations are discussed in Ref. [40], where a set of first-principles boundary conditions was derived. We remark that the boundary conditions of the kinetic neutral equation, Eq. (2.1), at the limiter or divertor plates, Eq. (2.5), are specified at the solid wall. However, since the neutral mean free path is typically much longer than the width of the magnetic presheath, we will assume that the boundary conditions of the neutral kinetic equation at the wall coincide with the ones at the magnetic presheath entrance.

Equations (2.16)-(2.21), in the limit of  $n_n \rightarrow 0$ , have been implemented in the GBS code [10] and used in the past to study the main properties of plasma turbulence in the tokamak SOL. Investigations carried out with GBS have significantly advanced our understanding of, e.g., the turbulent saturation mechanisms in the SOL [51], the SOL turbulent regimes [52], the phenomena behind the generation of intrinsic rotation [53], the scaling of the SOL width in inner-wall limited tokamak plasma [54],

and the equilibrium electrostatic potential [55].

## 2.4 Formal solution of the neutral kinetic equation

We now solve the kinetic advection equation for the neutrals, Eq. (2.1), by using the method of characteristics, under the assumption that plasma-related quantities are known. We remark that, similarly to iterative methods to solve the kinetic neutral equation (see, e.g., Ref. [56]), this method allows to obtain the neutral moments without the statistical noise that is inherent to the Monte Carlo method. The formal solution of Eq. (2.1) is

$$f_n(\mathbf{x}, \mathbf{v}, t) = \int_0^{r'_b} \left[ \frac{S(\mathbf{x}', \mathbf{v}, t')}{v} + \delta(r' - r'_b) f_n(\mathbf{x}'_b, \mathbf{v}, t'_b) \right] \times \exp \left[ -\frac{1}{v} \int_0^{r'} v_{\text{eff}}(\mathbf{x}'', t'') dr'' \right] dr' \quad (2.22)$$

where  $\mathbf{x}' = \mathbf{x} - r' \hat{\Omega}$ ,  $t' = t - r'/v$ ,  $v = |\mathbf{v}|$ , and  $\hat{\Omega} = \mathbf{v}/v$ . (The single prime is used to indicate the source location of neutrals.) Similar definitions apply to  $\mathbf{x}''$  and  $t''$ . (The double prime is used for locations along the path integral between the source,  $\mathbf{x}'$ , and the observed location,  $\mathbf{x}$ .) Moreover, the subscript  $b$  is used as an indication for a position on the boundary. Therefore,  $\mathbf{x}'_b = \mathbf{x} - r'_b \hat{\Omega}$  is the intersection of the vector parallel to  $\hat{\Omega}$ , starting at  $\mathbf{x}$ , with the boundary, and  $t'_b = t - r'_b/v$ . The neutral source term consists of a volumetric source,  $S(\mathbf{x}', \mathbf{v}, t')$ , resulting from charge-exchange and recombination processes, given by

$$S(\mathbf{x}', \mathbf{v}, t') = v_{\text{cx}}(\mathbf{x}', t') n_n(\mathbf{x}', t') \Phi_i(\mathbf{x}', \mathbf{v}, t') + v_{\text{rec}}(\mathbf{x}', t') f_i(\mathbf{x}', \mathbf{v}, t'), \quad (2.23)$$

where  $\Phi_i = f_i/n_i$  is the ion velocity distribution, and of the  $\delta(r' - r'_b) f_n(\mathbf{x}'_b, \mathbf{v}, t'_b)$  term, which is localized at the boundary of the domain, where  $f_n(\mathbf{x}'_b, \mathbf{v}, t'_b)$  is given by the boundary conditions, Eqs. (2.5) and (2.7). The effective cross-section for the removal of the neutrals is given by  $v_{\text{eff}}(\mathbf{x}'', t'') = v_{\text{iz}}(\mathbf{x}'', t'') + v_{\text{cx}}(\mathbf{x}'', t'')$ . We remark that we split the charge exchange term in Eq. (2.1) into a source and sink term, which are, together, still particle conserving. Because  $S(\mathbf{x}', \mathbf{v}, t')$  depends on  $n_n(\mathbf{x}', t') = \int f_n(\mathbf{x}', \mathbf{v}, t') d\mathbf{v}$  [see Eq. (2.23)], Eq. (2.22) is an integral equation for  $f_n$  in the spatial and velocity domain that involves plasma and neutral quantities at past times.

We now consider two approximations, valid in the typical SOL parameter regime, which considerably simplify Eq. (2.22) and therefore the numerical investigation of the neutral dynamics. First, we Taylor expand the source term  $S$  and the other

## 2.4. Formal solution of the neutral kinetic equation

time-dependent quantities appearing in the integral in Eq. (2.22) about time  $t' = t$ , i.e.

$$S(\mathbf{x}', t') = S\left(\mathbf{x}', t - \frac{r'}{v}\right) = S(\mathbf{x}', t) - \frac{\partial S(\mathbf{x}', t')}{\partial t'} \Big|_{t'=t} \frac{r'}{v} + o\left(\frac{r'}{v}\right). \quad (2.24)$$

We now note that  $S$  varies in time on the typical plasma turbulent time scale,  $\tau_{\text{turb}}$ , while  $r'/v$  constitutes the typical flight time of the neutrals,  $\tau_n$ , which can be estimated as  $\tau_n \sim v_{\text{eff}}^{-1}$ . For typical SOL and edge parameters  $\tau_n < \tau_{\text{turb}}$ . It follows therefore that we can approximate  $S(\mathbf{x}', t') \simeq S(\mathbf{x}', t)$ , which corresponds to taking  $\partial_t f_n = 0$  in Eq. (2.1). This is a commonly used assumption (see, e.g., Ref. [47]), which has been denoted as the neutral adiabatic regime [57].

Second, we take advantage of the plasma turbulence anisotropy to reduce the solution of the three-dimensional neutral model to a set of two-dimensional problems. In fact, turbulent plasma structures are considerably more elongated along the magnetic field lines than perpendicular to them,  $k_{\parallel} \ll k_{\perp}$ , and the neutral mean free path,  $\lambda_{\text{mfp},n}$ , is typically much shorter (of the order of millimeters or centimeters) than the parallel elongation of the turbulent plasma structures, which is of the order of the machine size (i.e. of the order of a meter). We therefore have  $\lambda_{\text{mfp},n} \sim v/v_{\text{eff}} \ll 1/k_{\parallel}$ . (We remark that neutrals in the tail of the distribution function originating from charge exchange processes might have much longer mean free paths, but  $\lambda_{\text{mfp},n} \ll 1/k_{\parallel}$  is fulfilled for the bulk of the neutrals in a typical tokamak SOL.) To take advantage of the plasma anisotropy, we introduce a set of coordinates aligned to  $\mathbf{B}$ , that is  $\mathbf{x} = (\mathbf{x}_{\perp}, x_{\parallel})$ , where  $\mathbf{x}_{\perp}$  denotes the coordinates in the direction perpendicular to  $\mathbf{B}$ , and  $x_{\parallel}$  parallel to it. We note that  $x_{\parallel}$  approximately coincides with the toroidal direction, and  $\mathbf{x}_{\perp}$  denotes the coordinate in the poloidal plane, in the large aspect ratio limit and at the large value of the safety factor,  $q$ , of typical tokamak SOL ( $R_0/a_0 \gg 1$ ,  $q > 1$ ). We expand the source  $S$  and the other quantities appearing in Eq. (2.22) about  $x'_{\parallel} = x_{\parallel}$ , that is

$$S(\mathbf{x}'_{\perp}, x'_{\parallel}, t) = S(\mathbf{x}'_{\perp}, x_{\parallel}, t) + \frac{\partial S(\mathbf{x}'_{\perp}, x'_{\parallel}, t)}{\partial x'_{\parallel}} \Big|_{x'_{\parallel}=x_{\parallel}} (x'_{\parallel} - x_{\parallel}) + o(x'_{\parallel} - x_{\parallel}). \quad (2.25)$$

Now, because of the exponential decay due to ionization and charge exchange processes, the contribution of  $S$  to the integral in Eq. (2.22) becomes small at distances longer than  $\lambda_{\text{mfp},n}$ . Therefore, the expansion in Eq. (2.25) has to be considered for  $x'_{\parallel} - x_{\parallel} \lesssim \lambda_{\text{mfp},n}$ . Being  $\partial_{x'_{\parallel}} S(\mathbf{x}'_{\perp}, x'_{\parallel}, t) \sim k_{\parallel} S(\mathbf{x}'_{\perp}, x'_{\parallel}, t)$ , and  $k_{\parallel} \lambda_{\text{mfp},n} \ll 1$ , it follows that  $S(\mathbf{x}'_{\perp}, x'_{\parallel}, t) \simeq S(\mathbf{x}'_{\perp}, x_{\parallel}, t)$  in the regime of interest.

Within the adiabatic approximation,  $\tau_n < \tau_{\text{turb}}$ , and the assumption of  $k_{\parallel} \lambda_{\text{mfp},n} \ll 1$ ,

the formal solution of the neutral kinetic equation, Eq. (2.1), becomes

$$f_n(\mathbf{x}_\perp, x_\parallel, \mathbf{v}, t) = \int_0^{r_{\perp b}} \left[ \frac{S(\mathbf{x}'_\perp, x_\parallel, \mathbf{v}, t)}{v_\perp} + \delta(r'_\perp - r_{\perp b}) f_n(\mathbf{x}'_{\perp b}, x_\parallel, \mathbf{v}, t) \right] \quad (2.26)$$

$$\times \exp \left[ -\frac{1}{v_\perp} \int_0^{r'_\perp} v_{\text{eff}}(\mathbf{x}''_\perp, x_\parallel, t) dr''_\perp \right] dr'_\perp$$

where  $r'_\perp$  has been defined through  $\mathbf{x}'_\perp = \mathbf{x}_\perp - r'_\perp \hat{\mathbf{\Omega}}_\perp$ ,  $\hat{\mathbf{\Omega}}_\perp = \mathbf{v}_\perp / v_\perp$ , and  $\mathbf{v}_\perp$  is the perpendicular velocity. Since the dependencies in Eq. (2.26) on the parallel direction and on time are parametric, in the following, for better readability, we do not carry over the explicit notation of the  $t$  and  $x_\parallel$  dependence.

In Eq. (2.26), the recombination term contained in  $S$  [see Eq. (2.23)], as well as the term associated to ion recycling at the limiter present in the boundary conditions, do not depend on  $f_n(\mathbf{x}_\perp, \mathbf{v})$  and can be evaluated once the plasma quantities are known. On the other hand, the charge-exchange collision term on the right-hand side of Eq. (2.26) contained in  $S$ , and the reflected or re-emitted neutrals from the walls, which appear in the boundary term, depend on  $f_n(\mathbf{x}_\perp, \mathbf{v})$  through  $n_n(\mathbf{x}_\perp)$ . This suggests that a linear integral equation for  $n_n(\mathbf{x}_\perp)$  can be obtained by integrating Eq. (2.26) in velocity space, which is

$$n_n(\mathbf{x}_\perp) = \int_0^\infty dv_\perp v_\perp \int_0^{2\pi} d\vartheta \int_{-\infty}^\infty dv_\parallel \int_0^{r_{\perp b}} dr'_\perp \quad (2.27)$$

$$\left\{ \left[ \frac{S(\mathbf{x}'_\perp, \mathbf{v})}{v_\perp} + \delta(r'_\perp - r'_{\perp b}) f_n(\mathbf{x}'_\perp, \mathbf{v}) \right] \exp \left[ -\frac{1}{v_\perp} \int_0^{r'_\perp} v_{\text{eff}}(\mathbf{x}''_\perp) dr''_\perp \right] \right\}$$

where we use cylindrical coordinates,  $(v_\perp, \vartheta, v_\parallel)$ , in velocity space (also in this case parallel and perpendicular denote the direction with respect to the magnetic field).

We now describe two properties that help us simplify Eq. (2.27). First, for a generic function  $F(\mathbf{x}_\perp, \mathbf{x}'_\perp)$  we can write

$$\int_0^{r_{\perp b}} dr'_\perp \int_0^{2\pi} d\vartheta F(\mathbf{x}_\perp, \mathbf{x}'_\perp) = \int_D dA' \frac{1}{r'_\perp} F(\mathbf{x}_\perp, \mathbf{x}'_\perp), \quad (2.28)$$

where  $dA'$  is the infinitesimal area of  $D$ , which is the part of the plane perpendicular to the magnetic field, approximatively corresponding to the poloidal plane, that is optically connected to  $\mathbf{x}_\perp$ . Second, we use the following property,

$$\int_0^{r_{\perp b}} dr'_\perp \int_0^{2\pi} d\vartheta \delta(r'_\perp - r'_{\perp b}) F(\mathbf{x}_\perp, \mathbf{x}'_\perp) = \int_{\partial D} da'_b \frac{\cos \theta'}{r'_{\perp b}} F(\mathbf{x}_\perp, \mathbf{x}'_{\perp b}), \quad (2.29)$$

## 2.4. Formal solution of the neutral kinetic equation

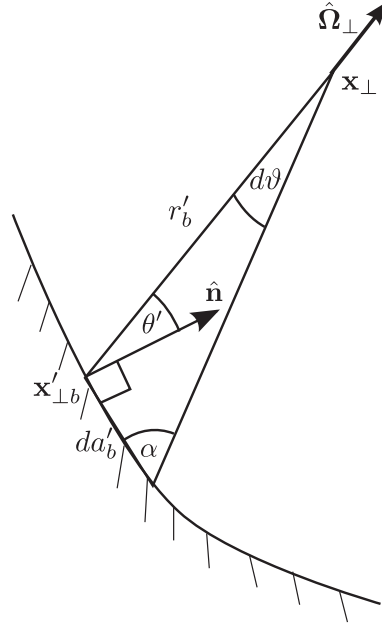


Figure 2.2 – Illustration of the transformation from an angular integral (in  $\vartheta$ ) to a line integral (in  $a'_b$ ) for neutrals coming from a section of the boundary of length  $da'_b$  at  $\mathbf{x}'_{\perp b}$  arriving at  $\mathbf{x}_{\perp}$  flying in the direction  $\hat{\Omega}_{\perp}$ .

where  $da'_b$  is the infinitesimal length along  $\partial D$ , which is the boundary of  $D$ , and  $\theta' = \arccos|\hat{\Omega}_{\perp} \cdot \hat{\mathbf{n}}|$  is the angle between  $\hat{\Omega}_{\perp}$  and  $\hat{\mathbf{n}}$  at the boundary location,  $\mathbf{x}'_{\perp b}$ . In fact, the  $r'$  integral gives

$$\int_0^{r'_{\perp b}} dr'_{\perp} \int_0^{2\pi} d\vartheta \delta(r'_{\perp} - r'_{\perp b}) F(\mathbf{x}_{\perp}, \mathbf{x}'_{\perp}) = \int_0^{2\pi} d\vartheta F(\mathbf{x}_{\perp}, \mathbf{x}'_{\perp b}), \quad (2.30)$$

and the  $\vartheta$  integral is transformed to a line integral along  $\partial D$  by using the law of sines for the triangle in Fig. 2.2, namely

$$\frac{da'_b}{d\vartheta} = \frac{r'_{\perp b}}{\sin(\alpha)} = \frac{r'_{\perp b}}{\cos(\theta')}, \quad (2.31)$$

as  $\alpha = \pi/2 - \theta'$  for infinitesimal small  $d\vartheta$ .

Now, by rearranging the integrals in Eq. (2.27) and using the two properties, Eqs. (2.28)

and (2.29), we obtain

$$\begin{aligned}
 n_n(\mathbf{x}_\perp) = & \int_D dA' \frac{1}{r'_\perp} \int_0^\infty dv_\perp v_\perp \int_{-\infty}^\infty dv_\parallel \left\{ \frac{S(\mathbf{x}'_\perp, \mathbf{v})}{v_\perp} \exp \left[ -\frac{1}{v_\perp} \int_0^{r'_\perp} v_{\text{eff}}(\mathbf{x}'_\perp) dr''_\perp \right] \right\} \\
 & + \int_{\partial D} da'_b \frac{\cos \theta'}{r'_{\perp b}} \int_0^\infty dv_\perp v_\perp \int_{-\infty}^\infty dv_\parallel \left\{ f_n(\mathbf{x}'_{\perp b}, \mathbf{v}) \exp \left[ -\frac{1}{v_\perp} \int_0^{r'_{\perp b}} v_{\text{eff}}(\mathbf{x}'_\perp) dr''_\perp \right] \right\}.
 \end{aligned} \tag{2.32}$$

The quantities that do not depend on velocity, that is  $n_n(\mathbf{x}'_\perp)$ ,  $v_{\text{cx}}(\mathbf{x}'_\perp)$ , and  $\Gamma_{\text{out}}(\mathbf{x}'_{\perp b})$  [inside  $S(\mathbf{x}'_\perp, \mathbf{v})$ , and  $f_n(\mathbf{x}'_{\perp b}, \mathbf{v})$  respectively], can be taken out of the velocity integrals, leading to an integral equation for  $n_n(\mathbf{x}_\perp)$ , which is

$$\begin{aligned}
 n_n(\mathbf{x}_\perp) = & \int_D n_n(\mathbf{x}'_\perp) v_{\text{cx}}(\mathbf{x}'_\perp) K_{\text{p} \rightarrow \text{p}}(\mathbf{x}_\perp, \mathbf{x}'_\perp) dA' \\
 & + \int_{\partial D} \Gamma_{\text{out}}(\mathbf{x}'_{\perp b}) K_{\text{b} \rightarrow \text{p}}(\mathbf{x}_\perp, \mathbf{x}'_{\perp b}) da'_b + n_{\text{n,rec}}(\mathbf{x}_\perp),
 \end{aligned} \tag{2.33}$$

where  $\Gamma_{\text{out}}$ , the perpendicular component of neutral and ion flux outflowing into the boundary, is

$$\begin{aligned}
 \Gamma_{\text{out}}(\mathbf{x}_{\perp b}) = & \int v_\perp \cos \theta f_n(\mathbf{x}_{\perp b}, \mathbf{v}_\perp) d\mathbf{v}_\perp + \Gamma_{\text{out},i}(\mathbf{x}_{\perp b}) \\
 = & \int_D n_n(\mathbf{x}'_\perp) v_{\text{cx}}(\mathbf{x}'_\perp) K_{\text{p} \rightarrow \text{b}}(\mathbf{x}_{\perp b}, \mathbf{x}'_\perp) dA' \\
 & + \int_{\partial D} \Gamma_{\text{out}}(\mathbf{x}'_{\perp b}) K_{\text{b} \rightarrow \text{b}}(\mathbf{x}_{\perp b}, \mathbf{x}'_{\perp b}) da'_b + \Gamma_{\text{out,rec}}(\mathbf{x}_{\perp b}) + \Gamma_{\text{out},i}(\mathbf{x}_{\perp b}),
 \end{aligned} \tag{2.34}$$

and where  $\theta = \arccos|\hat{\mathbf{\Omega}}_\perp \cdot \hat{\mathbf{n}}|$  is the angle between  $\hat{\mathbf{\Omega}}_\perp$  and  $\hat{\mathbf{n}}$  at the boundary location,  $\mathbf{x}_{\perp b}$ . Moreover, the following kernel functions have been defined

$$K_{\text{p} \rightarrow \text{p}}(\mathbf{x}_\perp, \mathbf{x}'_\perp) = \int_0^\infty \frac{1}{r'_\perp} \Phi_{\perp i}(\mathbf{x}'_\perp, \mathbf{v}_\perp) \exp \left[ -\frac{1}{v_\perp} \int_0^{r'_\perp} v_{\text{eff}}(\mathbf{x}'_\perp) dr''_\perp \right] dv_\perp \tag{2.35}$$

$$K_{\text{b} \rightarrow \text{p}}(\mathbf{x}_\perp, \mathbf{x}'_{\perp b}) = \int_0^\infty \frac{v_\perp}{r'_{\perp b}} \cos \theta' \chi_{\perp \text{in}}(\mathbf{x}'_{\perp b}, \mathbf{v}_\perp) \exp \left[ -\frac{1}{v_\perp} \int_0^{r'_\perp} v_{\text{eff}}(\mathbf{x}'_\perp) dr''_\perp \right] dv_\perp \tag{2.36}$$

$$K_{\text{p} \rightarrow \text{b}}(\mathbf{x}_{\perp b}, \mathbf{x}'_\perp) = \int_0^\infty \frac{v_\perp}{r'_\perp} \cos \theta \Phi_{\perp i}(\mathbf{x}'_\perp, \mathbf{v}_\perp) \exp \left[ -\frac{1}{v_\perp} \int_0^{r'_\perp} v_{\text{eff}}(\mathbf{x}'_\perp) dr''_\perp \right] dv_\perp \tag{2.37}$$



## 2.4. Formal solution of the neutral kinetic equation

$$K_{b \rightarrow b}(\mathbf{x}_{\perp b}, \mathbf{x}'_{\perp b}) = \int_0^{\infty} \frac{v_{\perp}^2}{r'_{\perp b}} \cos\theta \cos\theta' \chi_{\perp \text{in}}(\mathbf{x}'_{\perp b}, \mathbf{v}) \exp \left[ -\frac{1}{v_{\perp}} \int_0^{r'_{\perp}} v_{\text{eff}}(\mathbf{x}'_{\perp}) dr''_{\perp} \right] dv_{\perp}, \quad (2.38)$$

where we have carried out the integral in  $v_{\parallel}$  to obtain

$$\Phi_{\perp i}(\mathbf{x}_{\perp}, \mathbf{v}_{\perp}) = \int \Phi_i(\mathbf{x}_{\perp}, \mathbf{v}) dv_{\parallel} = \frac{m_i}{2\pi T_i} \exp \left( -\frac{m_i v_{\perp}^2}{2T_i} \right) \quad (2.39)$$

and

$$\begin{aligned} \chi_{\perp \text{in}}(\mathbf{x}_{\perp}, \mathbf{v}_{\perp}) &= \int \chi_{\text{in}}(\mathbf{x}_{\perp}, \mathbf{v}) dv_{\parallel} \\ &= \frac{3m_i^2}{4\pi T_i^2} v_{\perp} \cos\theta \exp \left( -\frac{m_i v_{\perp}^2}{4T_i} \right) \mathcal{K}_0 [m_i v_{\perp}^2 / (4T_i)], \end{aligned} \quad (2.40)$$

with  $\mathcal{K}_0(x)$  the modified Bessel function of the second kind.

The four kernels, Eqs. (2.35)-(2.38), depict the four different possible paths for neutral particles: originating from within the plasma or from the boundary, and arriving at a position in the plasma or on the boundary. All kernels include an exponentially decaying term, to take into account the loss of neutrals between the origin and arrival positions due to ionization and charge-exchange collisions. Furthermore, we note that neutrals that are emitted in the plasma region originate from a source proportional to  $\Phi_{\perp i}$  (see  $K_{p \rightarrow p}$  and  $K_{p \rightarrow b}$ ), while neutrals are emitted at the boundary with a source proportional to  $\chi_{\perp \text{in}} v_{\perp} \cos\theta'$  (see  $K_{b \rightarrow p}$  and  $K_{b \rightarrow b}$ ). Since  $\Gamma_{\text{out}}$  describes the perpendicular outflow into the boundary, the kernels  $K_{p \rightarrow b}$  and  $K_{b \rightarrow b}$  include a  $v_{\perp} \cos\theta$  term. We note that the kernels, Eqs. (2.35)-(2.38), are given in the limit of  $\alpha_{\text{refl}} = 0$ , such that only the neutrals' direct path from  $\mathbf{x}'_{\perp}$  to  $\mathbf{x}_{\perp}$  is taken into account. In the case of  $\alpha_{\text{refl}} > 0$ , the paths over all possible reflection points for the combination  $(\mathbf{x}'_{\perp}, \mathbf{x}_{\perp})$  have to be included in the kernels. In the current implementation of the kernels, Eqs. (2.35)-(2.38), and the boundary condition, Eq. (2.5), in the GBS code only reflection at the toroidal rail limiter is included, such that there can only be one or no reflection point for each  $(\mathbf{x}'_{\perp}, \mathbf{x}_{\perp})$ .

The neutral density and the neutral outflow caused by volumetric recombination are evaluated using kernels  $K_{p \rightarrow p}$  and  $K_{p \rightarrow b}$  resulting in

$$n_{n, \text{rec}}(\mathbf{x}_{\perp}) = \int_D n_i(\mathbf{x}'_{\perp}) v_{\text{rec}}(\mathbf{x}'_{\perp}) K_{p \rightarrow p}(\mathbf{x}_{\perp}, \mathbf{x}'_{\perp}) dA' \quad (2.41)$$

and

$$\Gamma_{\text{out,rec}}(\mathbf{x}_{\perp b}) = \int_D n_i(\mathbf{x}'_{\perp}) v_{\text{rec}}(\mathbf{x}'_{\perp}) K_{\text{p} \rightarrow \text{b}}(\mathbf{x}_{\perp b}, \mathbf{x}'_{\perp}) dA'. \quad (2.42)$$

We remark that the kernel functions,  $K_{\text{p} \rightarrow \text{p}}$ ,  $K_{\text{b} \rightarrow \text{p}}$ ,  $K_{\text{p} \rightarrow \text{b}}$ , and  $K_{\text{b} \rightarrow \text{b}}$ , do neither depend on  $f_n(\mathbf{x}_{\perp}, \mathbf{v})$ , nor on any of its moments. They can be evaluated once the problem geometry and the plasma state are known.

Having solved Eq. (2.33), therefore once  $n_n(\mathbf{x}_{\perp})$  is known, the distribution function of the neutral atoms,  $f_n(\mathbf{x}_{\perp}, \mathbf{v})$ , can be readily evaluated by using Eq. (2.26). At that point, the moments of  $f_n(\mathbf{x}_{\perp}, \mathbf{v})$  that are needed in the neutral-plasma interaction terms presented in the drift-reduced Braginskii equations, Eqs. (2.16)-(2.21), such as the fluid parallel neutral velocity,  $v_{\parallel n}(\mathbf{x}_{\perp})$ , and the neutral temperature,  $T_n(\mathbf{x}_{\perp})$ , can be computed without difficulties. The numerical discretization of the neutral model is described in Section 2.5, and its convergence properties are discussed in Section 2.7.

## 2.5 Numerical implementation

In the following we introduce the discretization of Eq. (2.33) necessary for its numerical solution. The spatial discretization for the neutral equation can be set independently of the grid on which the plasma quantities are evolved. If the two spatial discretizations do not match, a linear two-dimensional interpolation routine is used to port the plasma and neutral fields from one grid to the other. We remark that, while the use of any grid to solve Eq. (2.33), including unstructured meshes, does not present any conceptual difficulty, in the current implementation we use an equidistant grid in the poloidal and radial direction for each poloidal plane.

On a discretized spatial grid, Eqs. (2.33) and (2.34) assume the form

$$n_n^i = \sum_j K_{\text{p} \rightarrow \text{p}}^{i,j} v_{\text{cx}}^j n_n^j + \sum_j K_{\text{b} \rightarrow \text{p}}^{i,j} \Gamma_{\text{out}}^j + n_{\text{n,rec}}^i \quad (2.43)$$

and

$$\Gamma_{\text{out}}^i = \sum_j K_{\text{p} \rightarrow \text{b}}^{i,j} v_{\text{cx}}^j n_n^j + \sum_j K_{\text{b} \rightarrow \text{b}}^{i,j} \Gamma_{\text{out}}^j + \Gamma_{\text{out,rec}}^i + \Gamma_{\text{out,i}}^i \quad (2.44)$$

where  $i$  and  $j$  are grid cell indices (the  $i$ -th grid cell is centered around  $\mathbf{x}_{\perp}^i$  and has an

area  $\Delta A^i$ ), and

$$K_{p \rightarrow p}^{i,j} = \frac{\Delta A^j}{r^{ij}} \int_0^\infty \Phi_{\perp i}(\mathbf{x}_\perp^j, v_\perp \hat{\mathbf{r}}^{ij}) \exp \left[ -\frac{1}{v_\perp} \int_0^{r^{ij}} v_{\text{eff}}(\mathbf{x}_\perp^j + r' \hat{\mathbf{r}}^{ij}) dr' \right] dv_\perp \quad (2.45)$$

with  $\mathbf{r}^{ij} = \mathbf{x}_\perp^i - \mathbf{x}_\perp^j$ , and  $\hat{\mathbf{r}}^{ij} = \mathbf{r}^{ij} / r^{ij}$ . Equivalent expressions apply to the other kernels.

In Eq. (2.45), the velocity integral is discretized in equidistant velocity intervals of size  $\Delta v$ , centered around  $(i_v + 1/2)\Delta v$ , usually up to  $v_{\text{max}} = 5c_{s0}$ , and computed by using the rectangle rule. On the other hand, the line integral between  $\mathbf{x}_\perp^i$  and  $\mathbf{x}_\perp^j$ ,  $\int_0^{r^{ij}} v_{\text{eff}}(\mathbf{x}_\perp^j + r' \hat{\mathbf{r}}^{ij}) dr'$ , is equidistantly discretized into  $N_{\text{interp}} + 1$  intervals, and integrated using the trapezoidal rule. The values of  $v_{\text{eff}}(\mathbf{x}_\perp^j + r' \hat{\mathbf{r}}^{ij})$  required for the evaluation of the integral are obtained by using linear interpolation from the grid values.

Equations (2.43) and (2.44) are a system of linear equations that can be recast in matrix form

$$\begin{bmatrix} n_n \\ \Gamma_{\text{out}} \end{bmatrix} = \begin{bmatrix} K_{p \rightarrow p} & K_{b \rightarrow p} \\ K_{p \rightarrow b} & K_{b \rightarrow b} \end{bmatrix} \cdot \begin{bmatrix} n_n \\ \Gamma_{\text{out}} \end{bmatrix} + \begin{bmatrix} n_{n,\text{rec}} \\ \Gamma_{\text{out,rec}} + \Gamma_{\text{out,i}} \end{bmatrix} \quad (2.46)$$

and that can be solved with standard full matrix solvers. We note that, in the simulations presented in this Thesis, the matrix is typically filled by one third, since not every pair of grid cells is optically connected. The fraction of non-zero entries decreases at larger system size. As a matter of fact, entries of pairs that are separated by several  $\lambda_{\text{mfp},n}$  could be neglected, making the fraction of non-zero elements even smaller, leading to faster solutions with sparse matrix solvers and fewer matrix elements that have to be computed, which is the computationally most expensive part in the current implementation. While we have verified, a posteriori, that neglecting small matrix elements does not change the result significantly, it is not straightforward to predict the matrix elements that can be neglected, because of the evolving turbulent plasma properties and the related variation of  $\lambda_{\text{mfp},n}$ . In the present Thesis, methods to reduce the number of non-zero elements in the matrix were not developed.

Since the solution of Eq. (2.43) is particularly expensive, we use a short cycling scheme, as described in Ref. [24] and used, e.g., in Ref. [36]. More precisely, to apply the short cycle scheme, we recalculate the neutral density every time interval,  $\Delta t_n$ , where  $\Delta t_n$  is comparable to the turbulent timescales and longer than the typical time step used to advance numerically the drift-reduced Braginskii equations. However, the interaction terms in the plasma equations, Eqs. (2.16)-(2.21) (e.g.,  $n_n v_{iz} = n_n n \langle v_e \sigma_{iz} \rangle_v$ ) are recalculated at every time-step, taking into account the changing plasma quantities

(e.g.,  $n$ ), and the change in reaction rates (e.g.,  $\langle \nu_e \sigma_{iz} \rangle_\nu$ ), which depend on the plasma temperatures.

The drift-reduced Braginskii equations, Eqs. (2.16)-(2.21), are solved by the GBS code on an equidistant three-dimensional grid as described in Refs. [10, 11]. The parallel and perpendicular operators are discretized using a second order finite difference scheme, except for the  $[A_1, A_2]$  operators that are discretized by using the Arakawa scheme [58]. The Laplacian operator in the Poisson equation is also discretized using the standard centered finite difference scheme, and it is solved with either a sparse linear algebra solver or a multigrid solver [11]. Time integration of Eqs. (2.16)-(2.21) is carried out with the classical Runge-Kutta method [59]. We remark that we recast the equations for plasma density and electron and ion temperatures in terms of  $\theta_n = \log(n)$ ,  $t_e = \log(T_e)$ , and  $t_i = \log(T_i)$  to ensure the positivity of these quantities. The correctness of the implementation and numerical discretization of Eqs. (2.16)-(2.21) in the GBS code has been rigorously verified with the method of manufactured solutions [60].

## 2.6 First self-consistent plasma turbulence simulations with neutral atom dynamics

We report here the first simulations carried out with the GBS code [10, 11] extended by implementing the kinetic neutral atom model and the plasma-neutral interaction terms in the fluid equations. We compare here a low plasma density simulation, where the recycled neutrals are mostly ionized in the tokamak core, and therefore the source of SOL plasma is mainly due to the plasma outflow from the core (this simulation features the sheath limited regime), with a high plasma density simulation, where SOL plasma is coming partly from the core and partly from the recycling process occurring inside the SOL (several features of the so-called conduction limited regime are displayed by this simulation). Both simulations consider a limited SOL geometry, with a toroidal rail limiter on the high-field side equatorial midplane,  $R_0/\rho_{s0} = 500$ ,  $m_i/m_e = 400$ ,  $2\pi a_0 = 800\rho_{s0}$ , and  $T_{e0} = T_{i0} = 10\text{eV}$ . Furthermore, in the low plasma density simulation, we impose  $n_0 = 5 \cdot 10^{18}\text{m}^{-3}$ , the value of the density at the LCFS, and  $\tilde{\nu} = R_0 m_e / (1.96 c_{s0} m_i \tau_e) = 0.02$ , the resistivity normalized to  $R_0/c_{s0}$ . As a consequence, the dimensionless parallel electron heat conductivity is  $\tilde{\kappa}_{\parallel e} = 3.16 \times 2 T_{e0} \tau_e / (3 m_e c_{s0} R_0) = 56.0$ , the dimensionless parallel ion heat conductivity is  $\tilde{\kappa}_{\parallel i} = 3.9 \times 2 T_{i0} \tau_i / (3 m_i c_{s0} R_0) = 1.6$ , and the dimensionless electron viscosity coefficient is  $\tilde{\eta}_{e0} = 0.73 T_{e0} \tau_e / (m_e R_0 c_{s0}) = 20.0$ . In the high plasma density simulation,

## 2.6. First self-consistent simulations with neutral atom dynamics

---

$n_0 = 5 \cdot 10^{19} \text{m}^{-3}$ ,  $\tilde{v} = 0.2$ ,  $\tilde{\kappa}_{\parallel e} = 5.6$ ,  $\tilde{\kappa}_{\parallel i} = 0.16$ , and  $\tilde{\eta}_{e0} = 2.0$  are used. The computational domain extends radially from  $r_{\min} = 0$  to  $r_{\max} = 150\rho_{s0}$ . The source terms  $S_n$ ,  $S_{T_i}$ , and  $S_{T_e}$  in Eqs. (2.16)-(2.21) are constant in time, poloidally uniform, and radially Gaussian around  $r_s = 30\rho_{s0}$ , which we interpret as the radial position of the LCFS. Quantities displayed in the figures are normalized to  $n_0$ ,  $c_{s0}$ , and  $T_{e0}$ .

In Figs. 2.3 and 2.4 typical snapshots of plasma density, parallel electron and ion velocities, electron and ion temperatures, electrostatic potential, neutral density, and ionization source,  $S_{iz} = n_n v_{iz}$ , are shown on a poloidal cross-section. They display fully developed turbulence during the quasi-steady state of the two simulations.

The poloidal dependence of the relevant plasma quantities (plasma density, electron and ion parallel velocities, electron and ion temperatures, electrostatic potential, neutral density, and  $S_{iz}$ ) for the low- and high-density simulations are shown in Fig. 2.5. The displayed profiles are averaged over a time window of  $20 R_0/c_{s0}$ , over the full toroidal angle, and over a radial region extending for  $20 \rho_{s0}$ , centered at a distance of  $30 \rho_{s0}$  from the separatrix.

We point out a few interesting differences between the high- and low-density simulations. The poloidal density profile in the high-density simulation is flatter than in the low-density simulation. This is due to the fact that the plasma source due to the ionizations occurring close to the limiter inside the SOL is much higher in the high-density simulation, preventing the plasma density to drop when approaching the sheaths. The parallel velocity profiles (which are expected to be approximately linear if the plasma source is poloidally constant) are somewhat flatter close to the limiter in the high-density scenario; however, the flattening is not particularly significant, because a relatively large fraction of the plasma density source is still due to the poloidally constant outflow of particles from the core. Furthermore, both electron and ion temperature poloidal gradients increase in the high-density scenario, which is expected while going towards the conduction limited regime. The mechanisms that lead to this temperature drop include the reduced parallel heat conductivity (due to lower temperature and higher density), and the direct energy loss due to ionizations (see, e.g., Ref. [8]). To verify that these are the acting mechanism behind the temperature drop in the high-density scenario, the balance of the electron temperature equation, Eq. (2.20), in quasi steady state is shown in Fig. 2.6. The terms on the right hand side of Eq. (2.20) are toroidally, radially, and time averaged, in the same way as the poloidal profiles in Fig. 2.5. The terms are arranged into four groups, namely, the parallel advection term,  $A = -v_{\parallel e} \nabla_{\parallel} T_e + 2T_e / (3n) [0.71 / e \nabla_{\parallel} j_{\parallel} - n \nabla_{\parallel} v_{\parallel e}]$ , the parallel diffusion term,  $D = \kappa_{\parallel e} \nabla_{\parallel} (T_e^{5/2} \nabla_{\parallel} T_e)$ , the plasma-neutral interaction term,  $N = n_n v_{iz} / n [-2E_{iz} / 3 - T_e + m_e v_{\parallel e} (v_{\parallel e} - 4v_{\parallel n} / 3)] - n_n v_{en} m_e 2v_{\parallel e} / (3n) (v_{\parallel n} - v_{\parallel e})$ , and the

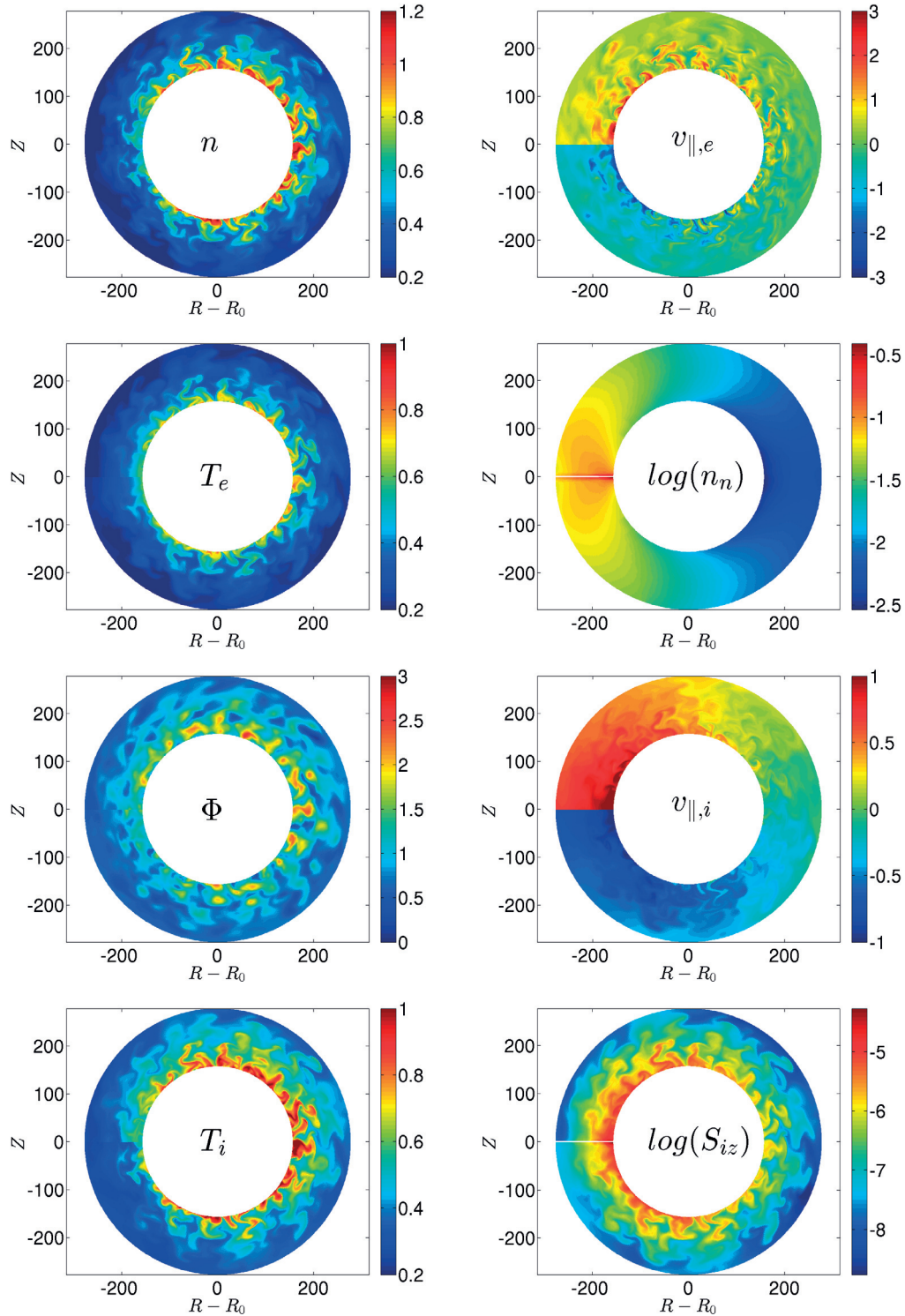


Figure 2.3 – Snapshots on a poloidal cross-section of plasma density, electric potential, ion and electron parallel velocities, electron and ion temperatures, neutral density, and the ionization source term,  $S_{iz}$ , for the low-density simulation,  $n_0 = 5 \cdot 10^{18} \text{m}^{-3}$ .

## 2.6. First self-consistent simulations with neutral atom dynamics

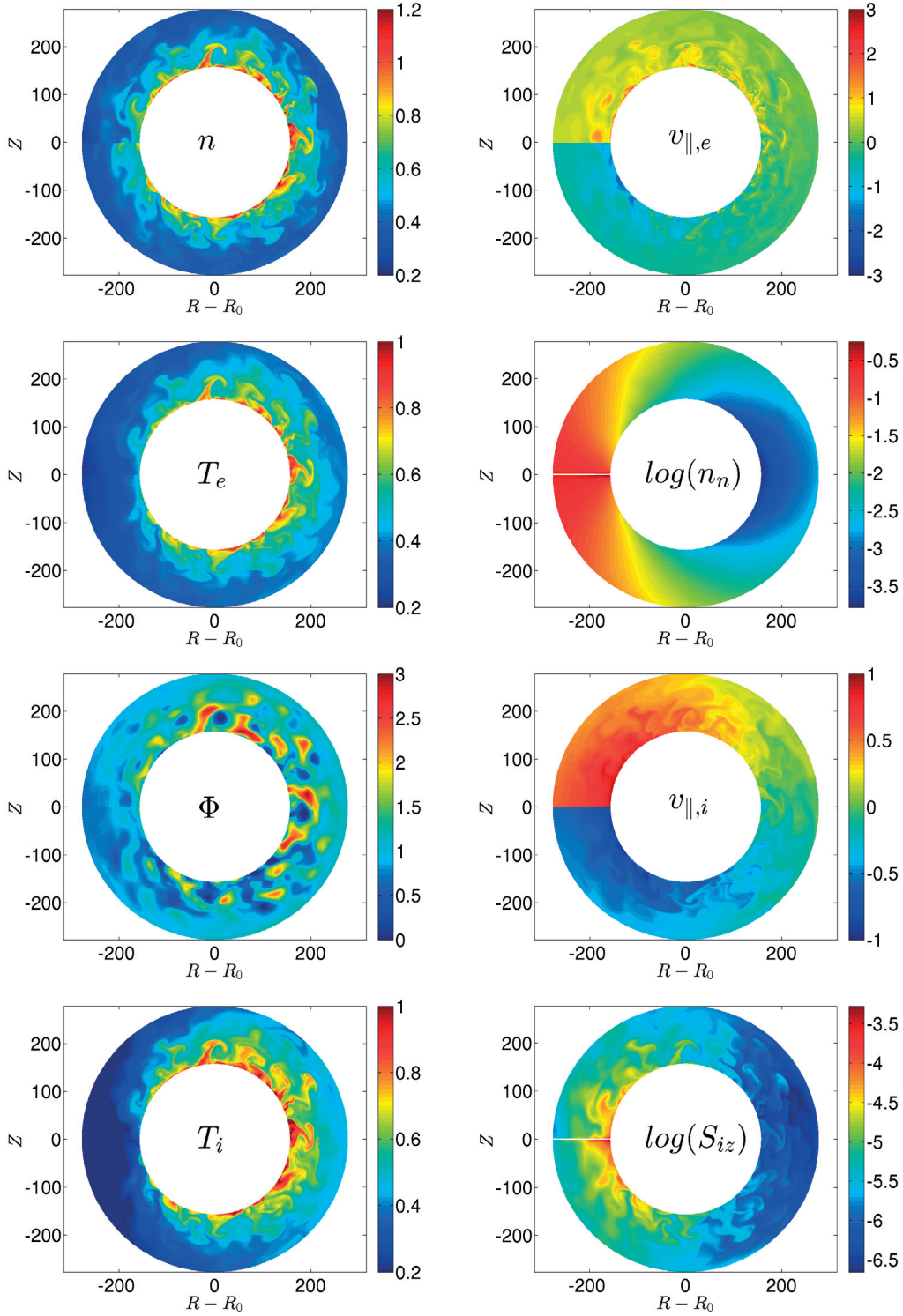


Figure 2.4 – Snapshots on a poloidal cross-section of plasma density, electric potential, ion and electron parallel velocities, electron and ion temperatures, neutral density, and the ionization source term,  $S_{iz}$ , for the high-density simulation,  $n_0 = 5 \cdot 10^{19} \text{ m}^{-3}$ .

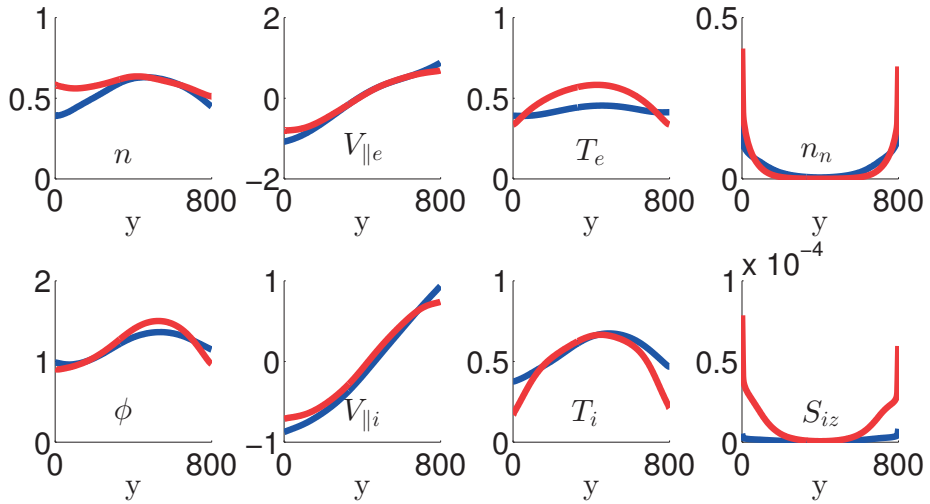


Figure 2.5 – Time-averaged poloidal profiles of  $n$ ,  $\Phi$ ,  $V_{\parallel e}$ ,  $V_{\parallel i}$ ,  $T_e$ ,  $T_i$ ,  $n_n$ , and  $S_{iz}$  for the low (blue) and high (red) plasma density scenario.

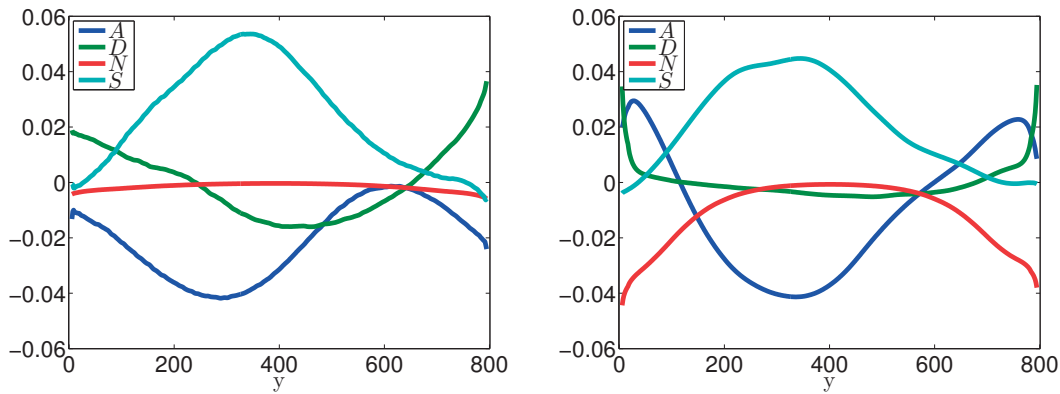


Figure 2.6 – Time-averaged poloidal balance of the electron temperature equation for the low (left) and high (right) density case. The shown terms are the parallel advection,  $A$ , the parallel diffusion,  $D$ , the contribution of the neutral interaction,  $N$ , and the sources in the electron temperature equation,  $S$ .



## 2.7. Convergence properties of the neutral model

source term,  $S = -1/B[\phi, T_e] + 4T_e/(3eB)[T_e C(n)/n + 7C(T_e)/2 - eC(\phi)] + \mathcal{D}_{T_e}(T_e) + S_{T_e}$ , which includes the divergence of the flow due to the  $\mathbf{E} \times \mathbf{B}$  and curvature drifts. It has been verified that the sum of the four terms converges towards zero as we increase the time-span over which the average is evaluated. From Fig. 2.6, it is apparent that both before mentioned mechanisms are important for the steepening of the electron temperature gradient. While the source term,  $S$ , has almost the same shape in the two scenarios, the plasma-neutral interaction term,  $N$ , is clearly important only in the high-density simulation (the most important contribution to  $N$  is due to the ionization process,  $-2n_n v_{iz} E_{iz}/(3n)$ ). The effect of  $N$  is to decrease the electron temperature close to the limiter. Furthermore, the parallel diffusion term,  $D$ , has a larger impact on the low-density simulation, where it flattens the temperature profile. In the low-density simulation, the importance of the parallel diffusion term arises from the high parallel electron conductivity, inversely proportional to the plasma density. In the high density simulation, the parallel diffusion term plays a significant role only in proximity of the limiter.

The electron temperature drop along the parallel direction is discussed further in Chapter 4, where a set of simulations (including the two simulations from this Chapter) is compared to a simple and a refined two-point model.

## 2.7 Convergence properties of the neutral model

To illustrate the numerical convergence properties, we consider the relative error in the conservation of neutral particles, defined as

$$\epsilon_{\text{rel}} = \frac{N_{\text{in}} - N_{\text{out}}}{N_{\text{in}}} \quad (2.47)$$

where  $N_{\text{in}} = \sum_i \Gamma_{\text{out},i}^i \Delta a_b^i + \sum_i n_i^i v_{\text{rec}}^i \Delta A^i$  is the number of neutrals that are created in a time unit due to ion recycling and recombination, and  $N_{\text{out}} = \sum_i n_n^i v_{iz}^i \Delta A^i + \sum_i \Gamma_{\text{out},\text{core}}^i \Delta a_b^i$  is the number of neutrals lost from the system in a time unit due to ionization and outflow to the core region. For the first two numerical tests in this Section we consider the low-density plasma scenario described in Section 2.6, the third convergence test is performed with a smaller simulation domain.

We carry out three convergence tests. We first study the convergence of the numerical solution with the spatial discretization. We use the radial distance from the LCFS,  $r$ , and the poloidal angle,  $\vartheta$ , as coordinates in the poloidal plane, which we discretize on a grid with equidistant points separated by the normalized distances  $\Delta x = \Delta r / \rho_{s0}$

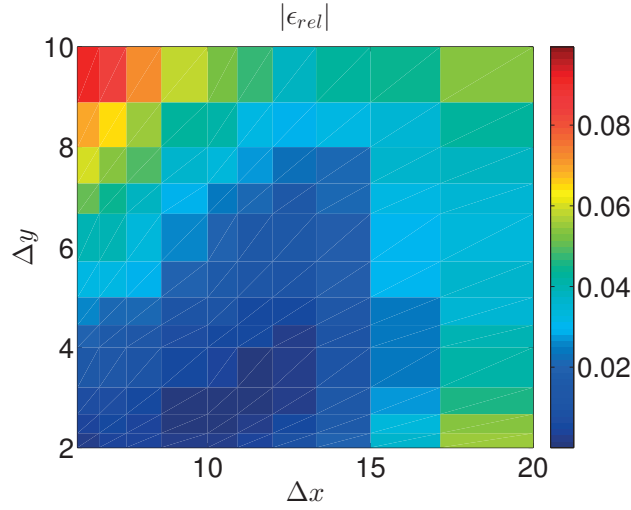


Figure 2.7 – Relative error of the neutral particle conservation,  $\epsilon_{\text{rel}}$ , as a function of the grid spacing in the radial,  $\Delta x$ , and poloidal,  $\Delta y$ , directions. The low density scenario,  $n_0 = 5 \cdot 10^{18} \text{m}^{-3}$ , which is presented in Section 2.6, is considered.

in the radial direction and  $\Delta y = a_0 / \rho_{s0} \Delta \vartheta$  in the poloidal direction. Figure 2.7 shows a convergence study on the spatial discretization. The best converged results are obtained for  $2 \lesssim \Delta x / \Delta y \lesssim 4$ . (The variation of the neutral quantities is stronger in the poloidal than in the radial direction.) Then, we perform a scan of solutions of Eq. (2.46) by varying the grid spacing and  $N_{\text{interp}}$  independently. The results are presented in Fig. 2.8. For small  $N_{\text{interp}}$ , the error does not converge to zero, but towards a finite value that is determined by the error associated with the discretization of the line integral between  $\mathbf{x}_{\perp}$  and  $\mathbf{x}'_{\perp}$ . This error decreases with increasing  $N_{\text{interp}}$  as it is shown in Fig. 2.8. To calculate the order of convergence, we extrapolate the error of the  $N_{\text{interp}} = 80$  curve to  $\Delta x = 0$ , to obtain  $\epsilon_{\text{extrp}} = \epsilon(\Delta x = 0)$ , where  $\epsilon_{\text{extrp}}$  includes the numerical error from the discretization of the line integral between  $\mathbf{x}_{\perp}$  and  $\mathbf{x}'_{\perp}$ , as well as the numerical errors from the velocity space discretization. Figure 2.9 shows the error due to the spatial grid discretization,  $\epsilon_{\text{rel}} - \epsilon_{\text{extrp}}$ , and reveals that the numerical algorithm has a linear convergence with respect to the grid spacing. Typically,  $\Delta x \approx 2.5$ ,  $\Delta y \approx 7.5$ , and  $N_{\text{interp}} = 20$  are used in our simulations.

The second test investigates the convergence with respect to the discretization of the velocity integral inside the kernel functions. Figure 2.10a shows the convergence with  $\Delta v$  for fixed  $v_{\text{max}} = 5.0 c_{s0}$ , while Fig. 2.10b shows the convergence with  $v_{\text{max}}$  for fixed  $\Delta v = 0.1 c_{s0}$ . Both figures show convergence towards a finite value of  $\epsilon_{\text{err}}$ , which is the error due to the spatial discretization. Typically,  $\Delta v = 0.1 c_{s0}$  and  $v_{\text{max}} = 5 c_{s0}$  are used in our simulations.

For the third convergence test, which investigates the short cycle scheme, we perform

## 2.7. Convergence properties of the neutral model

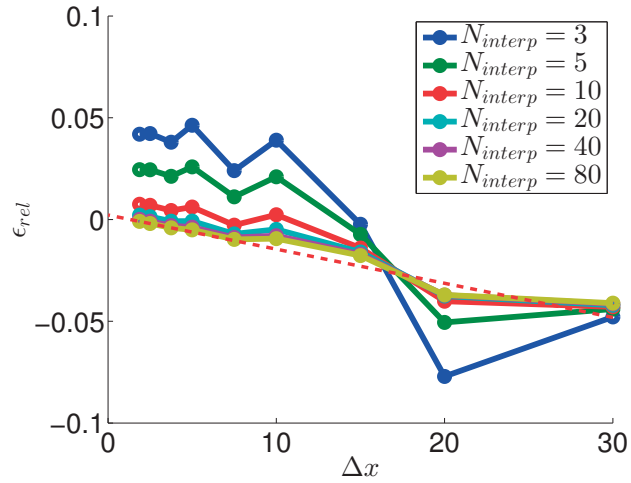


Figure 2.8 – Convergence of the numerical error,  $\epsilon_{\text{rel}}$ , depending on the grid size and the number of interpolation points. In particular, we consider  $\Delta x = [30, 20, 15, 10, 7.5, 5, 3.75, 2.5, 1.875]$ ,  $\Delta y = \Delta x/2.5$ , and  $N_{\text{interp}} = [3, 5, 10, 20, 40, 80]$ . The red dashed line is the extrapolation of  $\epsilon_{\text{rel}}$  to  $\Delta x = 0$  for the  $N_{\text{interp}} = 80$  case. The last three points, with the smallest  $\Delta x$ , are considered.

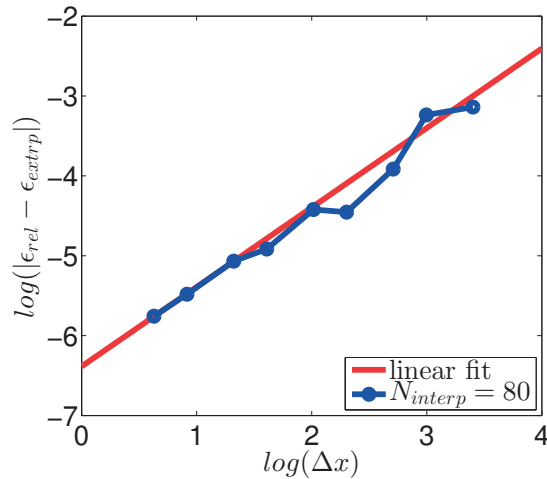


Figure 2.9 – Log-log plot of the numerical error,  $\epsilon_{\text{rel}}$ , as a function of the spatial discretization,  $\Delta x$  ( $\Delta y = \Delta x/2.5$ ), for the case  $N_{\text{interp}} = 80$ , including a linear fit [ $\log(|\epsilon_{\text{rel}} - \epsilon_{\text{extrp}}|) = 0.995 \log(\Delta x) - 6.39$ , using the three points with the smallest  $\Delta x$  for the fitting procedure] to demonstrate linear order of convergence.

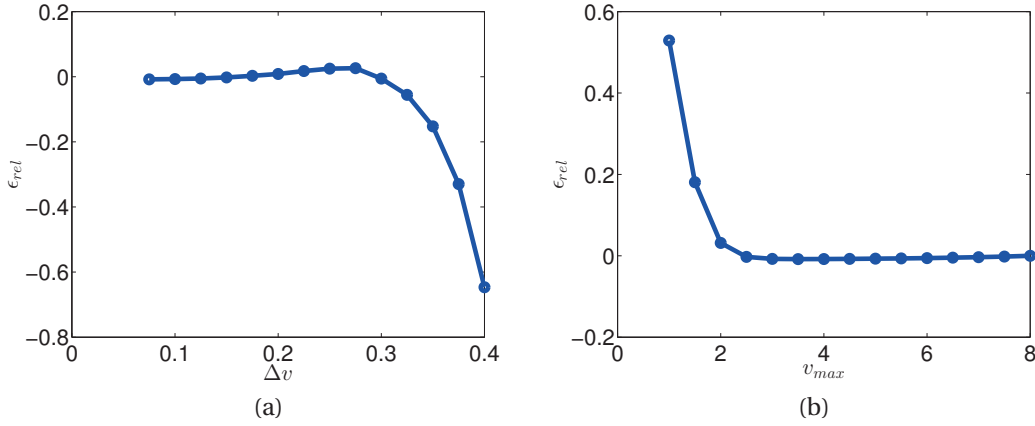


Figure 2.10 – Relative error of particle conservation,  $\epsilon_{rel}$ , as a function of the velocity discretization. (Both cases use  $\Delta x = 2.5\Delta y = 7.5$ , and  $N_{interp} = 20$ .) (a) Convergence is observed for  $\Delta v \lesssim 0.25c_{s0}$  (having fixed  $v_{max} = 5.0c_{s0}$ ). (b) Convergence is observed for  $v_{max} \gtrsim 2.5c_{s0}$  (having fixed  $\Delta v = 0.1c_{s0}$ ).

a set of non-linear simulations of SOL plasma dynamics by solving the drift-reduced Braginskii equations self-consistently with the neutral equation. We set  $\Delta t_n = 0.01, 0.05, 0.2, 1$ , and  $5 R_0/c_{s0}$ . Since these self-consistent simulations are computational demanding, we decrease the size of the considered domain to  $2\pi a_0 = 400\rho_{s0}$ ,  $r_{min} = 0$ ,  $r_{max} = 50\rho_{s0}$ , and move the location of density and temperature sources to  $r_s = 0\rho_{s0}$ . The results of all simulations show no significant nor systematic differences in the averaged plasma and neutral quantities (see, e.g., the time traces of the neutral density at the low-field side midplane in Fig. 2.11). We note that even the case  $\Delta t_n = 5R_0/c_{s0}$ , in which the neutral density does not follow the initial overshoot, evolves towards the same quasi-steady state.

We remark that in simulations that include both the SOL and edge region, large poloidal shear flows form around and inside the LCFS due to large radial electric fields. Depending on the orientation and magnitude of the shear flow, the plasma properties and structures below and above the limiter can vary during the simulation, which raises or lowers the local recycling rate. This has to be captured temporally in the neutral dynamics. Because of this, we usually choose  $\Delta t_n = 0.025R_0/c_{s0}$  in the simulations including both SOL and edge region, while we usually choose  $\Delta t_n = 0.1R_0/c_{s0}$  for simulations including only the SOL.

## 2.7. Convergence properties of the neutral model

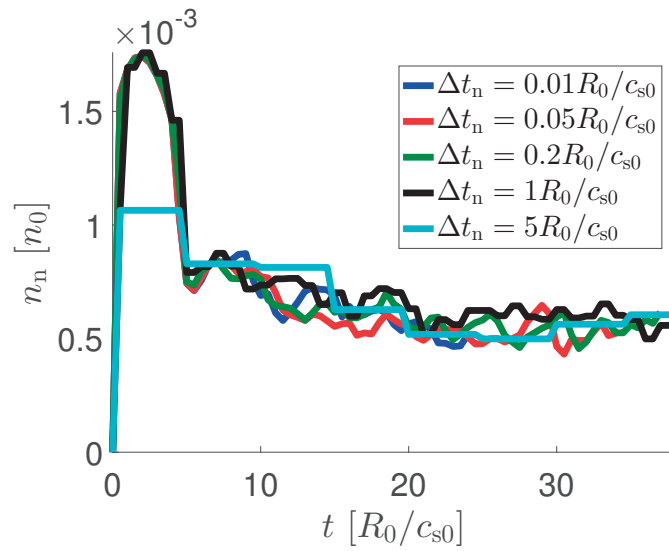


Figure 2.11 – Time traces of the neutral density at the low-field side midplane (averaged over the region  $10\rho_{s0} < r < 20\rho_{s0}$ ,  $195\rho_{s0} < y < 205\rho_{s0}$ ) for  $\Delta t_n = 0.01, 0.05, 0.2, 1,$  and  $5 R_0/c_{s0}$ .



## Chapter 3

# Identification of the key elements of the neutral-plasma interaction

In this Chapter we identify the key elements determining the interaction between neutrals and plasma in the tokamak periphery. For this purpose, we use a simulation of the SOL and edge regions of a tokamak with a toroidal rail limiter on the high-field side equatorial midplane. We study the importance of the different elements present in the neutral-plasma interaction by analyzing a number of simulations where we zero out some of these elements. The ultimate goal of this effort is to derive a simple model for the neutral-plasma interaction, by neglecting the less important terms, so that the computational cost of the simulations can be reduced. At the same time, a simpler model of the plasma-neutral interaction can help us to identify and understand the principal physical processes at play in the tokamak periphery.

This Chapter is structured as follows. After the Introduction, in Section 3.2 we present the simulation of the tokamak periphery that we use to identify the key elements of the neutral-plasma interaction. In Section 3.3, we investigate the impact of the neutral fluctuations on the time-averaged plasma profiles. In Section 3.4, we focus on the impact of the different plasma-neutral interaction terms. Further considerations, namely concerning the time-averaged plasma-neutral interaction terms and the impact of the poloidal localization of the ionization density source term, are presented in Section 3.5.

### 3.1 Introduction

While it has been pointed out that turbulence might significantly affect the neutral properties [57, 61], the self-consistent interaction of plasma turbulence and neutrals remains largely unexplored. More in general, despite recent progress in the simulations, the basic understanding of the physical mechanisms at play in the self-consistent interaction of turbulent plasma and neutral particles is still missing. The goal of the present Chapter is to identify the key elements of the neutral-plasma interaction by using self-consistent turbulent simulations of the tokamak periphery. In particular, we point out the role of neutral fluctuations, friction and energy sink terms, and the poloidal asymmetry of the ionization source. The investigation is carried out on the basis of one simulation, described in Section 3.2, that includes the SOL and edge regions of a limited tokamak. Starting point of the analysis is the kinetic model, which enables us to consider scenarios with both long and short neutral mean free paths, described in Section 2.2. The model includes ionization, charge-exchange, recombination, and elastic electron-neutral collisions, described by Krook collision operators. This relatively simple model facilitates the understanding of the basic physical processes at play in the neutral-plasma interaction. However, our investigation cannot validate the assumptions of our neutral model, such as neglecting the effects of molecules.

To identify the key elements of the neutral-plasma interaction, we first analyze the role of neutral fluctuations. It turns out that they do not affect significantly the time-averaged plasma profiles in the considered plasma conditions. The friction terms between the plasma species and the neutrals are also found not to play a significant role in setting the plasma profiles. On the other hand, the analysis of the role of the temperature equilibration term between ions and neutrals and the electron energy sink due to ionizations shows that they significantly affect the time-averaged plasma profiles, whereby we identify the interaction terms in the plasma temperature equations as being essential to the model within the investigated plasma conditions. Finally, we show that it is not possible to average the whole plasma-neutral interaction terms, and we present a brief investigation of the effects of the poloidal asymmetry in the plasma density source due to ionization processes.

We remark that our observations cannot be directly extrapolated to other regimes. In scenarios with higher plasma density and lower plasma temperatures, such as in detachment scenarios, the ionization and recombination regions and the detachment front might move, leading to substantial temporal variations in the neutral density, which can be much larger than in the present simulation. This is expected to enhance the importance of the neutral fluctuations. On the other hand, at low densities,



the neutrals penetrate far into the core before being ionized, leading to very few plasma-neutral interactions in the periphery. This might reduce the importance of the ionization energy sink terms.

## 3.2 Simulation of the tokamak periphery

The simulation used for the present study considers a limited tokamak with a toroidal rail limiter on the high-field side equatorial midplane and circular flux surfaces. The simulation includes the SOL and part of the edge region, where the magnetic field lines lie on closed flux surfaces without intersecting the wall, similarly to Ref. [62]. (We remark that the GBS simulation presented here is the first to include the SOL and edge regions, as well as the self-consistent neutral-plasma interaction terms.) The normalized dimensions of the simulated tokamak are  $R_0 = 500\rho_{s0}$  and  $a_0 = 800\rho_{s0}/2\pi$ . The poloidal direction is described by the coordinate  $y$ , with  $y = 0$  at the lower side of the limiter,  $y = 400\rho_{s0}$  at the low-field side equatorial midplane, and  $y = 800\rho_{s0}$  at the upper side of the limiter. The radial extents of the simulated SOL and edge regions are  $75\rho_{s0}$  each and the separatrix is located at  $r = 0$ . The resistivity, normalized to  $R_0/c_{s0}$ , is defined as  $\tilde{\nu} = \tilde{\nu}_0(T_e/T_{e0})^{-3/2}$ , taking into account the Spitzer dependency and being  $\tilde{\nu}_0 = R_0 m_e / (1.96 c_{s0} m_i \tau_e)$ , the dimensionless parallel electron heat conductivity is  $\tilde{\kappa}_{\parallel e} = 3.16 \times 2 T_{e0} \tau_e / (3 m_e c_{s0} R_0)$ , and the dimensionless parallel ion heat conductivity is  $\tilde{\kappa}_{\parallel i} = 3.9 \times 2 T_{i0} \tau_i / (3 m_i c_{s0} R_0)$ . With the normalization parameters  $n_0 = 2 \cdot 10^{19} \text{m}^{-3}$ ,  $T_{e0} = T_{i0} = 20 \text{eV}$ , and  $B_0 = 0.5 \text{T}$ , it results  $\rho_{s0} \simeq 0.9 \text{mm}$ ,  $R_0 \simeq 44 \text{cm}$ ,  $a_0 \simeq 11 \text{cm}$ , and  $R_0/c_{s0} \simeq 10 \mu\text{s}$ . The normalized values for the resistivity and the parallel heat conductivities calculated from the parameters above ( $\tilde{\nu}=0.03$ ,  $\tilde{\kappa}_{\parallel e} = 39.6$ , and  $\tilde{\kappa}_{\parallel i} = 1.1$ ) are modified to  $\tilde{\nu} = 0.1$ ,  $\tilde{\kappa}_{\parallel e} = 10$ , and  $\tilde{\kappa}_{\parallel i} = 0.5$  to reduce the numerical cost of the simulation. The ion to electron mass ratio is set to  $m_i/m_e = 200$  for the same reason. We also impose  $E_{iz} = 30 \text{eV}$ . We note that recombination processes can be neglected at  $T_{e0} = 20 \text{eV}$  since  $\nu_{\text{rec}}/\nu_{iz} \approx 10^{-6}$  (within our simple atomic neutral model this assumption holds for  $T_e \gtrsim 2 \text{eV}$ , corresponding to  $\nu_{\text{rec}}/\nu_{iz} \lesssim 10^{-2}$ ). We remark that at the boundary of the simulation domain towards the main wall, assumed to be at a certain location between the separatrix and the solid wall, we apply vanishing Neumann boundary conditions for  $n$ ,  $\nu_{\parallel e}$ ,  $\nu_{\parallel i}$ ,  $T_e$ , and  $T_i$ , and  $\tilde{\omega} = 0$  and  $\phi = \langle \Lambda T_e \rangle_t$  ( $\Lambda \simeq 3$  and  $\langle \rangle_t$  is a moving window time average). We use open boundary conditions (vanishing Neumann) for all quantities at the boundary towards the tokamak core.

Since there is no separation between equilibrium and fluctuating quantities in the drift-reduced Braginskii equations, Eqs. (2.16)-(2.21), the plasma profiles result self-consistently from the interplay between perpendicular and parallel transport, losses

### Chapter 3. Identification of the key elements of the neutral-plasma interaction

at the sheath, ionization processes, and heat outflowing from the tokamak core to the edge region. The latter is mimicked by the temperature source terms,  $S_{T_e}$  and  $S_{T_i}$ , which are constant in time, poloidally uniform, and radially Gaussian with a width of  $5\rho_{s0}$  centered around  $r_s = -75\rho_{s0}$ , i.e. the location of the boundary of the simulated domain towards the tokamak core. In the present simulation it is assumed that the source of plasma density is solely due to ionization of neutral atoms in the simulated volume, therefore the plasma density source  $S_n$  in Eq. (2.16), mimicking the outflow of plasma density from the core, vanishes. The plasma flowing along the magnetic field lines and arriving at the limiter plates is recycled, assuming that 80% is reflected specularly and 20% is absorbed on the surface and released with a thermal distribution of 3eV, mimicking energies of neutral atoms after Frank-Condon dissociation [46, 8]. We assume the same reflection coefficient for neutrals arriving at the limiter.

To fuel the plasma and compensate for the radial plasma losses, two gas puffs on the high-field side, above and below the limiter, and a constant inflow of neutrals from the main wall (mimicking main wall recycling) are included in the simulation. The two gas puffs are toroidally constant and, together, account for 41% of the ionization. The small constant inflow of neutrals from the main wall accounts for 17% of the total ionization and the recycling at the limiter for 42%.

The gas puff inlets lie outside the simulated domain, since its outer boundary does not coincide with the physical wall. Therefore, we assume that the hydrogen molecules from the gas puff are dissociated into atoms and somewhat diffuse before entering the simulated domain. We account for this by setting the inflowing distribution function at the outer boundary,  $\mathbf{x}_b$ , to

$$f_{n,gp}(\mathbf{x}_b, \mathbf{v}) \propto \exp\left(-\frac{(y_b - y_{0gp})^2}{2\Delta y_{gp}^2}\right) \chi_{in}(\mathbf{x}_b, \mathbf{v}), \quad (3.1)$$

where  $y_b$  is the outer boundary poloidal coordinate,  $y_{0gp} = \pm 40\rho_{s0}$  is the location and  $\Delta y_{gp} = 20\rho_{s0}$  the width of the gas puff. The inflowing velocity distribution,  $\chi_{in}$ , is defined in Eq. 2.6, and we impose  $T_b = 3\text{eV}$ .

After a transient, a quasi-steady state is achieved in our simulation where sources and losses balance and the total amount of particles in the system is approximately constant. Our investigation focuses on this quasi-steady state. Poloidal snapshots of plasma density, electrostatic potential, electron and ion parallel velocities, electron and ion temperatures, neutral density, and ionization source,  $S_{iz}$ , are shown in Fig. 3.1. Poloidal profiles of the same quantities averaged in time and toroidally are displayed in Fig. 3.2. We observe strong poloidal asymmetries, particularly visible for the plasma

### 3.2. Simulation of the tokamak periphery

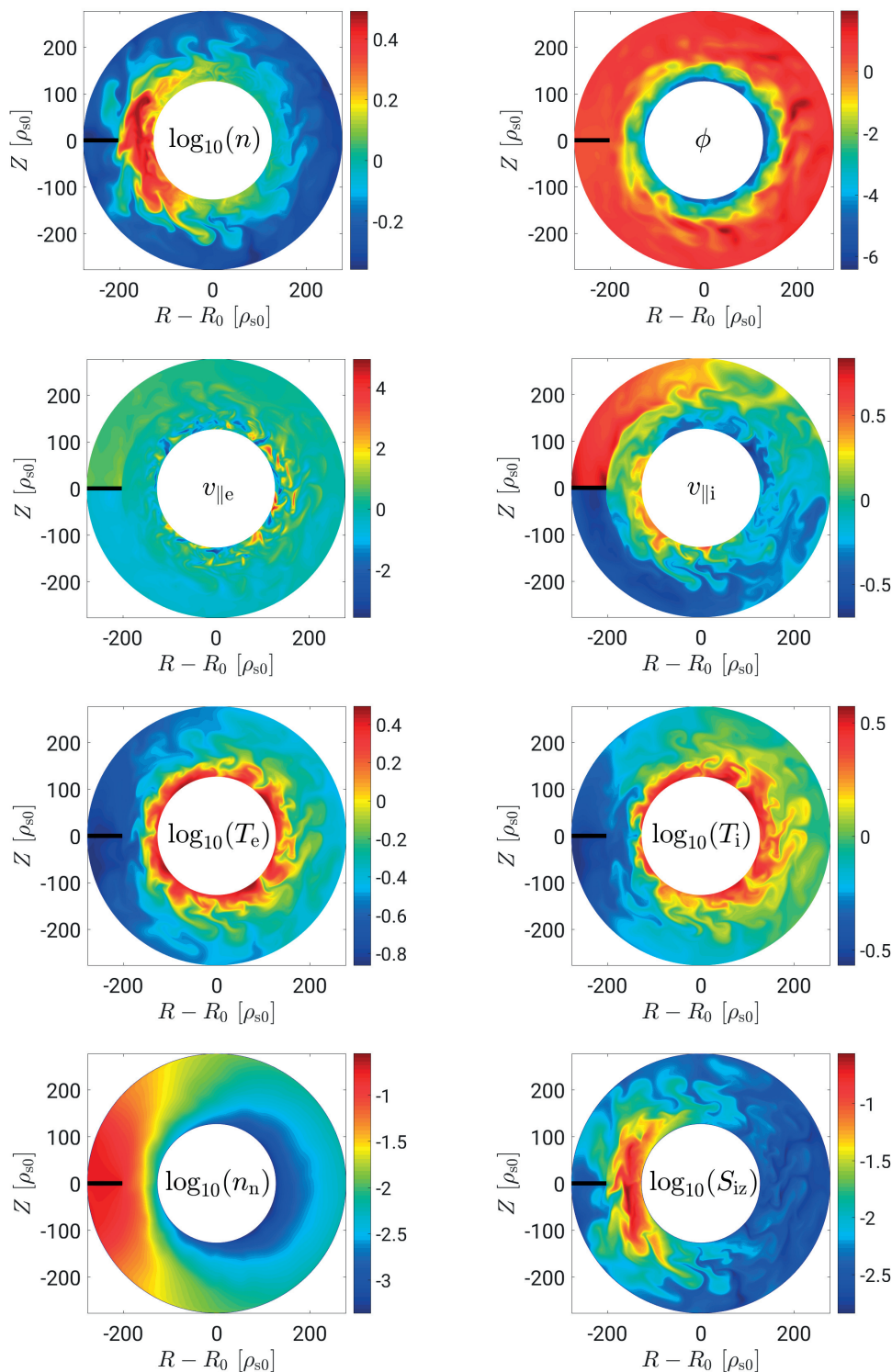


Figure 3.1 – Poloidal snapshots of plasma density, electrostatic potential, electron and ion parallel velocities, electron and ion temperatures, neutral density, and ionization rate for the simulation described in Section 3.2.

### Chapter 3. Identification of the key elements of the neutral-plasma interaction

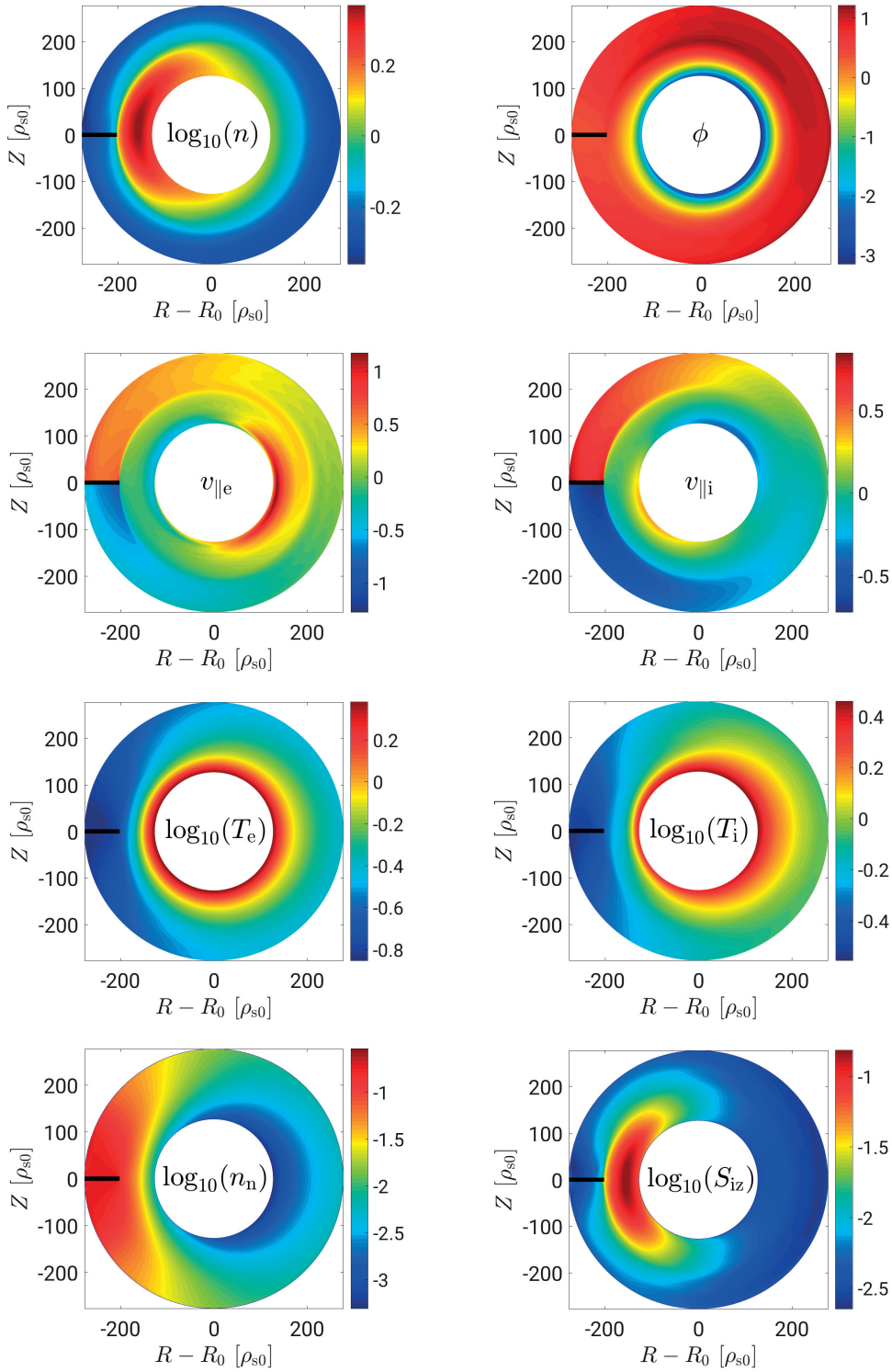


Figure 3.2 – Time-averaged poloidal profiles of plasma density, electrostatic potential, electron and ion parallel velocities, electron and ion temperatures, neutral density, and ionization rate for the simulation described in Section 3.2.

### 3.2. Simulation of the tokamak periphery

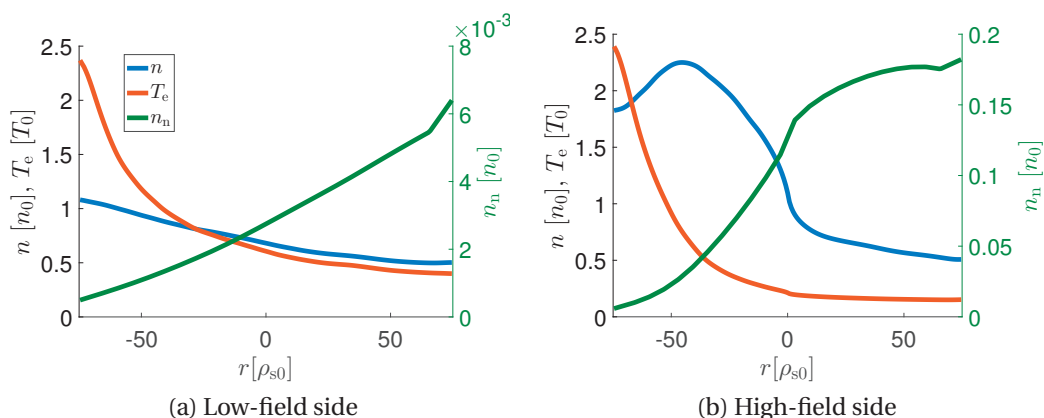


Figure 3.3 – Radial profiles of plasma density, electron temperature, and neutral density on the low-field side equatorial midplane (left,  $350\rho_{s0} < y < 450\rho_{s0}$ ), and at the high-field side, in proximity of the limiter (right,  $|y - y_{\text{limiter}}| < 50\rho_{s0}$ ), time and toroidally averaged. The simulation described in Section 3.2 is considered.

density in the edge region, which is higher on the high-field side than on the low-field side, and in the electron and ion temperatures, which are higher on the low-field side than on the high-field side. In the SOL, the electron temperature drop towards the limiter is due to the balance between radial turbulent transport, parallel heat conduction and convection, the ionization energy loss close to the limiter, and the parallel outflow of plasma to the limiter (see, e.g., our work on a refined two-point model in Chapter 4 or in Ref. [63]).

Time-averaged radial profiles of plasma density, electron temperature, and neutral density on the low-field side equatorial midplane ( $350\rho_{s0} < y < 450\rho_{s0}$ ) and at the high-field side, in proximity of the limiter ( $|y - y_{\text{limiter}}| < 50\rho_{s0}$ ) are shown in Figs. 3.3a and 3.3b, respectively. At the low-field side, the neutral density decays with a scale length of approximately  $80\rho_{s0}$  from the outer domain boundary, resulting from ionization and charge exchange processes. The plasma density decays from the core to the vessel wall with a scale length comparable to the radial domain size, approximately  $180\rho_{s0}$ . The electron temperature has a short decay length in the closed flux-surface region (approximately  $30 - 40\rho_{s0}$ ), and a decay length comparable to the one of the density in the SOL.

The equilibrium profiles show a more complex behavior around the limiter. The neutral density is almost constant in the SOL and decays in the closed flux surface region from the limiter tip towards the core with a decay length of approximately  $30\rho_{s0}$ . The plasma density peaks in the edge region where the amplitude of the ionization source is largest (see Fig. 3.2). The electron temperature decays with a short scale

## Chapter 3. Identification of the key elements of the neutral-plasma interaction

length of approximately  $25\rho_{s0}$  from the core towards the limiter, and it is almost constant along the limiter with a value of  $T_e \simeq 3\text{eV}$ . We remark that the fast decay in the edge is partly due to the ionization energy loss (proportional to the ionization source). We also note that, while the volumetric recombination rate at  $T_e \simeq 3\text{eV}$  is still quite low, molecules are expected to play an important role at this temperature, which is not captured by the present model.

In this Chapter, we discuss the impact of neutral fluctuations and the different plasma-neutral interaction terms on the equilibrium plasma profiles. We identify the interaction terms in the density, vorticity, electron and ion parallel velocity, and electron and ion temperature equations, Eqs. (2.16)-(2.21), respectively as

$$I_n = n_n v_{iz} \quad (3.2)$$

$$I_{\tilde{\omega}} = -\frac{n_n}{n} v_{cx} \tilde{\omega} \quad (3.3)$$

$$I_{v_{\parallel e}} = \frac{n_n}{n} (v_{en} + 2v_{iz})(v_{\parallel n} - v_{\parallel e}) \quad (3.4)$$

$$I_{v_{\parallel i}} = \frac{n_n}{n} (v_{iz} + v_{cx})(v_{\parallel n} - v_{\parallel i}) \quad (3.5)$$

$$I_{T_e} = \frac{n_n}{n} v_{iz} \left[ -\frac{2}{3} E_{iz} - T_e + m_e v_{\parallel e} \left( v_{\parallel e} - \frac{4}{3} v_{\parallel n} \right) \right] - \frac{n_n}{n} v_{en} m_e \frac{2}{3} v_{\parallel e} (v_{\parallel n} - v_{\parallel e}) \quad (3.6)$$

$$I_{T_i} = \frac{n_n}{n} (v_{iz} + v_{cx}) \left[ T_n - T_i + \frac{1}{3} (v_{\parallel n} - v_{\parallel i})^2 \right], \quad (3.7)$$

where we neglect the recombination term in  $I_n$ . We remind that the collisionalities depend on plasma density and electron or ion temperature (see Eqs. (2.2)-(2.4)).

### 3.3 Fluctuations in the neutral moments

We investigate the impact of neutral fluctuations on the time-averaged plasma profiles. For this purpose, we select a time window of  $\Delta t = 30R_0/c_{s0}$  during the quasi-steady state phase of the simulation described in Section 3.2, and we average the neutral density, velocity, and temperature over this time window and toroidally. We then repeat the simulation from the checkpoint at the beginning of this time window, which we define to be at  $t = 0$ , replacing the neutral moments with their averages,

which results in the plasma-neutral interaction terms

$$I_n = \langle n_n \rangle v_{iz} \quad (3.8)$$

$$I_{\tilde{\omega}} = -\frac{\langle n_n \rangle}{n} v_{cx} \tilde{\omega} \quad (3.9)$$

$$I_{v_{\parallel e}} = \frac{\langle n_n \rangle}{n} (v_{en} + 2v_{iz}) (\langle v_{\parallel n} \rangle - v_{\parallel e}) \quad (3.10)$$

$$I_{v_{\parallel i}} = \frac{\langle n_n \rangle}{n} (v_{iz} + v_{cx}) (\langle v_{\parallel n} \rangle - v_{\parallel i}) \quad (3.11)$$

$$I_{T_e} = \frac{\langle n_n \rangle}{n} v_{iz} \left[ -\frac{2}{3} E_{iz} - T_e + m_e v_{\parallel e} \left( v_{\parallel e} - \frac{4}{3} \langle v_{\parallel n} \rangle \right) \right] \\ - \frac{\langle n_n \rangle}{n} v_{en} m_e \frac{2}{3} v_{\parallel e} (\langle v_{\parallel n} \rangle - v_{\parallel e}) \quad (3.12)$$

$$I_{T_i} = \frac{\langle n_n \rangle}{n} (v_{iz} + v_{cx}) \left[ \langle T_n \rangle - T_i + \frac{1}{3} (\langle v_{\parallel n} \rangle - v_{\parallel i})^2 \right], \quad (3.13)$$

where  $\langle n_n \rangle$ ,  $\langle v_{\parallel n} \rangle$ , and  $\langle T_n \rangle$  denote the toroidal and time average of  $n_n$ ,  $v_{\parallel n}$ , and  $T_n$ .

We compare the results of this simulation that excludes the neutral fluctuations, which we label as  $\langle n_n \rangle$  simulation, with the original one, labeled as  $n_n$  simulation, in Figs. 3.4-3.6 by analyzing time traces and radial and poloidal profiles of plasma density, electrostatic potential, electron and ion parallel velocities, and electron and ion temperatures. The time traces in Fig. 3.4 are evaluated in a region at the low-field side SOL, averaged over  $10\rho_{s0} < r < 20\rho_{s0}$  and  $350\rho_{s0} < y < 450\rho_{s0}$ . The radial profiles in Fig. 3.5 are also evaluated at the low-field side,  $350\rho_{s0} < y < 450\rho_{s0}$ , and time-averaged over  $20R_0/c_{s0} < t < 30R_0/c_{s0}$ . The poloidal profiles in Fig. 3.6 are time-averaged over the same time window and they are taken in proximity of the LCFS, i.e., averaged over  $10\rho_{s0} < r < 20\rho_{s0}$ . While the fast oscillations present in the time traces deviate for the two simulations after a short time, as it is expected in a turbulent system, the quasi-steady state values remain very similar, as confirmed by the radial and poloidal profiles.

The amplitude of the neutral density fluctuations, which is typically 10 – 30% in the region of strong plasma-neutral interactions in front of the limiter, is therefore not strong enough to influence the plasma profiles significantly. We conclude that, for the plasma parameters considered in these simulations, the fluctuations of the neutral moments do not significantly affect the time-averaged profiles.

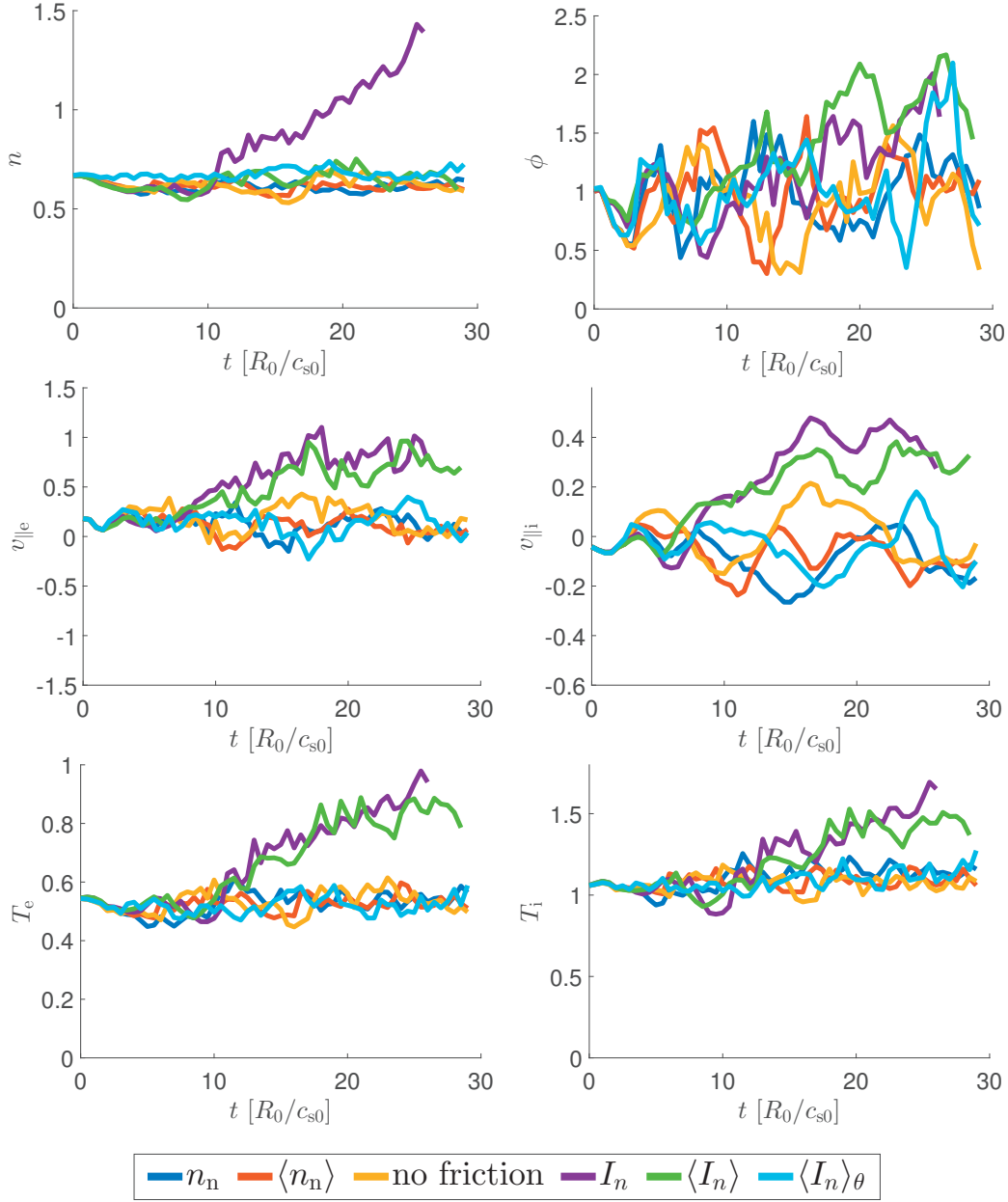


Figure 3.4 – Time traces evaluated at the SOL on the low-field side, averaged over  $10\rho_{s0} < r < 20\rho_{s0}$ ,  $350\rho_{s0} < y < 450\rho_{s0}$ , and toroidally, of plasma density, electrostatic potential, electron and ion parallel velocities, and electron and ion temperatures. The  $n_n$  simulation uses the neutral-plasma interaction terms in Eqs. (3.2)-(3.7), the  $\langle n_n \rangle$  simulation the ones in Eqs. (3.8)-(3.13), the 'no friction' simulation the ones in Eqs. (3.14)-(3.17), the  $I_n$  simulation the ones in Eqs. (3.18)-(3.19), the  $\langle I_n \rangle$  simulation the ones in Eqs. (3.24)-(3.25), and the  $\langle I_n \rangle_\theta$  simulation the ones in Eqs. (3.26)-(3.29).



### 3.3. Fluctuations in the neutral moments

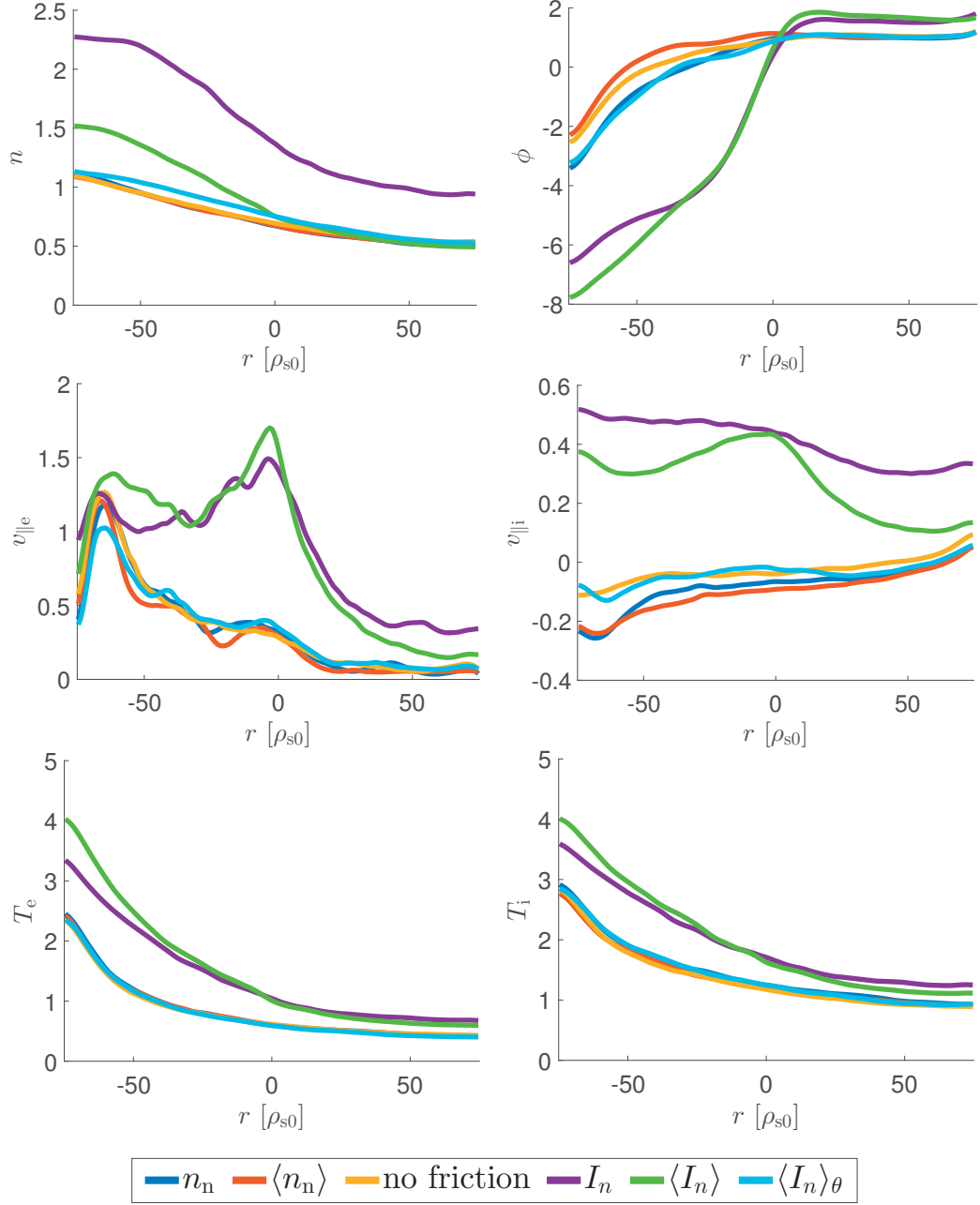


Figure 3.5 – Same as in Fig. 3.4, but for the radial profiles, averaged over  $350\rho_{s0} < y < 450\rho_{s0}$ ,  $20R_0/c_{s0} < t < 30R_0/c_{s0}$ , and toroidally, of plasma density, electrostatic potential, electron and ion parallel velocities, and electron and ion temperatures.

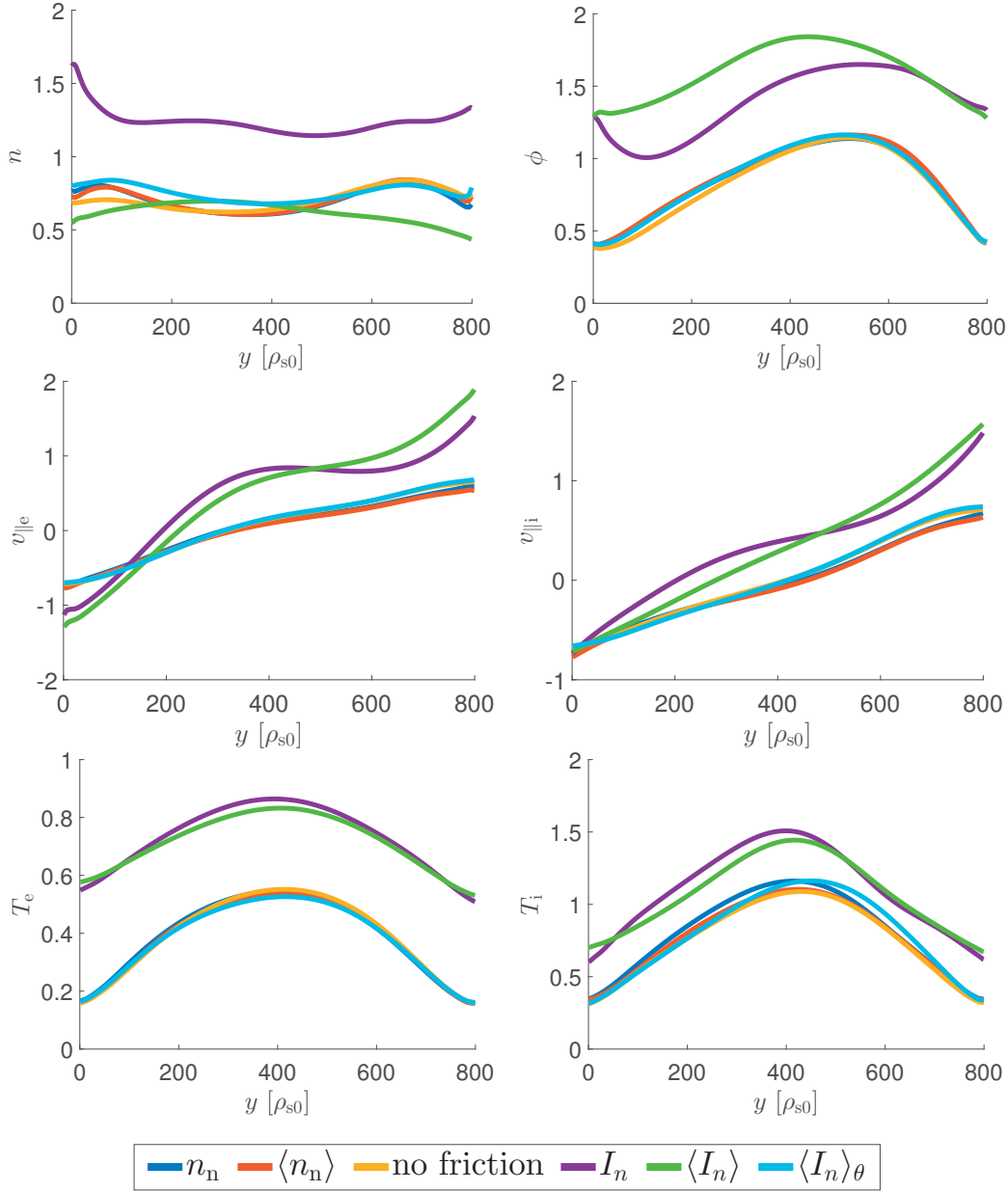


Figure 3.6 – Same as in Fig. 3.4, but for the poloidal SOL profiles, averaged over  $10\rho_{s0} < r < 20\rho_{s0}$ ,  $20R_0/c_{s0} < t < 30R_0/c_{s0}$ , and toroidally, of plasma density, electrostatic potential, electron and ion parallel velocities, and electron and ion temperatures.

## 3.4 The key interaction terms

To identify the plasma-neutral interaction processes that have an important impact in setting the time-averaged plasma profiles, we now repeat the simulation described in Section 3.2, by neglecting the plasma-neutral interaction terms related to friction (Subsection 3.4.1) and the terms associated with heat losses and temperature equilibration due to ionization and charge-exchange (Subsection 3.4.2). We use the averaged neutral moments as in Section 3.3, since neutral fluctuations do not significantly affect the time-averaged plasma profiles in the considered plasma scenario.

### 3.4.1 Friction interaction terms

Excluding the friction related terms, responsible for momentum transfer between neutrals and the plasma and for heat generation, the plasma-neutral interaction with averaged neutral moments is described by

$$I_n = \langle n_n \rangle v_{iz} \quad (3.14)$$

$$I_{T_e} = \frac{\langle n_n \rangle}{n} v_{iz} \left( -\frac{2}{3} E_{iz} - T_e \right) \quad (3.15)$$

$$I_{T_i} = \frac{\langle n_n \rangle}{n} (v_{iz} + v_{cx}) (\langle T_n \rangle - T_i) \quad (3.16)$$

$$I_{\bar{\omega}} = I_{v_{\parallel e}} = I_{v_{\parallel i}} = 0. \quad (3.17)$$

The plasma-neutral interaction terms in Eqs. (3.14)-(3.17) take into account the plasma ionization source and the heat loss and temperature equilibration due to ionization and charge exchange processes. The original simulation of Section 3.2 is repeated with the plasma-neutral interaction terms in Eqs. (3.14)-(3.17). The results of this simulation, labeled as 'no friction', are shown in Figs. 3.4, 3.5, and 3.6. Removing the friction related terms affects weakly the simulation results, confirming that these terms are rather small, and that, therefore, it is a reasonable approximation to neglect them in the considered plasma scenario. This observation is confirmed by the estimate of the importance of the friction terms in the electron temperature balance, presented in Fig. 4.3 for a similar plasma scenario.

### 3.4.2 Heat loss and temperature equilibration terms

We now zero out the plasma-neutral interaction terms present in the electron and ion temperature equations, Eqs. (2.20) and (2.21). We therefore describe the plasma-neutral interaction only through the ionization source,  $I_n$ , in the plasma density equation, Eq. (2.16), i.e.

$$I_n = \langle n_n \rangle v_{iz} \quad (3.18)$$

$$I_{\tilde{\omega}} = I_{v_{\parallel e}} = I_{v_{\parallel i}} = I_{T_e} = I_{T_i} = 0. \quad (3.19)$$

The simulation carried out with the interaction terms in Eqs. (3.18)-(3.19), labeled  $I_n$ , leads to very different results than the previous simulations, as it can be observed in Figs. 3.4, 3.5, and 3.6. In this simulation, the electron and ion temperatures raise, since the zeroed out terms describe the plasma cooling due to ionization and charge exchange processes with the neutrals. The increased electron temperature increases the ionization rate coefficient,  $\langle \nu_e \sigma_{iz}(\nu_e) \rangle_\nu$ , that, as a consequence, enhances the ionization rate,  $I_n$ . Therefore, the plasma density also increases, which in turn further amplifies the ionization term. This self-enhancing feedback would usually be inhibited by a decreasing neutral density through higher ionization rates but, since neutral fluctuations are neglected and neutral density is therefore constant in this simulation, this negative feedback is not available. In fact, the  $I_n$  simulation is not in a quasi-steady state and, due to the positive feedback loop, one might not even be reached. The radial and poloidal profiles shown in Figs. 3.5 and 3.6 are taken from averaged profiles in the time window  $20R_0/c_{s0} < t < 30R_0/c_{s0}$ .

### 3.4.3 Considerations on a simplified neutral model

From the observations in Sections 3.3, 3.4.1, and 3.4.2, we conclude that the minimal set of plasma-neutral interaction terms that result in the time-averaged plasma profiles of the fully self-consistent simulations, is given by Eqs. (3.14)-(3.17). In fact, fluctuations of the neutral moments do not affect the plasma profiles significantly for the considered scenario, and the neutral-plasma interaction terms related to friction are small, which is shown in Section 3.4.1. On the other hand, the electron energy sink due to ionization processes and the temperature equilibration term between ions and neutrals significantly affect the plasma.

Let us point out that this model of the neutral-plasma interaction terms, given by Eqs. (3.14)-(3.17), cannot be easily used to carry out simulations of the tokamak periphery, since the averaged neutral moments have to be obtained from a fully

self-consistent plasma-neutral simulation, such as the one in Section 3.2. Obtaining averaged neutral moments without self-consistent simulations of the coupled turbulent neutral-plasma system faces a major challenge. In fact, the drift-reduced Braginskii equations, Eqs. (2.16)-(2.21), we consider, do not separate quantities in an equilibrium and a fluctuating part. The time-averaged plasma profiles are therefore not imposed “a priori” and they are not known in advance. Therefore, if one wants to avoid to take into account the neutral fluctuations, one has to recalculate the neutral moments periodically to reach iteratively a self-consistent quasi-steady state, similarly to what is often done when neutral models are coupled to transport codes.

## 3.5 Further considerations

We would like to conclude the present Chapter with further considerations on the development of a simplified neutral model. We focus in particular on the averaging of the plasma-neutral interaction terms and on the poloidal asymmetry of the plasma density source due to ionization.

### 3.5.1 Averaged plasma-neutral interaction terms

In order to simplify the description of the plasma-neutral interaction, one can consider to average the complete plasma-interaction terms rather than only the neutral moments. For this purpose, we consider the two sets of interaction terms discussed in Section 3.4, Eqs. (3.14)-(3.17) and Eqs. (3.18)-(3.19), which we average, respectively, as follows:

$$I_n = \langle n_n v_{iz} \rangle \quad (3.20)$$

$$I_{T_e} = \left\langle \frac{n_n}{n} v_{iz} \left( -\frac{2}{3} E_{iz} - T_e \right) \right\rangle \quad (3.21)$$

$$I_{T_i} = \left\langle \frac{n_n}{n} (v_{iz} + v_{cx}) (T_n - T_i) \right\rangle \quad (3.22)$$

$$I_{\bar{\omega}} = I_{v_{\parallel e}} = I_{v_{\parallel i}} = 0, \quad (3.23)$$

and

$$I_n = \langle n_n v_{iz} \rangle \quad (3.24)$$

$$I_{\bar{\omega}} = I_{v_{\parallel e}} = I_{v_{\parallel i}} = I_{T_e} = I_{T_i} = 0. \quad (3.25)$$

### **Chapter 3. Identification of the key elements of the neutral-plasma interaction**

---

We perform simulations with both sets of interaction terms, repeating the simulation described in Section 3.2.

The first neutral-plasma description, Eqs. (3.20)-(3.23), which includes all the important neutral-plasma interaction terms, as discussed in Section 3.4, results in an inconsistent physical model that leads to the termination of the simulation after a very short time. (No time traces or profiles are shown for this reason.) This is due to the nature of the plasma-neutral interaction terms in the temperature equations, especially  $I_{T_e}$ . Since electrons are cooled by ionization processes, the  $I_{T_e}$  term is negative,  $I_{T_e} < 0$ . In a self-consistent simulation, such as the one in Section 3.2, the number of ionization events, and therefore the amount of energy lost due to ionization, decreases with the electron temperature, since the ionization rate is strongly dependent on the electron temperature, in particular at low temperatures. However, in the simulation with the averaged interaction terms given by Eqs. (3.20)-(3.23), the energy sink is constant, and the electron temperature decreases, eventually reaching zero and becoming negative. The neutral-plasma interaction terms that remove energy from the system, therefore, cannot be averaged as in Eqs. (3.21)-(3.22). At least the contribution of the fluctuations in the plasma quantities has to be taken into account. We note that the same is expected for other plasma energy loss mechanisms, such as impurity radiation.

Time traces and radial and poloidal profiles of the simulation with the set of interaction terms in Eqs. (3.24)-(3.25), where only the averaged density source term due to ionization is included, are shown in Figs. 3.4, 3.5, and 3.6. (The simulation is labeled as  $\langle I_n \rangle$ .) Similarly to the  $I_n$  simulation described in Section 3.4.2, we observe raising temperatures, caused by zeroing out the important heat sink terms in the electron and ion temperature equations. However, in contrast to the  $I_n$  simulation, the plasma density in this simulation is less affected with respect to the original simulation described in Section 3.2, since the complete density source term due to ionization is constant and the increasing temperature cannot lead to an increasing ionization term and the self-enhancing feedback described in Section 3.4.2. We expect that the raised plasma density in the edge region, observed in the radial profiles in Fig. 3.5, is due to the higher plasma temperatures, and not caused by the averaging of the neutral-plasma interaction term, as one can infer from the simulation in Section 3.5.2.

#### **3.5.2 On the poloidal asymmetry**

In the final simulation presented in this Chapter, we investigate the influence of the poloidal asymmetry in the ionization density source term,  $I_n$ . For this purpose, we

average the interaction term  $I_n$  not only in time and toroidally, as in Section 3.5.1, but also poloidally, which is indicated by  $\langle \rangle_\theta$ . For the other interaction terms we consider the same expressions as in Section 3.4.1, i.e.

$$I_n = \langle n_n v_{iz} \rangle_\theta \quad (3.26)$$

$$I_{T_e} = \frac{\langle n_n \rangle}{n} v_{iz} \left( -\frac{2}{3} E_{iz} - T_e \right) \quad (3.27)$$

$$I_{T_i} = \frac{\langle n_n \rangle}{n} (v_{iz} + v_{cx}) (\langle T_n \rangle - T_i) \quad (3.28)$$

$$I_{\tilde{\omega}} = I_{v_{||e}} = I_{v_{||i}} = 0. \quad (3.29)$$

We remark that, in Eqs. (3.26)-(3.29), we zero out the friction terms and the fluctuations in the neutral moments (Sections 3.3 and 3.4.1 show that their influence on the time-averaged plasma profiles can be neglected). On the other hand, we do not average the terms  $I_{T_e}$  and  $I_{T_i}$ , because, as shown in Section 3.5.1, this is unphysical.

Time traces and radial and poloidal profiles of the present simulation, labeled as  $\langle I_n \rangle_\theta$ , are displayed in Figs. 3.4, 3.5, and 3.6. The time traces and plasma profiles are very similar to the ones of the original simulation in Section 3.2. We can therefore conclude that the poloidal shape of the ionization source in the plasma density equation does not significantly impact the time-averaged plasma profiles. This indicates that the plasma particles are redistributed on a fast time scale along the magnetic field lines inside the edge region of the plasma, where the field lines lie on closed magnetic flux surfaces.





# Chapter 4

## Two-point model

In the present Chapter we investigate the electron temperature drop along the SOL magnetic field lines, and we compare the drop obtained from self-consistent turbulent simulations to the predictions of a simple two-point model. Since the agreement is not satisfactory, we then develop a refined two-point model that is shown to be in much better agreement with the simulation results than the simple model. The work discussed in the present Chapter is published in Ref. [63].

This Chapter is structured as follows. After the Introduction, in Section 4.2 we describe a simple two-point model for toroidally limited tokamaks. Section 4.3 compares the prediction of this model with the SOL turbulence simulations. In Section 4.4 we develop a more accurate two-point model, which we compare to the turbulent simulations. A discussion follows in Section 4.5.

### 4.1 Introduction

The level of impurities in the core of a tokamak and the lifetime of the plasma facing components, two critical issues on the way to fusion energy, depend on the amount of sputtering of wall material [17]. Sputtering occurs when ions, accelerated in the sheath, hit the solid wall. The acceleration is directly related to the electron and ion temperature in front of the divertor or limiter plates [8]. Therefore, understanding the physical processes that regulate the plasma temperature in front of the solid walls is of paramount importance.

Predictions of the conditions in front of the solid walls can be obtained by using

## Chapter 4. Two-point model

---

three-dimensional simulations of the SOL. However, turbulence simulations remain computationally very expensive. For this reason, progress was made in the development of simplified models that describe perpendicular turbulent transport as a diffusive process with diffusion coefficients obtained from fitting experimental data. Progress has been made to include the effect of turbulent fluctuations on neutral dynamics in these transport codes by adding stochastic fluctuations to plasma density and temperature, with characteristics similar to SOL turbulence [57, 61]. Further simplifications of these transport models lead to the so-called two-point models [8], which are widely used to obtain fast, although rough, estimates of plasma parameters in front of the solid walls. Two-point models can be used to understand basic trends of the parallel transport in the tokamak SOL. They use assumptions about the perpendicular heat and particle fluxes and a one-dimensional description of the plasma dynamics along the field lines to obtain relations between the plasma parameters at the target (the divertor or limiter plates) and upstream (a location far from the target and in contact with the core, e.g., close to the X-point, where the divertor legs begin, or at the low-field side midplane). While a number of two-point models were developed in the past for different magnetic geometries, varying in their assumptions and inclusion of different physical processes (see, e.g., Refs. [64, 65, 66, 8]), to our knowledge no direct comparison of two-point models with the results of turbulence codes was carried out. The goal of the present Chapter is to perform such a comparison between fluid turbulent simulation results and two-point models in a rather low temperature regime ( $T_e \approx 3 - 15\text{eV}$ ), and develop a two-point model that can well represent the simulation results. A two-point model that successfully predicts features of self-consistent turbulence simulations has the possibility to guide the decision about parameters of new simulations or even experiments, while reducing the number of computationally expensive turbulence simulations.

The comparison between two-point models and simulation results is performed by evaluating the electron temperature drop from the upstream to the target regions in a very simple magnetic configuration, i.e. a tokamak with circular magnetic flux surfaces and a toroidal rail limiter on the high-field side equatorial midplane. In this case, the targets are the lower and upper sides of the limiter, while the upstream location is at the low-field side equatorial midplane, halfway between the two targets. Since in the limited configuration the target location is next to the confined region, a large fraction of the recycled neutral atoms are ionized inside the LCFS, even in high density plasmas, where the ionization mean free path is short. The plasma can redistribute itself poloidally in the closed flux surface region, by moving along the magnetic field lines, and it flows back out to the SOL also at locations far from the limiter. Therefore, plasma parallel flows towards the limiter are important and, contrary to what is often done for high-density divertor configurations [8], the parallel convective heat flux cannot be

neglected. Therefore, the simplest two-point model in limited configuration is derived from the balance between perpendicular heat transport, parallel heat conduction, and parallel heat convection (used as the basic model where plasma-neutral interactions are not important in [65], or as a starting point to derive the basic divertor two-point model in [8]). In this Chapter, we compare the predictions of the simplest two-point model to first-principles turbulence simulations carried out with the GBS code. Since the comparison is not completely satisfactory, we derive a more refined two-point model rigorously from the fluid drift-reduced Braginskii equations, which are coupled to a kinetic equation for neutral atoms. The comparison of this refined model with the turbulence simulations shows very good agreement.

## 4.2 A simple two-point model for the limited SOL

In this Section we describe a simple two-point model for an axisymmetric tokamak with a toroidal limiter. We consider one flux tube, which spans along a magnetic field line from one side to the other side of the limiter. We assume that the limiter is located at the high-field side equatorial midplane. We label the direction along the flux tube with the coordinate  $s$ , which spans from  $s = -L$  at the lower side of the limiter, to  $s = +L$  at its upper side, with the upstream location,  $s = 0$ , located at the low-field side equatorial midplane.

Since in the limited configuration the target location is next to the confined region, a large fraction of the recycled neutral atoms is ionized, even in high density plasmas, inside the closed flux surface region, where the ionized particles can redistribute poloidally before they flow back into the SOL. As a consequence, large plasma flows towards the limiter are present (even far from the limiter) and the parallel convective heat flux cannot be neglected. Therefore, the simplest two-point model in limited configuration is derived from the balance between the heat deposited in the flux tube due to the radial heat transport,  $S_{Q\perp}$ , the parallel heat conduction,  $Q_{\text{cond}}$ , and the parallel heat convection,  $Q_{\text{conv}}$ , i.e.

$$Q_{\text{cond}}(s) + Q_{\text{conv}}(s) = \int_0^s S_{Q\perp}(s') ds'. \quad (4.1)$$

In Eq. (4.1) we impose  $Q_{\text{cond}}(0) = Q_{\text{conv}}(0) = 0$  because the upstream location,  $s = 0$ , is both a symmetry and a stagnation point in this simple model. The conductive heat flux is modeled by using the Spitzer heat flux coefficient,  $Q_{\text{cond}} = -\chi_{\parallel e} T_e^{5/2} dT_e/ds$ , and the convective heat flux is estimated by taking the third-order moment of a shifted Maxwellian velocity distribution and neglecting the fluid kinetic energy contribution

as  $Q_{\text{conv}} = c_{e0}\Gamma T_e$ , where  $c_{e0} = 5/2$ , and  $\Gamma = \int S_{n\perp} ds$  is the parallel particle flux, with  $S_{n\perp}$  being the particle source due to radial transport into the flux tube. Assuming  $S_{Q\perp}$  and  $S_{n\perp}$  constant along the flux tube in a limited geometry (corresponding to poloidally uniform outflow of plasma and heat), the equation that determines the electron temperature is

$$-\chi_{\parallel e} T_e^{5/2} \frac{dT_e}{ds} + c_{e0} s S_{n\perp} T_e = s S_{Q\perp}. \quad (4.2)$$

The solution of Eq. (4.2) requires a boundary condition that we apply at the magnetic pre-sheath entrance by writing the electron heat flux through the sheath entrance as  $Q_t = \gamma_e \Gamma_t T_{e,t}$ , where the subscript  $t$  indicates the target location, which is the magnetic pre-sheath entrance, and the coefficient  $\gamma_e \approx 5$  is the electron sheath transmission coefficient [8].

Equation (4.2) can be integrated numerically for a given  $S_{Q\perp}$  and  $S_{n\perp}$  by imposing the sheath boundary condition. An implicit analytical expression to relate the electron temperature at the target,  $T_{e,t}$ , to its upstream value,  $T_{e,u}$ , can also be obtained [65] and evaluated numerically.

The simplest two-point model we describe here, Eq. (4.2), is often used in the literature, e.g. as a starting point to derive the simple divertor two-point model in [8] or as a basic model in regions where plasma-neutral interactions are not important in [65].

### 4.3 Turbulent SOL simulations and comparison with the simple two-point model

To compare the simple two-point model with results from the GBS code, we consider six simulations, with a toroidal limiter on the high-field equatorial midplane,  $R_0 = 500\rho_{s0}$ ,  $2\pi a_0 = 800\rho_{s0}$ , and  $m_i/m_e = 400$ . With  $T_{e0} = T_{i0} = 10\text{eV}$  and  $B_0 = 0.5\text{T}$ , it results  $R_0 \simeq 31\text{cm}$  and  $a_0 \simeq 8\text{cm}$ . The six simulations are variants of the two basic configurations, characterized by two different plasma densities, presented in Section 2.6 and in Ref. [12]. In the low plasma density configuration, we impose  $n_0 = 5 \cdot 10^{18}\text{m}^{-3}$ . As a consequence, the resistivity normalized to  $R_0/c_{s0}$  is  $\tilde{\nu} = 0.02$ , the dimensionless parallel electron heat conductivity is  $\tilde{\kappa}_{\parallel e} = 56.0$ , and the dimensionless parallel ion heat conductivity is  $\tilde{\kappa}_{\parallel i} = 1.6$ . In the high plasma density configuration,  $n_0 = 5 \cdot 10^{19}\text{m}^{-3}$ ,  $\tilde{\nu} = 0.2$ ,  $\tilde{\kappa}_{\parallel e} = 5.6$ , and  $\tilde{\kappa}_{\parallel i} = 0.16$  are used. In addition to these two basic simulations, we repeat both simulations zeroing out the plasma interaction terms with the neutral atoms. These simulations are labeled as 'no  $n_n$ ' in the fol-

#### 4.4. A refined two-point model for limited SOL

---

lowing. For the high density case, we also carry out a simulation where we change the energy removed by each ionization to include the increased energy loss due to multiple impact ionizations, labeled as ' $E_{iz} = 30\text{eV}$ ' (in the other cases  $E_{iz} = 13.6\text{eV}$ ) and a simulation labeled 'high  $S_T$ ', where we increase the temperature sources  $S_{T_e}$  and  $S_{T_i}$  by a factor of four and the density source  $S_n$  by 30%, which results in twice the temperature and about the same density as in the basic high density simulation. (The electron temperature increases at the target from 3.8eV to 7.2eV and at the low-field side midplane from 6.4eV to 13.8eV in the closest flux-tube to the core, centered around  $r - r_{\text{LCFS}} = 15\rho_{s0}$ .) The computational domain extends for all six simulations from  $r_{\text{min}} = 0$  to  $r_{\text{max}} = 150\rho_{s0}$ . The source terms  $S_n$ ,  $S_{T_i}$ , and  $S_{T_e}$  in Eqs. (2.16-2.21), which mimic the outflow of hot plasma from the confined region to the SOL, are constant in time, poloidally uniform, and radially Gaussian around  $r_s = 30\rho_{s0}$  with a width of  $5\rho_{s0}$ . We interpret their location as the radial position of the LCFS.

The comparison with the simple two-point model is performed for five different flux tubes extending radially over  $10\rho_{s0}$  centered at  $r - r_{\text{LCFS}} = 15, 25, 35, 45, 55\rho_{s0}$ . To calculate the particle and heat deposited into each flux tube,  $S_{n\perp}$  and  $S_{Q\perp}$ , we combine the perpendicular drift terms in the GBS equations (as explained in Section 4.4), and we average them over time and over the poloidal direction.

The two-point model estimates of the temperature ratio,  $T_{e,u}/T_{e,t}$ , are then compared to the temperature ratio in the simulations. The results are shown in Fig. 4.1. While the general trend for the different radial locations in each simulation is captured by the simple two-point model, the agreement with the turbulent simulations shows relative errors that are up to 50% for this set of simulations.

## 4.4 A refined two-point model for limited SOL

In this Section, we derive a refined two-point model rigorously from the drift-reduced Braginskii equations for plasma density, Eq. (2.16), and electron temperature, Eq. (2.20). The perpendicular diffusive terms,  $\mathcal{D}_n(n)$  and  $\mathcal{D}_{T_e}(T_e)$ , included mostly for numerical reasons, can be neglected, since they are small. For typical parameters of limited tokamaks, the SOL plasma temperature is sufficiently high to neglect recombination processes. Furthermore, we neglect the terms in the electron temperature equation, Eq. (2.20), associated with the difference between parallel electron and neutral velocities since they are small compared to the other plasma-neutral interaction terms. We also assume  $j_{\parallel} = 0$  in Eq. (2.20). The validity of these assumptions is shown in Figs. 4.2 and 4.3. By making use of these assumptions, we obtain

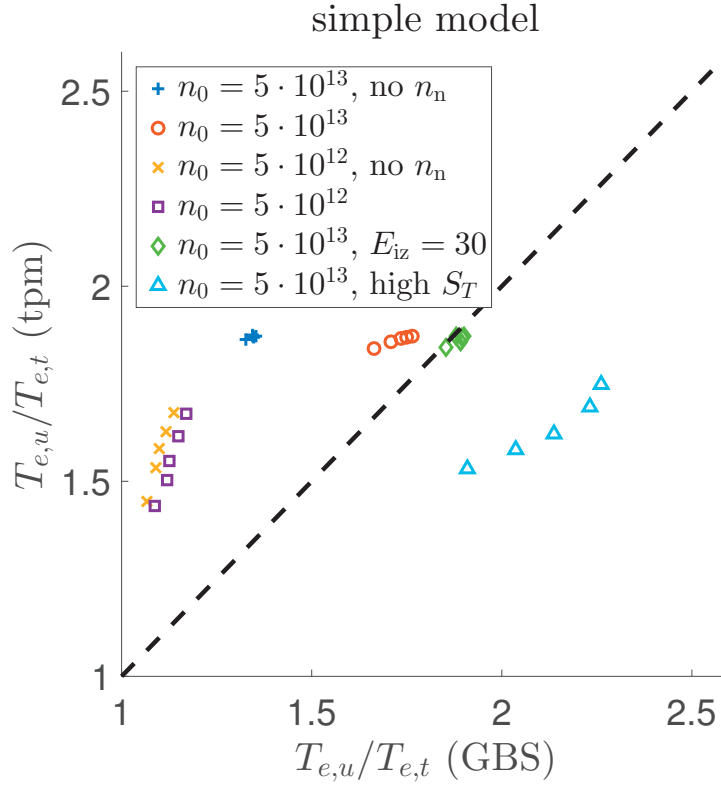


Figure 4.1 – Comparison of the ratio between the electron temperature at the upstream and target locations,  $T_{e,u}/T_{e,t}$ , predicted by the simple two-point model, Eq. (4.2), (tpm), with the results of a set of GBS simulations. For each simulation (different colors) we consider five flux tubes of width  $10\rho_{s0}$  centered at radial locations  $r - r_{\text{LCFS}} = 15, 25, 35, 45, 55\rho_{s0}$ .

$$\frac{\partial n}{\partial t} + \nabla_{\parallel}(n v_{\parallel e}) = \tilde{S}_{n\perp} + \tilde{S}_{n,n_n} \quad (4.3)$$

$$\frac{\partial T_e}{\partial t} + v_{\parallel e} \nabla_{\parallel} T_e + \frac{2T_e}{3} \nabla_{\parallel} v_{\parallel e} - \kappa_{\parallel e} \nabla_{\parallel} (T_e^{5/2} \nabla_{\parallel} T_e) = \tilde{S}_{T_e\perp} + \tilde{S}_{T_e,n_n} \quad (4.4)$$

where we combine the perpendicular transport terms (the terms related to the  $\mathbf{E} \times \mathbf{B}$  and diamagnetic drifts as well as the  $S_n$  and  $S_{T_e}$  terms) into effective perpendicular source terms,

$$\tilde{S}_{n\perp} = -\frac{1}{B}[\phi, n] + \frac{2}{eB} [C(p_e) - enC(\phi)] + S_n \quad (4.5)$$

$$\tilde{S}_{T_e\perp} = -\frac{1}{B}[\phi, T_e] + \frac{4T_e}{3eB} \left[ \frac{T_e}{n} C(n) + \frac{7}{2} C(T_e) - eC(\phi) \right] + S_{T_e}, \quad (4.6)$$

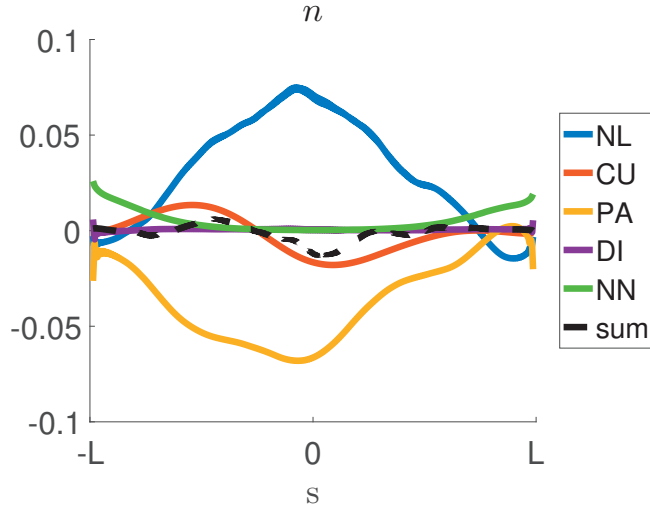


Figure 4.2 – Time-averaged plasma density balance along the field lines between the two limiter plates for the high density simulation for a flux tube with a width of  $10\rho_{s0}$  centered at  $r - r_{\text{LCFS}} = 25\rho_{s0}$ . The contributions are  $\text{NL} = -[\phi, n]/B$  ( $\mathbf{E} \times \mathbf{B}$  advection),  $\text{CU} = 2[C(p_e) - enC(\phi)]/eB$  (divergence of diamagnetic and  $\mathbf{E} \times \mathbf{B}$  flow due to curvature),  $\text{PA} = -\nabla_{\parallel}(nv_{\parallel e})$  (parallel advection),  $\text{DI} = \mathcal{D}_n(n)$  (perpendicular diffusion), and  $\text{NN} = n_n v_{\text{iz}}$  (plasma-neutral interaction term). The sum in black shows the quasi steady state balance is almost exact. It does not vanish perfectly because of the finite time-average and the finite sampling rate of the simulation results.

and we do the same for the plasma-neutral interaction terms:

$$\tilde{S}_{n,n_n} = n_n v_{\text{iz}} \quad (4.7)$$

$$\tilde{S}_{T_e, n_n} = \frac{n_n}{n} v_{\text{iz}} \left( -\frac{2}{3} E_{\text{iz}} - T_e \right). \quad (4.8)$$

To obtain an equation for the parallel electron heat flux, we multiply Eq. (4.3) by  $3T_e/2$ , and Eq. (4.4) by  $3n/2$  and we sum the two resulting equations:

$$\begin{aligned} \frac{3}{2} \frac{\partial(nT_e)}{\partial t} + \frac{3}{2} T_e \nabla_{\parallel}(nv_{\parallel e}) + \frac{3}{2} nv_{\parallel e} \nabla_{\parallel} T_e + nT_e \nabla_{\parallel} v_{\parallel e} - \frac{3}{2} n\kappa_{\parallel e} \nabla_{\parallel} (T_e^{5/2} \nabla_{\parallel} T_e) \\ = \frac{3}{2} T_e \tilde{S}_{n\perp} + \frac{3}{2} n \tilde{S}_{T_e\perp} + \frac{3}{2} T_e \tilde{S}_{n,n_n} + \frac{3}{2} n \tilde{S}_{T_e, n_n}. \end{aligned} \quad (4.9)$$

We now time-average Eqs. (4.3) and (4.9) and, rearranging the terms, we obtain

$$\nabla_{\parallel} (nv_{\parallel e}) \approx S_{n\perp} + S_{n,n_n} \quad (4.10)$$

$$\nabla_{\parallel} \left( \frac{5}{2} nv_{\parallel e} T_e \right) - v_{\parallel e} \nabla_{\parallel} (nT_e) - \chi_{\parallel e} \nabla_{\parallel} (T_e^{5/2} \nabla_{\parallel} T_e) \approx S_{Q\perp} - S_{n,n_n} E_{\text{iz}}, \quad (4.11)$$

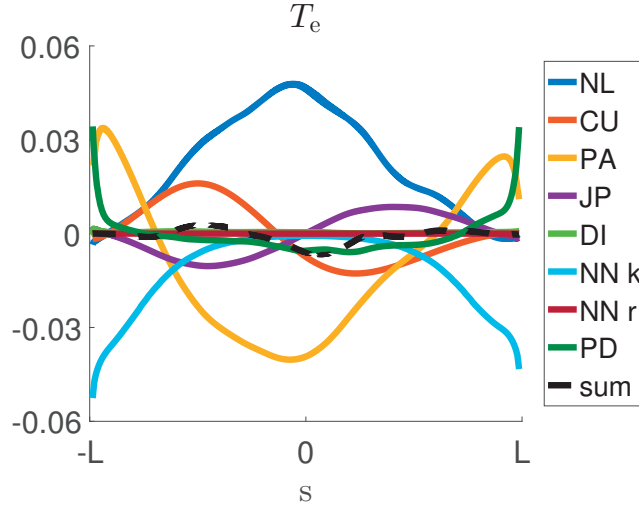


Figure 4.3 – Time-averaged electron temperature balance for the same case as in Fig. 4.2. The contributions are  $NL = -[\phi, T_e]/B$  ( $\mathbf{E} \times \mathbf{B}$  advection),  $CU = 4T_e[T_e C(n)/n + 7C(T_e)/2 - eC(\phi)]/3eB$  (curvature),  $PA = -v_{\parallel e} \nabla_{\parallel} T_e + 2T_e \nabla_{\parallel} v_{\parallel e}/3$  (parallel advection),  $JP = 0.47T_e \nabla_{\parallel} j_{\parallel}/en$  (parallel current term),  $DI = \mathcal{D}_{T_e}(T_e)$  (perpendicular diffusion),  $NN_k = n_n v_{iz}(-2E_{iz}/3 - T_e)/n$  (plasma-neutral interaction terms that we keep in the analysis),  $NN_r = n_n v_{iz} m_e v_{\parallel e}(v_{\parallel e} - 4v_{\parallel n}/3)/n - n_n v_{en} m_e 2v_{\parallel e}(v_{\parallel n} - v_{\parallel e})/3n$  (plasma-neutral interaction terms that we neglect), and  $PD = \kappa_{\parallel e} \nabla_{\parallel} (T_e^{5/2} \nabla_{\parallel} T_e)$  (parallel conduction). The sum in black shows the quasi steady state balance is almost exact. It does not vanish perfectly because of the finite time-average and the finite sampling rate of the simulation results.

with  $S_{n\perp}$  and  $S_{Q\perp}$  being the time average of  $\tilde{S}_{n\perp}$  and  $3/2(T_e \tilde{S}_{n\perp} + n \tilde{S}_{T_e\perp})$  respectively, and all quantities appearing in Eqs. (4.10-4.11) being time averaged. We note that, in agreement with simulation results, the contribution due to the correlation between fluctuations can be neglected when time-averaging the parallel transport terms and the neutral-plasma interaction terms (i.e., the terms that are the product of two or more fluctuating quantities can be evaluated as the product of the time-averaged multiplicands). On the other hand, the fluctuations have to be included in the time-averaging of the perpendicular turbulent transport terms to obtain  $S_{n\perp}$  and  $S_{Q\perp}$ . Moreover, the coefficient in the parallel Spitzer heat conductivity is defined as  $\chi_{\parallel e} = \frac{3}{2} n_{ft} \kappa_{\parallel e}$ , where  $n_{ft}$  is the average density in the flux tube.

To derive the electron temperature drop along the field lines from Eq. (4.11), we estimate the variation of the parallel electron velocity, plasma density, and neutral density along the field line. We assume that the parallel velocity varies linearly between



the two limiters, where Bohm boundary conditions are valid, i.e.

$$v_{\parallel e}(\pm L) = \pm c_s = \pm \sqrt{\frac{T_e + T_i}{m_i}} \approx \pm \sqrt{\frac{2T_e}{m_i}}, \quad (4.12)$$

obtaining therefore

$$v_{\parallel e}(s) = \frac{c_s s}{L}. \quad (4.13)$$

To estimate the plasma density profile, we integrate Eq. (4.10), that is

$$\Gamma = n v_{\parallel e} = \int S_{n\perp} + S_{n,n_n} ds. \quad (4.14)$$

The profile of the plasma density is then  $n = \Gamma / v_{\parallel e}$ . The neutral density is assumed to decay exponentially from the two limiters, i.e.

$$n_n(s) = n_n(-L) \exp [(-s - L) / \lambda_{\text{mfp},n}] + n_n(L) \exp [(s - L) / \lambda_{\text{mfp},n}], \quad (4.15)$$

with the decaying scale length given by  $\lambda_{\text{mfp},n} = \alpha_r c_s / (v_{iz} + v_{cx})$ , where  $\alpha_r$  is the reflection coefficient of the neutrals on the limiter (the velocity of the thermal neutrals from the wall is much smaller and can be neglected when estimating the effective neutral mean free path). The collision frequencies  $v_{iz}$  and  $v_{cx}$  are evaluated with the electron temperature and plasma density averaged around the target (from the limiter to a distance  $\lambda_{\text{mfp},n}$  from the limiter). The target density,  $n_n(\pm L)$ , is chosen to match the total amount of ionization in the considered flux tube. This is an input for an one-dimensional model, since neutral particles are not bound to flow along a field line and can move easily across the flux surfaces before being ionized. The ionization inside each flux tube amounts for about 5% to 20% of the recycled particles at its ends, depending mainly on plasma density and radial location of the considered flux tube. The perpendicular source terms,  $S_{n\perp}$  and  $S_{Q\perp}$ , are approximated to have a cosine distribution due to the ballooning character of the perpendicular transport, which is confirmed by the turbulence simulations.

Finally, to solve (4.11) for the electron temperature, we impose symmetry around the upstream location  $s = 0$ , where the parallel derivative of  $T_e$  vanishes. We also ensure that the velocity profile is self-consistently evaluated with  $T_e(\pm L)$  by enforcing that

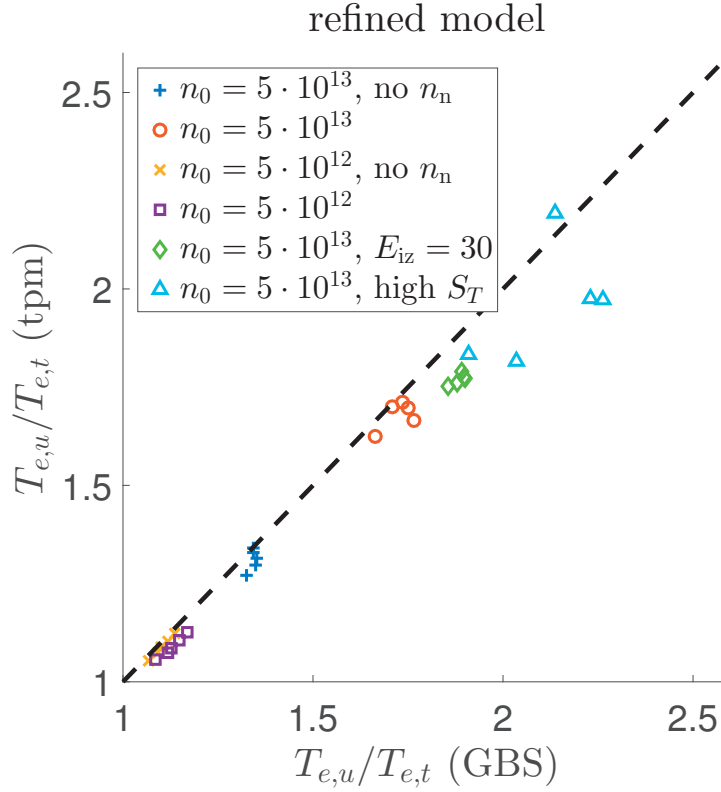


Figure 4.4 – Comparison of the ratio between the electron temperature at the upstream and target locations,  $T_{e,u}/T_{e,t}$ , as provided by the refined two-point model, Eqs. (4.10-4.11), (tpm), with the same set of GBS simulations considered in Fig. 4.1 and described in Section 4.3.

the integral of the parallel electron heat equation, Eq. (4.11), along  $s$  is satisfied, i.e.

$$\begin{aligned} \left[ \frac{5}{2} n v_{\parallel e} T_e \right]_{-L}^L &= 5L\Gamma(\pm L) T_e(\pm L) \\ &= \int_{-L}^L \left[ S_{Q\perp} - S_{n,n_n} E_{iz} + v_{\parallel e} \nabla_{\parallel} (n T_e) + \chi_{\parallel e} \nabla_{\parallel} (T_e^{5/2} \nabla_{\parallel} T_e) \right] ds, \end{aligned} \quad (4.16)$$

which describes the total heat balance in the flux tube.

With these constraints, for a given density source strength, heat source strength, and total amount of ionization in the observed flux tube, the refined two-point model, consisting of Eqs. (4.10,4.11,4.13,4.15), can be solved self-consistently. We compare its results to the set of simulations described in Section 4.3 in Fig. 4.4. The results obtained with the refined two-point model and the simulations show very good agreement.

## 4.5 Discussion

We test separately the main differences between the simple and the refined two-point model to determine the reason behind the significantly better agreement of the latter with the turbulence simulations. We observe that the shape of the source terms  $S_{n\perp}$  and  $S_{Q\perp}$  (from constant to a cosine poloidal dependence) does not improve significantly the agreement of the simple two-point model. On the other hand, a significant effect can be observed by including the plasma-neutral interaction terms. This was also observed by Tokar et al. [65], where an improved two-point model is described in which the neutrals are modeled as exponentially decaying from the limiter, similarly to the approach in the present paper, and charge-exchange collisions are taken into account through a diffusive model. To show the impact of the plasma-neutral interaction on the two-point model, we repeat the comparison between simulation results and the simple two-point model, but we include the plasma-neutral interaction terms (we assume a linear velocity profile to obtain the density, which is only needed in  $S_{n,n_n}$ ). The results, shown in Fig. 4.5 (left), reveal that, while the trend shown by the simulations is recovered, there is still a significant offset from GBS results, which disappears in the refined model (Fig. 4.4), where the compressional term,  $v_{\parallel e} \nabla_{\parallel} (nT_e)$  [Eq. (4.11)], originating from the plasma compressibility in the Braginskii equations, is included.

To investigate the effect of the compressional term, we repeat the comparison between simulation results and the refined two-point model, but we neglect the plasma-neutral interaction term. The result is shown in Fig. 4.5 (right). While for the simulations with low density and without neutrals we observe the same level of agreement between turbulence simulation and this two-point model as in the complete refined two-point model (Fig. 4.4), the same is not true for high density simulations, where the neutral mean free path is short.

From these observations we can draw two conclusions. First, when considering simulations with short neutral mean free path, it is important to account for the plasma-neutral interaction terms, and second, throughout the parameter regime explored in our simulations, the compressional term has to be taken into account for good quantitative agreement. We note that for significantly higher temperatures the impact of the compressional term might be reduced, since the parallel electron heat conductivity, increasing proportional to  $T_e^{5/2}$ , might dominate the heat equation. This has to be investigated with future simulations.

We can conclude that, by taking into account these two effects, the refined two-point model that we derived from the drift-reduced Braginskii equations for the limited

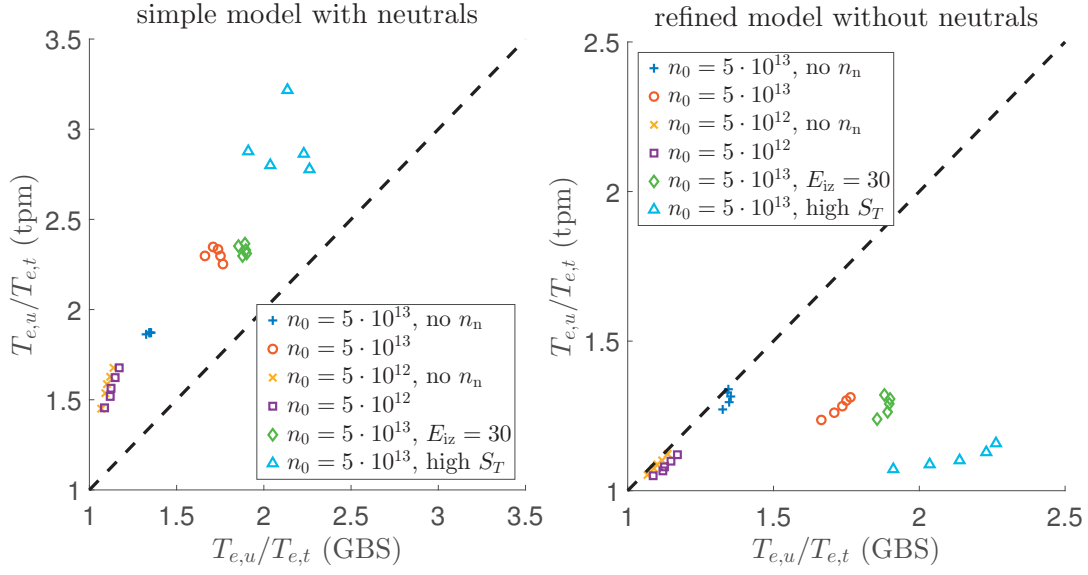


Figure 4.5 – Comparison of the ratio between the electron temperature at the upstream and target locations,  $T_{e,u}/T_{e,t}$ , for two intermediate models between the refined model (Fig. 4.4) and the simple model (Fig. 4.1). On the left, results from the the simple two-point model (Section 4.2) are shown, where the plasma-neutral interaction terms have been included to otherwise constant source terms  $S_n$  and  $S_Q$ . On the right, results from the refined model are shown, where the plasma-neutral interaction terms have been omitted.

tokamak SOL predicts accurately the ratio between upstream and target electron temperatures along a flux tube given three input parameters, namely the particle and heat sources due to perpendicular turbulent transport, and the ionization in the flux tube.

In the present work, we focus our attention on the electron temperature drop. We would like to remark that evaluating the same drop for the ion temperature brings additional difficulties. In fact, using quasi-neutrality to derive the drift-reduced Braginskii equations, we choose the electron density equation to evolve the plasma density. Therefore, identifying the parallel and perpendicular transport terms in the electron heat equation, Eq. (4.9), which is a combination of the density and electron temperature equation [Eq. (2.16) and Eq. (2.20)], is straightforward. Applying the same procedure to separate the parallel and perpendicular dynamics in an ion heat equation requires the use of the ion density equation, that involves the ion polarization velocity (see, e.g., [14]), which is more challenging. Furthermore, while neglecting the plasma current term in the electron equation is a good assumption (the 'JP' term in Fig. 4.3 is always smaller than several other dominant terms), we have observed that in the ion temperature balance (not shown) the current term can dominate the

balance at certain locations. In general, it is difficult to estimate the magnitude of the parallel current. Additionally, the complexity of the plasma-neutral interaction increases for the ions due to charge-exchange collisions, whose evaluation needs an approximation of the neutral temperature, while the neutral density suffices for the electron equations. On the other hand, the parallel heat conduction is much smaller for the ions than for the electrons, and can be neglected in most cases.



# Chapter 5

## Gas Puff Imaging

In the present Chapter, we investigate the impact of neutral density fluctuations on  $D_\alpha$  light emission, often used experimentally to study plasma structures and turbulence properties in the tokamak periphery. Our study is motivated by the fact that it is not easy experimentally to separate the contributions of neutral density, plasma density, and electron temperature fluctuations to the  $D_\alpha$  emission. The interpretation of this emission relies therefore on simulations, such as the one carried out in the present Chapter. The content of this Chapter has been submitted for publication to the Nuclear Fusion journal.

The present Chapter is structured as follows. After the Introduction, in Section 5.2 we describe the simulation that we consider for the present study and we introduce the synthetic GPI diagnostic. We describe the influence of neutral fluctuations on the  $D_\alpha$  emission in Section 5.3. A discussion follows in Section 5.4.

### 5.1 Introduction

The dynamics in the tokamak periphery results from the interplay and balance of perpendicular and parallel transport, plasma sink at the solid walls, and neutral recycling. Since radial transport is dominated by turbulent transport, measurements of the turbulent dynamics in the SOL and edge regions are of fundamental significance. Among the different experimental techniques available to study edge and SOL turbulence, we focus here on the Gas Puff Imaging (GPI) diagnostics [67, 68, 69, 70], where neutral gas is puffed into the SOL and light emission is recorded by one or several fast cameras with high temporal and spatial resolution. The local light emission stems

from atomic processes due to the interaction between the injected neutrals and the plasma, which is optically thin in typical tokamak conditions, so that most emitted photons leave the plasma without further interactions. The cameras measure the integrated local light emission along their lines of sight. The light emission is mostly toroidally localized around the gas puff valve. Therefore, using a fast camera with a tangential view, two-dimensional poloidal snapshots of the local light emission rates are approximately obtained.

While fast cameras can record the whole integrated visible spectrum, single spectral lines are usually selected by optical filters to facilitate the interpretation of the measurements. In particular, the  $H_\alpha$  line of the Balmer series is often used in hydrogen plasmas (respectively the  $D_\alpha$  line in deuterium plasmas) [67, 69, 71, 72]. It corresponds to the transition of an excited hydrogen atom in the third state,  $H^*(n=3)$ , to the second state. The  $H^*(n=3)$  excited state can originate from various atomic and molecular processes, such as molecular dissociation or electron impact excitation. (An exhaustive list of atomic and molecular processes in hydrogen plasma can be found in Ref. [46].) Due to this large variety of atomic processes and due to the difficulty to separately measure the parameters relevant to the emission process (e.g., plasma density, plasma temperature, atomic and molecular densities of the neutrals), it is not straightforward to interpret the GPI measurements. Assumptions or numerical simulations are necessary.

To interpret GPI measurements, it is often assumed that the emission rate can be estimated by [68, 69, 72]

$$D_\alpha = nn_n r_\alpha(n, T_e), \quad (5.1)$$

where  $n$  is the electron density (we assume unitary ion charge,  $Z = 1$ , in the present work),  $n_n$  is the atomic neutral density, and  $r_\alpha(n, T_e)$  is the emission rate coefficient of the  $D_\alpha$  line, which depends on the electron density and temperature and which is obtained from collisional-radiative modeling (see, e.g., Ref. [42]). The contribution of molecular dissociation is therefore neglected in Eq. (5.1). Then, two assumptions to interpret GPI images are typically made, i.e. that the structures visible in the light emission are mostly due to the plasma fluctuations, neglecting consequently the fluctuations of the neutral density, and that the plasma density and electron temperature are correlated in the tokamak SOL, which is supported by numerical turbulence simulations [71, 73]. This allows interpreting the GPI measurements and deduce properties of the SOL and edge plasma turbulence, such as spectra, spatial scales, relative fluctuation amplitudes, or blob propagation speed [67, 69, 71]. In order to reduce the number of assumptions, the contribution of plasma and neutral density



and electron temperature fluctuations to the light emission have to be measured separately. Experimentally, this is achieved by recording multiple spectral lines for the same lines of sight, taking advantage of the fact that the dependency of the emission rate coefficient,  $r(n, T_e)$ , on plasma density and electron temperature can be different for different spectral lines. This was done with helium gas puffs and different spectral He-lines, e.g., for a few lines of sight in the Alcator C-Mod tokamak [67] or, more recently, with two-dimensional images from high-speed cameras and two spectral He-lines in the TJ-II stellarator, which allowed estimating independently plasma density and neutral density fluctuations, showing the impact of neutral density fluctuations on light emission [74].

Despite the progress made on the experimental techniques, because of the complexity of the physics processes involved in the GPI measurements, numerical simulations of the turbulent plasma and the neutral particles are still necessary to confirm the validity of the used assumptions and to guide the interpretation of experimental measurements. Different types of simulations were carried out in the past for this purpose, with various assumptions, taking into account either plasma turbulence, while neglecting neutral fluctuations [71, 72, 73, 75], or simulating neutral density fluctuations, while taking averaged plasma profiles or artificial plasma fluctuations [69, 47, 57, 61]. Initial attempts to simulate plasma turbulence and fluctuating neutrals self-consistently were made with two-dimensional plasma simulations and mono-energetic neutrals [36], or with a diffusive neutral model without the back-reaction on the plasma [39].

Our goal is to investigate the impact of neutral density fluctuations on the light emission around the diagnostic gas puff, in particular we focus on the Balmer  $D_\alpha$  line. For this purpose, we use a three-dimensional turbulence simulation of a limited tokamak SOL and edge. The simulation includes two gas puffs around the toroidal rail limiter on the high-field side that fuel the plasma, and a small diagnostic gas puff on the low-field side equatorial midplane.

## 5.2 Simulation and GPI diagnostics

The simulation considered in this study is based on the simulation presented in Section 3.2, where we include a small diagnostic gas puff on the low-field side equatorial midplane. To simplify the geometry of our simulation, we assume that the diagnostic gas puff is toroidally constant. Moreover, we impose that it injects neutrals with the same distribution function as the two fueling gas puffs, Eq. (3.1), but with lower

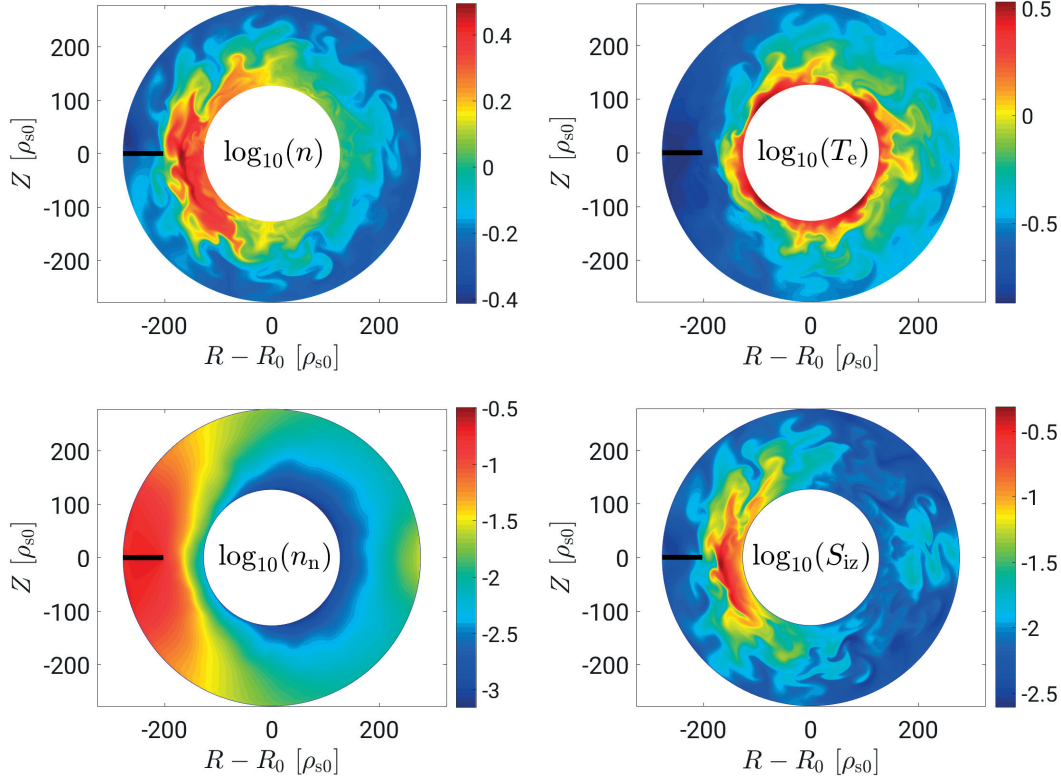


Figure 5.1 – Poloidal snapshots of plasma density, electron temperature, neutral density, and ionization rate, for the simulation considered in the present Chapter and described in Section 5.2.

amplitude. This diagnostic gas puff does not contribute significantly to the plasma fueling (it accounts for approximately 5% of the ionization in the simulation), as we verified by comparing the simulation to the one in Section 3.2. The same can also be inferred from Fig. 5.1, where we show poloidal snapshots of plasma density, electron temperature, neutral density, and ionization source,  $S_{iz}$ . One can observe that  $S_{iz}$  is rather small at the low-field side around the diagnostic gas puff. We note that toroidally constant gas puffs are atypical in experiments. However, our results are not significantly affected by the geometrical details of the gas puff since, in the present work, we do not address the issue of the integration of the signal along the lines of sight of a camera, for which a toroidally localized gas puff is needed, but we analyze the local light emission.

Radial profiles at the low-field side equatorial midplane, where the subsequent investigations on plasma and neutral fluctuations are performed, are shown in Fig. 5.2 for plasma density, electron temperature, and neutral density. The neutral density decays approximately exponentially with a scale length of  $60\rho_{s0}$  from the outer do-

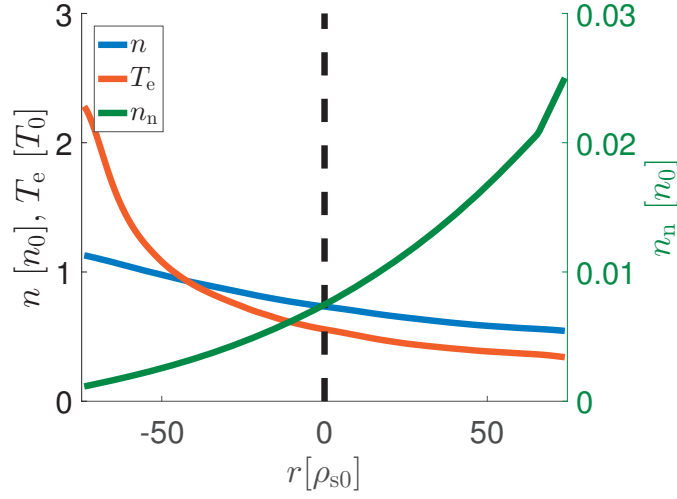


Figure 5.2 – Radial profiles of plasma density, electron temperature, and neutral density at the low-field side equatorial midplane, time and toroidally averaged.

	$T_e$ [eV]	1	10	100
$r_{D_\alpha}, n_0 = 5 \cdot 10^{18} m^{-3}$ [ $m^3/s$ ]		$2.64 \cdot 10^{-20}$	$8.89 \cdot 10^{-16}$	$2.25 \cdot 10^{-15}$
$r_{D_\alpha}, n_0 = 5 \cdot 10^{19} m^{-3}$ [ $m^3/s$ ]		$1.89 \cdot 10^{-16}$	$4.39 \cdot 10^{-16}$	$1.27 \cdot 10^{-15}$

Table 5.1 – Values of the emission coefficient  $r_{D_\alpha}$  for  $n_0 = 5 \cdot 10^{18} m^{-3}$  and  $n_0 = 5 \cdot 10^{19} m^{-3}$ .

main boundary, resulting from ionization and charge exchange processes. We define this scale length as the effective mean free path of the neutrals,  $\lambda_{\text{mfp},n}$ . On the other hand, the plasma density decays from the core to the vessel wall with a scale length of approximately  $180\rho_{s0}$ . The electron temperature has a shorter decay length in the closed flux-surface region closest to the core (approximately  $20 - 30\rho_{s0}$ ), which becomes comparable to the one of the density in the SOL.

We focus on the local emission rate of the Balmer  $D_\alpha$  line, which we calculate as

$$D_\alpha = n_e n_n r_{D_\alpha}(n_e, T_e), \quad (5.2)$$

where  $r_{D_\alpha}$  is the emission coefficient that depends on electron density and temperature as tabulated in the OpenADAS database [42]. Values of the  $r_{D_\alpha}$  emission coefficient are shown in Fig. 5.4 and Table 5.1. A snapshot of the  $D_\alpha$  emission rate is shown in Fig. 5.3 on the full poloidal cross-section. Figure 5.5 displays the temporal evolution of the normalized  $D_\alpha$  fluctuations in the region in front of the diagnostic gas puff around the low-field side equatorial midplane. (This region is indicated by a yellow dotted contour in Fig. 5.3.) Normalized  $D_\alpha$  emission fluctuations are defined

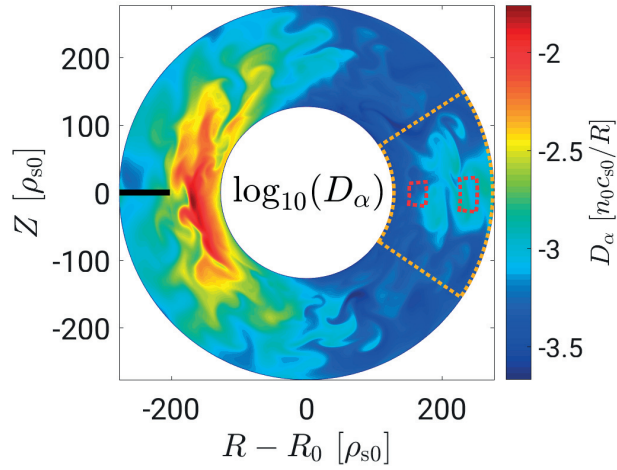


Figure 5.3 – Poloidal snapshot of the  $D_\alpha$  emission rate. The large yellow dotted area indicates the spatial region shown in Figs. 5.5, 5.6, and 5.12. The smaller red dotted areas indicate the spatial regions where the joint probabilities shown in Figs. 5.9 and 5.10 are calculated.

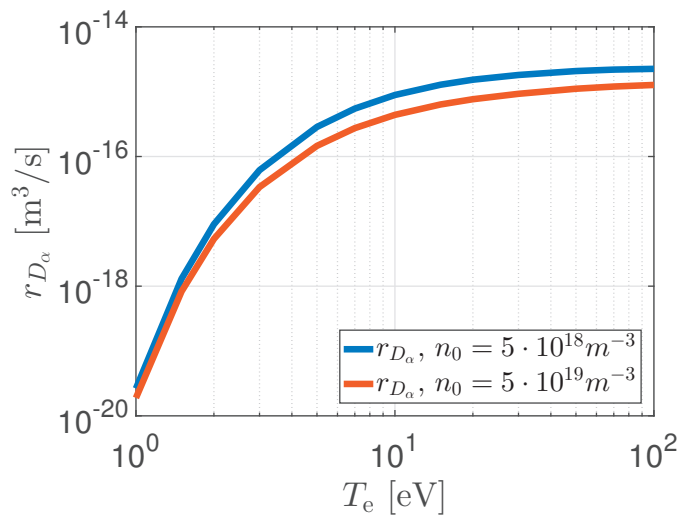


Figure 5.4 – Values of the emission coefficient  $r_{D_\alpha}$  for  $n_0 = 5 \cdot 10^{18} m^{-3}$  and  $n_0 = 5 \cdot 10^{19} m^{-3}$ .

### 5.3. Impact of neutral fluctuations on GPI

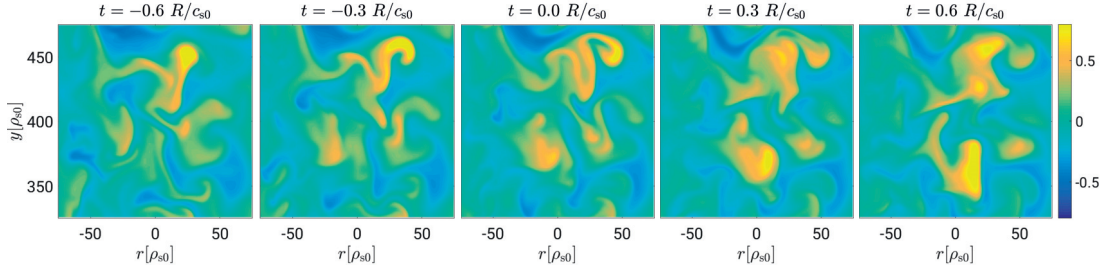


Figure 5.5 – Five snapshots, separated by  $0.3R_0/c_{s0} \simeq 3\mu s$ , representing normalized fluctuations of  $D_\alpha$  light emission,  $(D_\alpha - \langle D_\alpha \rangle)/\langle D_\alpha \rangle$ , in front of the gas puff. The considered spatial domain is indicated by a yellow dotted contour in Fig. 5.3. The LCFS is located at  $r = 0$  and the low-field side equatorial midplane is at  $y = 400\rho_{s0}$ . The snapshots in Figs. 5.1, 5.3, 5.6, and 5.12 are evaluated at  $t = 0$ .

as  $(D_\alpha - \langle D_\alpha \rangle)/\langle D_\alpha \rangle$ , where  $\langle D_\alpha \rangle$  denotes the toroidal and time average of  $D_\alpha$ . We note that the toroidal average can be performed since an axisymmetric system is investigated, and the time average is taken over a time window of  $\Delta t = 40R_0/\rho_{s0}$  that covers several fluctuation times during the quasi-steady state phase of the simulation. Similar definitions apply to other quantities.

### 5.3 Impact of neutral fluctuations on GPI

The neutral density in the SOL and edge regions is not easily measured experimentally. It is therefore difficult to disentangle the contributions of plasma density, electron temperature, and neutral density fluctuations to the fluctuations in the  $D_\alpha$  emission, Eq. (5.2). To investigate the impact of neutral density fluctuations on the  $D_\alpha$  emission, we evaluate it by using the averaged neutral density:

$$D_{\alpha\langle n_n \rangle} = n_e \langle n_n \rangle r_{D_\alpha}(n_e, T_e), \quad (5.3)$$

removing thereby the neutral density fluctuations, while keeping plasma density and electron temperature fluctuations.

We show  $D_\alpha$  and  $D_{\alpha\langle n_n \rangle}$  in Fig. 5.6 (left and middle panels) and their normalized difference in Fig. 5.6 (right panel). While  $D_\alpha$  and  $D_{\alpha\langle n_n \rangle}$  show similar spatial patterns, neglecting neutral density fluctuations leads to errors of the order of 30% in the intensity of the light emission, in particular in the closed flux-surface region. This therefore shows that the local  $D_\alpha$  emission amplitude might be significantly influenced by neutral fluctuations.

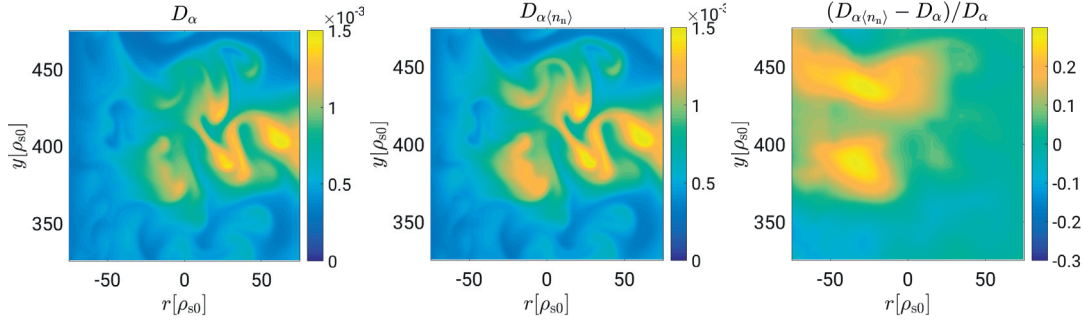


Figure 5.6 – Snapshots of  $D_\alpha$  emission (left) and  $D_{\alpha\langle n_n \rangle}$  emission, evaluated by removing the contribution of neutral density fluctuations (middle), and their relative difference (right).

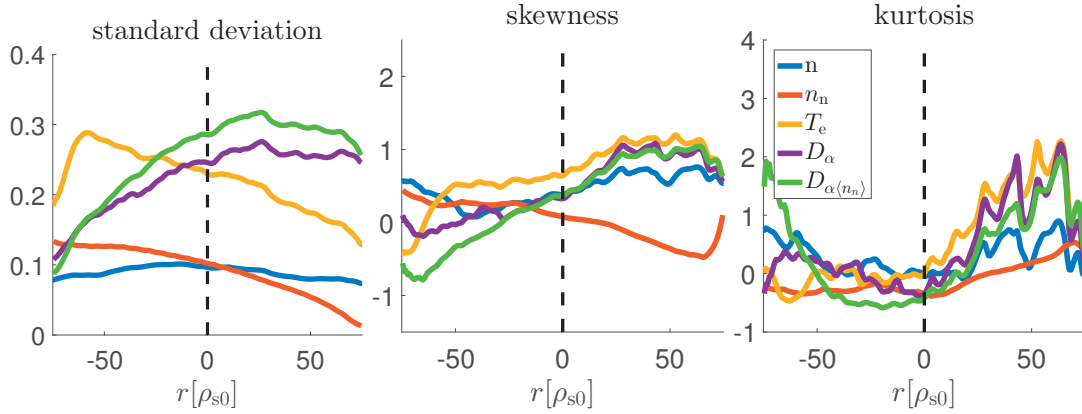


Figure 5.7 – Radial profiles of standard deviation (left), skewness (middle), and kurtosis (right) of normalized plasma and neutral density, electron temperature, and  $D_\alpha$  fluctuations with and without neutral density fluctuations at the low-field side midplane.

To investigate the impact of neutral fluctuations on other typical quantities obtained from GPI diagnostics, we evaluate the standard deviation, the skewness, the kurtosis, the autocorrelation time ( $\tau_{\text{auto}}$ ), and the radial and poloidal correlation lengths ( $L_{\text{rad}}$  and  $L_{\text{pol}}$ ) from the normalized  $D_\alpha$  and  $D_{\alpha\langle n_n \rangle}$  fluctuations respectively. These are shown in Figs. 5.7 and 5.8.

The standard deviation of the normalized  $D_{\alpha\langle n_n \rangle}$  emission in Fig. 5.7 (left panel) is up to 20% larger than the standard deviation of the  $D_\alpha$  emission in the SOL and their difference decreases when approaching the core. In addition, in the SOL we also observe that  $D_\alpha$  fluctuations are larger than  $n$ ,  $n_n$ , and  $T_e$  fluctuations, displaying also a different radial dependence. The skewness of the turbulent fields is analysed in Fig. 5.7, middle panel. We note that the skewness of  $D_\alpha$  and  $D_{\alpha\langle n_n \rangle}$  are very similar in the SOL, and both of them follow the skewness of plasma density and electron temperature

### 5.3. Impact of neutral fluctuations on GPI

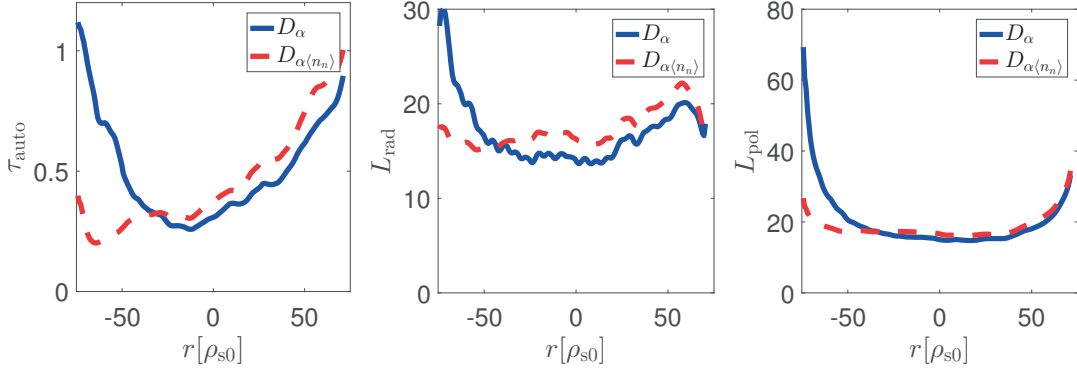


Figure 5.8 – Radial dependence of autocorrelation time and correlation lengths along the radial and poloidal direction for the  $D_\alpha$  emission with and without neutral fluctuations.

and increase radially. On the other hand, we observe a difference between the  $D_\alpha$  and  $D_{\alpha(n_n)}$  skewness in the confined region, where they are also quite different with respect to the skewness of plasma density and electron temperature. The skewness of the neutral density decreases radially and is negative in the SOL and positive in the edge. Similar remarks can be made for the kurtosis, Fig. 5.7 (right panel), namely,  $D_\alpha$  and  $D_{\alpha(n_n)}$  show similar behavior in the SOL region, and a discrepancy in the confined region.

To evaluate  $\tau_{\text{auto}}$ ,  $L_{\text{rad}}$ , and  $L_{\text{pol}}$ , we use the definitions in Refs. [71] and [72], i.e.

$$L = 1.66 \frac{\delta}{\sqrt{-\ln C_{ij}}} \quad (5.4)$$

and

$$C_{ii}(\tau_{\text{auto}}) = \frac{1}{2}, \quad (5.5)$$

where  $\delta$  is the distance between the two positions (experimentally the lines of sight)  $i$  and  $j$ , and  $C_{ij}$  is the zero-time-delay cross-correlation function between the signals at the same positions. For our analysis we choose  $\delta = 3\rho_{s0}$  (the results do not depend on the choice of  $\delta$  for  $1.5\rho_{s0} \lesssim \delta \lesssim 10\rho_{s0}$ ).

Radial profiles of  $\tau_{\text{auto}}$ ,  $L_{\text{rad}}$ , and  $L_{\text{pol}}$  are shown in Fig. 5.8. Neutral density fluctuations do not have a large impact on these measurements in the SOL. On the other hand, an effect of neutral density fluctuations can be observed in the confined region towards the core, similarly to what is observed for the statistical moments in Fig. 5.7. We note that converting normalized to dimensional units reveals  $\tau_{\text{auto}} \approx 3 - 8\mu\text{s}$ ,  $L_{\text{rad}} \approx$

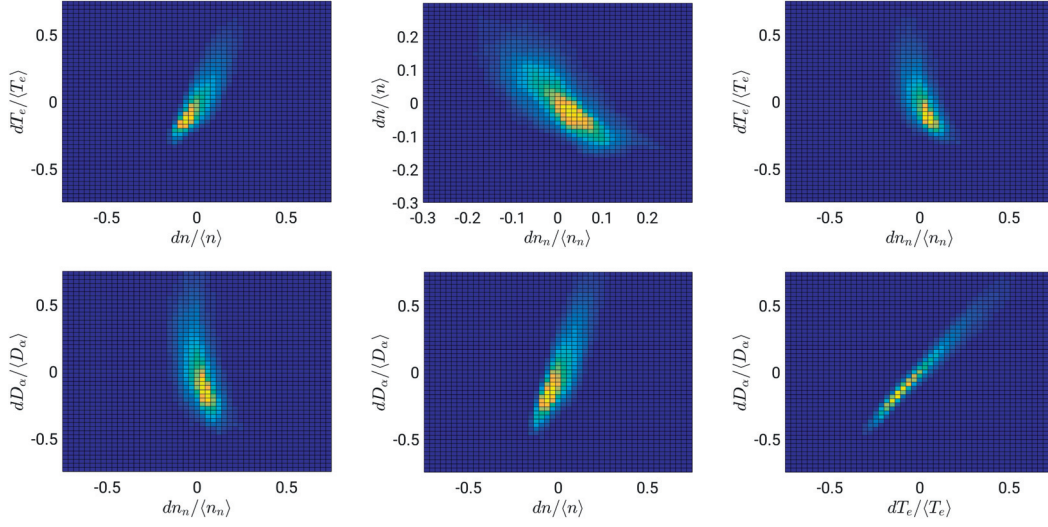


Figure 5.9 – Joint probability function between fluctuations of plasma density, electron temperature, neutral density, and  $D_\alpha$  emission in front of the low-field side diagnostic gas puff in the SOL ( $25\rho_{s0} < r < 50\rho_{s0}$ , right red dotted region in Fig. 5.3).

1.5 – 2cm, and  $L_{\text{pol}} \approx 2\text{cm}$ , values that are similar to the ones found in the C-Mod tokamak [71, 72].

## 5.4 Discussion

We analyze the link between neutral and plasma fluctuations to explain the impact of neutral density fluctuations on the  $D_\alpha$  emission rate. We first study the correlations and anti-correlations between  $n$ ,  $n_n$ ,  $T_e$ , and  $D_\alpha$  by evaluating their joint-probability functions. These are presented for the SOL ( $25\rho_{s0} < r < 50\rho_{s0}$ ) in Fig. 5.9, and for the edge ( $-50\rho_{s0} < r < -25\rho_{s0}$ ) in Fig. 5.10. Both regions (SOL and edge) show that plasma density and electron temperature fluctuations are correlated (an observation made also in other SOL turbulence simulations [71, 73]). On the other hand, the neutral density is anti-correlated with both plasma density and electron temperature, particularly in the SOL. The anti-correlation between  $D_\alpha$  emission and neutral density, observed in the SOL, disappears in the confined region, and the correlation between  $D_\alpha$  emission and both plasma density and electron temperature is much sharper in the SOL than in the edge.

To quantify the correlations, we introduce Spearman’s rank correlation coefficient [76],  $r_s$ , which indicates if a correlation between two quantities is monotonically increasing (in this case  $r_s = 1$ , and the two quantities are correlated), decreasing (in this case



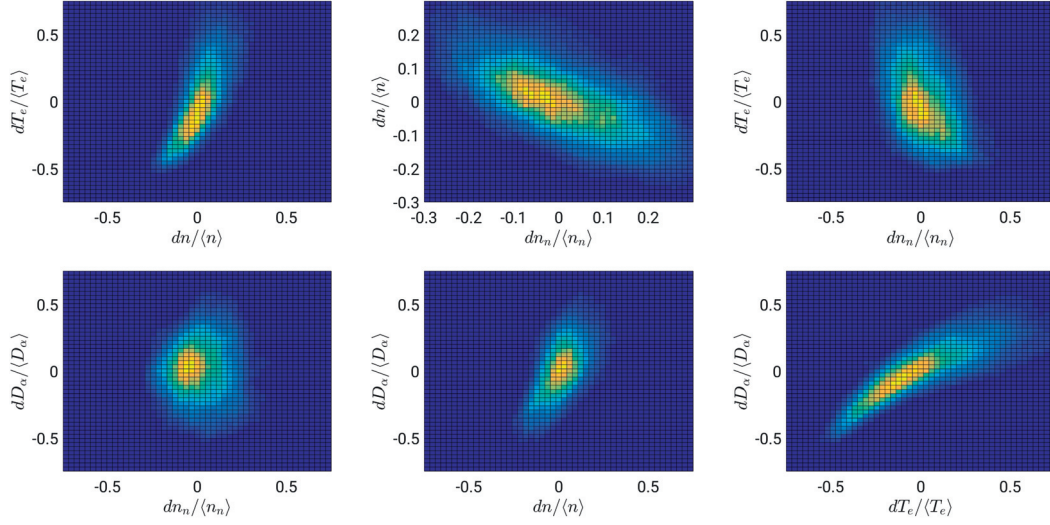


Figure 5.10 – Same plots as in Fig. 5.9 in the edge ( $-50\rho_{s0} < r < -25\rho_{s0}$ , left red dotted region in Fig. 5.3).

$r_s = -1$ , and the two quantities are anti-correlated), or it is somewhere in-between ( $-1 < r_s < 1$ ), independently of the type of correlation (e.g., linear or quadratic). Radial profiles of  $r_s$  evaluated at the low-field side equatorial midplane are shown in Fig. 5.11 for the six combinations of neutral and plasma density, electron temperature, and  $D_\alpha$  emission. In the SOL, a clear correlation between plasma density, electron temperature, and  $D_\alpha$  emission is visible, while one observes anti-correlation between the neutral density and the other three quantities. All correlation and anti-correlation coefficients decrease towards the core, and the anti-correlation of neutral density and  $D_\alpha$  emission in the SOL even turns into a correlation in the confined region. This transition happens at  $r \simeq -35\rho_{s0}$ , which is also, approximately, the radial location inside which the skewness (Fig. 5.7, middle panel) and the correlation quantities ( $\tau_{\text{auto}}$ ,  $L_{\text{rad}}$ , and  $L_{\text{pol}}$ , Fig. 5.8) differ if they are evaluated from  $D_\alpha$  or  $D_{\alpha\langle n_n \rangle}$ . In fact, for  $r \lesssim -35\rho_{s0}$  neutral fluctuations impact not only the  $D_\alpha$  fluctuation amplitude, but also their spatial structures and fluctuation properties, as it can be observed in the skewness and in the correlation lengths profiles.

These observations can be explained by the analysis of typical turbulence snapshots. The normalized fluctuations of plasma density, electron temperature, neutral density, and  $D_\alpha$  emission, in the region in front of the diagnostic gas puff, are shown in Fig. 5.12. First, we observe very similar spatial structures in plasma density and electron temperature, confirming that these two quantities are strongly correlated in the whole considered region. Second, for the correlation between the neutrals and the plasma quantities, we distinguish two regions, the region  $r \gtrsim -35\rho_{s0}$  (approximately

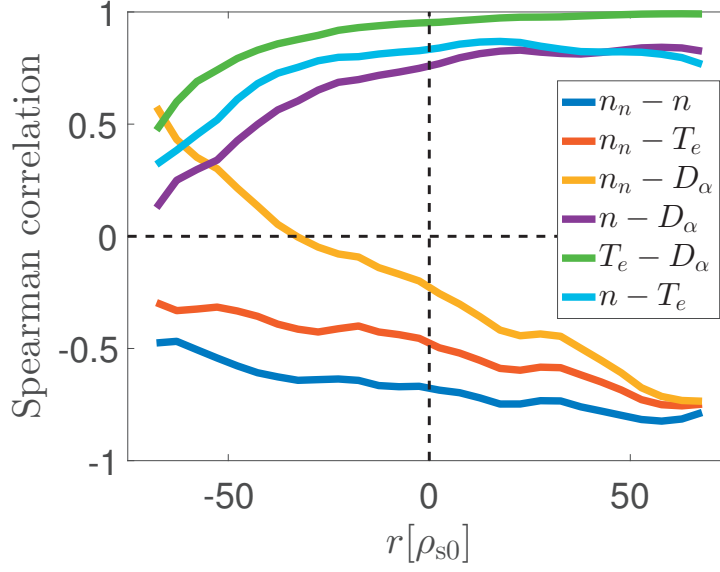


Figure 5.11 – Radial profiles of the Spearman correlation coefficient between plasma and neutral density, electron temperature, and  $D_\alpha$  emission.

the SOL), which is closer to the outer boundary than the effective neutral mean free path,  $\lambda_{\text{mfp},n} \approx 60\rho_{s0}$ , and the region  $r \lesssim -35\rho_{s0}$ , which is further away from the outer boundary than  $\lambda_{\text{mfp},n}$ . In the  $r \gtrsim -35\rho_{s0}$  region, positive fluctuations in plasma density and electron temperature (yellow structures) clearly correlate with negative fluctuations in the neutral density (blue structures). This anti-correlation is due to the fact that, while the diagnostic gas puff, the main source of neutral particles at the low-field side midplane, is constant and independent of the local plasma parameters, neutral particles are lost because of ionization processes, which occur with higher probability in regions where the plasma is denser and hotter. Therefore, regions of high plasma density and electron temperature correspond to regions of low neutral density. On the other hand, in the  $r \lesssim -35\rho_{s0}$  region, the neutral density is determined not only by the local plasma properties (a weak anti-correlation between  $n_n$  and both  $n$  and  $T_e$  is visible), but also by the plasma properties in the SOL region radially outward from the edge location where the observations are made. In Fig. 5.12, the enhanced SOL plasma density and electron temperature, observed at  $y \gtrsim 400\rho_{s0}$ , reduce the neutral density not only in the SOL, but also radially inward. This phenomenon is referred to as shadowing [47, 69]. On the other hand, for  $y \lesssim 350\rho_{s0}$ ,  $n$  and  $T_e$  are rather low and let the neutrals penetrate much further than on average. This leads to positive fluctuations in neutral density close to the core, a sort of inverse shadowing event. Because of the non-locality of the shadowing, the neutral density fluctuations in the confined region close to the core are not as anti-correlated with the plasma density and temperature as in the SOL (see Fig. 5.11). In fact, the  $D_\alpha$  emission close

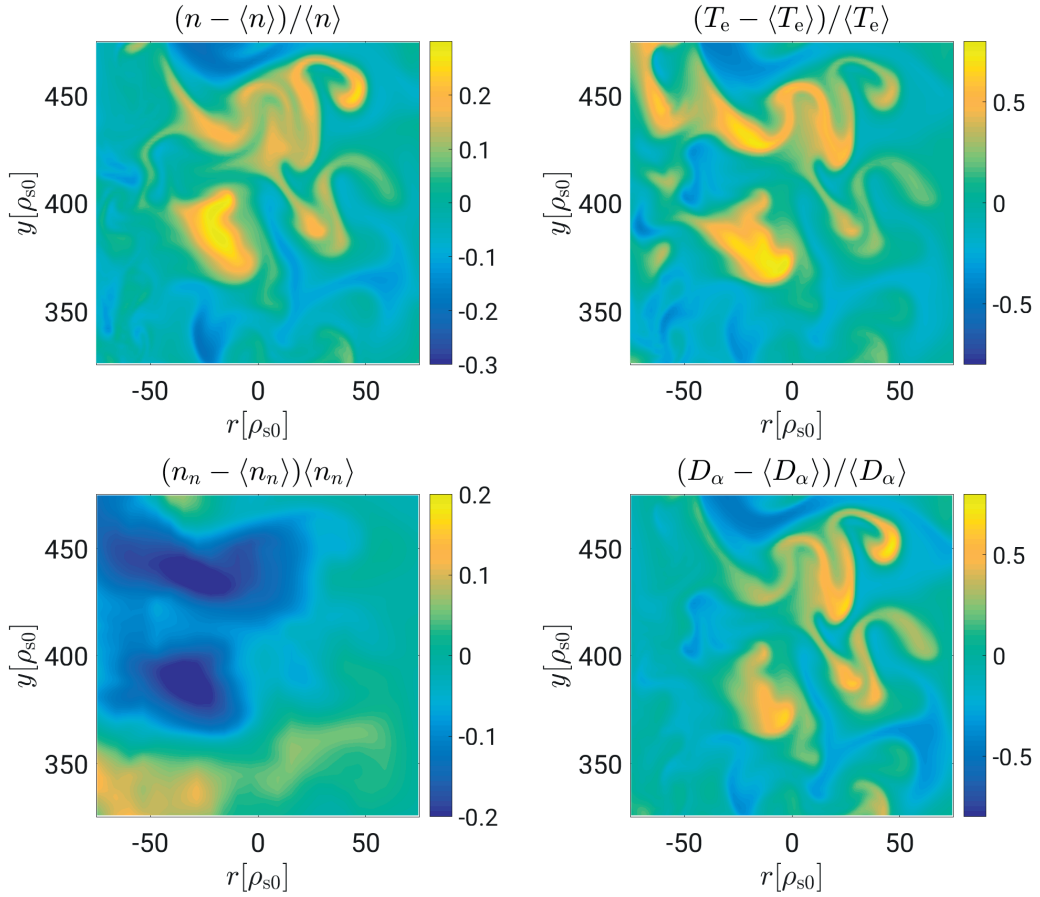


Figure 5.12 – Poloidal snapshots in front of the low-field side gas puff (this region is contoured by a yellow dotted line in Fig. 5.3) of the normalized fluctuations of plasma density (top left), electron temperature (top right), neutral density (bottom left), and  $D_\alpha$  emission (bottom right).

to the core is larger when neutrals can penetrate further into the plasma than on average, which is seen in the correlation between  $n_n$  and  $D_\alpha$  in the inner part of the edge region (see Fig. 5.11). As a consequence, at a distance larger than  $\lambda_{\text{mfp},n}$  from the outer boundary, neutral density fluctuations can have a significant influence on the statistical moments and turbulence properties evaluated from  $D_\alpha$  emission.

We have applied the same synthetic GPI diagnostics to a similar simulation with approximately twice the plasma density, and therefore with approximately half the neutral mean free path,  $\lambda_{\text{mfp},n} \approx 30\rho_{s0}$ . In this simulation, we observe that the transition from the region where neutrals and  $D_\alpha$  emission are clearly anti-correlated to the region where the two quantities are correlated, observed in the radial plot of the Spearman correlation coefficients (similar to Fig. 5.11), occurs approximately at a distance of  $40\rho_{s0}$  from the outer domain boundary. This confirms that  $\lambda_{\text{mfp},n}$  is a

## Chapter 5. Gas Puff Imaging

---

dominating factor in setting the region where the shadowing effect occurs and has a significant impact on GPI measurements.

The relevance of the shadowing effect in interpreting the GPI measurements depends on the experimental set-up and the sensitivity and dynamic range of the cameras. In fact, the location where the shadowing becomes important is related to  $\lambda_{\text{mfp},n}$ , which depends on the experimental conditions. At the same time, the average intensity of the  $D_\alpha$  emission decreases significantly at distances larger than  $\lambda_{\text{mfp},n}$  (see Fig. 5.6, left panel) and therefore it might be recordable only by sensitive cameras with a high dynamic range.

# Chapter 6

## Summary and outlook

The understanding of the interaction between neutral atoms and turbulent plasma in the tokamak periphery, focus of the present Thesis, is a crucial step in the development of fusion reactors. In fact, this interaction sets the boundary conditions for the burning plasma in the tokamak core, determining the overall performances of the machine.

In this Thesis, we present a first-principles self-consistent model suitable to simulate the coupled plasma turbulent and neutral dynamics in the tokamak periphery. The model, described in Chapter 2, assumes high plasma collisionality,  $\lambda_{\text{mfp}}/L \ll 1$ , magnetized plasma,  $\omega_c \tau \gg 1$ , drift ordering,  $d/dt \ll \omega_{\text{ci}}$ , adiabatic neutrals,  $\tau_n < \tau_{\text{turb}}$ , and elongated turbulent plasma structures,  $k_{\parallel} \lambda_{\text{mfp},n} \ll 1$ . The plasma is modeled by the drift-reduced two-fluid Braginskii equations, Eqs. (2.16)-(2.21), and the neutral physics is described by a kinetic equation with Krook operators for ionization, recombination, and charge-exchange processes, Eq. (2.1). The neutral kinetic equation is solved in the adiabatic limit using decoupled poloidal planes and a short cycle scheme. The kinetic equation is hereby reduced to a linear integral equation for the neutral density, Eq. (2.33). The solution of Eq. (2.33) enables the straightforward computation of the neutral distribution function,  $f_n$ , by evaluating Eq. (2.26), and any of its higher order moments, needed in the plasma-neutral interaction terms.

In Chapter 3, a simulation of the tokamak SOL and edge region is presented, where the plasma density source is solely described by the self-consistent ionization of neutral atoms. This simulation is then used as a basis to identify the key elements of the neutral-plasma interaction, with the goal of obtaining the simplest possible model for its description. In Section 3.3 part of the simulation is repeated with averaged neutral moments, showing that, in the presented plasma conditions, neutral fluctuations do not impact the equilibrium plasma profiles significantly. Zeroing out the terms

## Chapter 6. Summary and outlook

---

related to friction between the plasma species and the neutrals in Section 3.4.1, also results in very similar plasma profiles, confirming that these small terms do not impact the plasma profiles significantly in the considered plasma conditions. On the other hand, removing the interaction terms in the electron and ion temperature equations completely, as presented in Section 3.4.2, affects significantly the simulation. This points out that the temperature interaction terms, Eqs. (3.15) and (3.16), are important. Therefore, the simplest neutral model that can be used, in the plasma scenarios under consideration, includes the ionization term in the plasma density equation, the corresponding energy sink terms in the electron temperature equation, and the temperature equilibration terms related to ionization and charge exchange processes in the ion temperature equation.

A refined two-point model that includes plasma-neutral interactions is presented in Chapter 4. The model is derived from the drift-reduced Braginskii equations. It reproduces well the simulation results, as verified by a comparison with a set of self-consistent turbulence simulations of the tokamak SOL. Two conclusions can be drawn from the comparison. First, when considering simulations with short neutral mean free path, it is important to account for the plasma-neutral interaction terms and, second, throughout the parameter regime explored in the considered set of simulations, the compressional term has to be taken into account for good quantitative agreement. By taking into account these two effects, the refined two-point model that we derived from the drift-reduced Braginskii equations for the limited tokamak SOL predicts accurately the ratio between upstream and target electron temperatures along a flux tube given three input parameters, namely the particle and heat sources due to perpendicular turbulent transport, and the ionization in the flux tube. The refined two-point model can be used, in the parameter regime investigated through our simulations, to approximately predict the outcome of computationally expensive turbulence simulations, guiding the decision about input parameters of such simulations or experiments. As progress in the development of three-dimensional turbulence codes evolves, the two-point model can be further improved for more advanced tokamak exhaust configurations.

In Chapter 5, a self-consistent simulation of plasma turbulence and neutral atom dynamics in the SOL and edge regions of a limited tokamak is discussed. This simulation includes two fueling gas puffs on the high-field side and a diagnostic gas puff on the low-field side equatorial midplane. The local  $D_\alpha$  emission is evaluated and the effect of neutral density fluctuations on GPI measurements is investigated. It turns out that neutral density fluctuations and plasma fluctuations (for both plasma density and electron temperature) are strongly anti-correlated at distances from the gas puff smaller than the neutral mean free path,  $\lambda_{\text{mfp},n}$ , which leads to a systematic influence

---

of neutral density fluctuations on the  $D_\alpha$  emission amplitude. On the other hand, statistical moments and turbulence characteristics of the  $D_\alpha$  fluctuations, such as skewness, kurtosis, autocorrelation time, and perpendicular correlation lengths, are not affected significantly in this region, at least in the parameter regime investigated in the presented simulation. The assumption to neglect neutral fluctuations to interpret the characteristics of  $D_\alpha$  emission as being very similar to the characteristics of the plasma, which is often used to interpret experimental GPI measurements, is therefore justified at distances from the gas puff smaller than  $\lambda_{\text{mfp},n}$ . Particular care has to be taken in the analysis of GPI measurements, if regions closer to the core are included in the observations, where the neutrals have traversed distances longer than  $\lambda_{\text{mfp},n}$  from their source, the diagnostic gas puff. In these regions, in fact, the neutrals have interacted with plasma structures at different radial locations and the  $D_\alpha$  emission is strongly influenced by non-local shadowing events. This is particularly true for the skewness, kurtosis, autocorrelation time, and radial and poloidal correlation lengths, that are significantly affected by the neutral density fluctuations.

The inclusion of the kinetic neutral model into the drift-fluid plasma turbulence code GBS is a step in the path leading from the description of simple linear basic plasma physics experiments [77] to the completely self-consistent simulation of the complex processes in the periphery of a future fusion power plant. While in the present Thesis the focus lies on limited tokamaks, work is being carried out to enable the GBS code to simulate plasmas in arbitrary magnetic geometries, therefore allowing also diverted plasma configurations. Since in diverted configurations the strike points are far from the confined plasma region, neutral-plasma interactions are even more important than in limited plasmas. Simulating plasma turbulence and neutral atom dynamics self-consistently in diverted plasma configurations is one of the next steps for the GBS code. The initial work on the transition between a sheath limited to a conduction limited regime, presented in Section 2.6, can then be extended in future efforts towards the high-recycling and detached regimes, using divertor configurations. To fully self-consistently simulate the physical processes in the turbulent detached divertor, the neutral atom model most likely has to be extended to include molecular physics, the presence of impurities, and a model for power radiation.





# Bibliography

- [1] International Energy Agency. *World Energy Outlook 2016*. IEA Publications (2016).
- [2] A.J. Meadows. *Stellar Evolution*. Elsevier Science (2013).
- [3] F.F. Chen. *Introduction to Plasma Physics and Controlled Fusion*. Springer US (2013).
- [4] J.D. Lawson. Some Criteria for a Power Producing Thermonuclear Reactor. *Proceedings of the Physical Society. Section B* **70**, 6 (1957).
- [5] J. Wesson. *Tokamaks*. Oxford University Press (2011).
- [6] L. Spitzer. The Stellarator Concept. *Physics of Fluids* **1**, 253 (1958).
- [7] L. Spitzer. *Physics of Fully Ionized Gases*. Dover Publications (2006).
- [8] P. Stangeby. *The Plasma Boundary of Magnetic Fusion Devices*. IOP Publishing (2000).
- [9] Y. Gribov, D. Humphreys, K. Kajiwara, E.A. Lazarus, J.B. Lister, T. Ozeki, A. Portone, M. Shimada, A.C.C. Sips, and J.C. Wesley. Chapter 8: Plasma operation and control. *Nuclear Fusion* **47**, S385 (2007).
- [10] P. Ricci, F.D. Halpern, S. Jolliet, J. Loizu, A. Masetto, A. Fasoli, I. Furno, and C. Theiler. Simulation of plasma turbulence in scrape-off layer conditions: the GBS code, simulation results and code validation. *Plasma Physics and Controlled Fusion* **54**, 124047 (2012).
- [11] F.D. Halpern, P. Ricci, S. Jolliet, J. Loizu, J. Morales, A. Masetto, F. Musil, F. Riva, T.M. Tran, and C. Wersal. The GBS code for tokamak scrape-off layer simulations. *Journal of Computational Physics* **315**, 388 (2016).

## Bibliography

---

- [12] C. Wersal and P. Ricci. A first-principles self-consistent model of plasma turbulence and kinetic neutral dynamics in the tokamak scrape-off layer. *Nuclear Fusion* **55**, 123014 (2015).
- [13] S.I. Braginskii. Transport Processes in a Plasma. *Reviews of Plasma Physics* **1**, 205 (1965).
- [14] A. Zeiler, J.F. Drake, and B. Rogers. Nonlinear reduced Braginskii equations with ion thermal dynamics in toroidal plasma. *Physics of Plasmas* **4**, 2134 (1997).
- [15] J. Loizu. *The role of the sheath in magnetized plasma turbulence and flows*. Ph.D. thesis, École polytechnique fédérale de Lausanne EPFL, n° 5985 (2013).
- [16] A. Masetto. *Turbulent regimes in the tokamak scrape-off layer*. Ph.D. thesis, École polytechnique fédérale de Lausanne EPFL, n° 6197 (2014).
- [17] A. Loarte, B. Lipschultz, A.S. Kukushkin, G.F. Matthews, P.C. Stangeby, N. Asakura, G.F. Counsell, G. Federici, A. Kallenbach, K. Krieger, A. Mahdavi, V. Philipps, D. Reiter, J. Roth, J. Strachan, D. Whyte, R. Doerner, T. Eich, W. Fundamenski, A. Herrmann, M. Fenstermacher, P. Ghendrih, M. Groth, A. Kirschner, S. Konoshima, B. LaBombard, P. Lang, A.W. Leonard, P. Monier-Garbet, R. Neu, H. Pacher, B. Pegourie, R.A. Pitts, S. Takamura, J. Terry, E. Tsitrone, and the ITPA Scrape-off Layer and Divertor Physics Topical Group. Chapter 4: Power and particle control. *Nuclear Fusion* **47**, S203 (2007).
- [18] B. Lipschultz, X. Bonnin, G. Counsell, A. Kallenbach, A. Kukushkin, K. Krieger, A. Leonard, A. Loarte, R. Neu, R.A. Pitts, T. Rognlén, J. Roth, C. Skinner, J.L. Terry, E. Tsitrone, D. Whyte, S. Zweben, N. Asakura, D. Coster, R. Doerner, R. Dux, G. Federici, M. Fenstermacher, W. Fundamenski, P. Ghendrih, A. Herrmann, J. Hu, S. Krasheninnikov, G. Kirnev, A. Kreter, V. Kurnaev, B. LaBombard, S. Lisgo, T. Nakano, N. Ohno, H.D. Pacher, J. Paley, Y. Pan, G. Pautasso, V. Philipps, V. Rohde, D. Rudakov, P. Stangeby, S. Takamura, T. Tanabe, Y. Yang, and S. Zhu. Plasma–surface interaction, scrape-off layer and divertor physics: implications for ITER. *Nuclear Fusion* **47**, 1189 (2007).
- [19] D. Reiter *et al.* EIRENE - A Monte Carlo Linear Transport Solver. available on the Internet at <http://www.eirene.de> (2002-...).
- [20] D. Reiter, M. Baelmans, and P. Börner. The EIRENE and B2-EIRENE Codes. *Fusion Science and Technology* **47**, 172 (2005).
- [21] D. Stotler and C. Karney. Neutral Gas Transport Modeling with DEGAS 2. *Contributions to Plasma Physics* **34**, 392 (1994).

- [22] E. Cupini, A. De Matteis, and R. Simonini. NIMBUS-Monte Carlo Simulation of Neutral Particle Transport in Fusion Devices. *EUR XII-324/9 rep.* (1983).
- [23] H. Bufferand, B. Bensiali, J. Bucalossi, G. Ciraolo, P. Genesio, P. Ghendrih, Y. Marandet, A. Paredes, F. Schwander, E. Serre, and P. Tamain. Near wall plasma simulation using penalization technique with the transport code SOLEDGE2D-EIRENE. *Journal of Nuclear Materials* **438**, S445 (2013).
- [24] D. Reiter. Progress in two-dimensional plasma edge modelling. *Journal of Nuclear Materials* **196-198**, 80 (1992).
- [25] R. Schneider, D. Reiter, H.P. Zehrfeld, B. Braams, M. Baelmans, J. Geiger, H. Kastelewicz, J. Neuhauser, and R. Wunderlich. B2-EIRENE simulation of ASDEX and ASDEX-Upgrade scrape-off layer plasmas. *Journal of Nuclear Materials* **196-198**, 810 (1992).
- [26] Y. Feng, F. Sardei, J. Kisslinger, P. Grigull, K. McCormick, and D. Reiter. 3D Edge Modeling and Island Divertor Physics. *Contributions to Plasma Physics* **44**, 57 (2004).
- [27] T.D. Rognlien, J.L. Milovich, M.E. Rensink, and G.D. Porter. A fully implicit, time dependent 2-D fluid code for modeling tokamak edge plasmas. *Journal of Nuclear Materials* **196-198**, 347 (1992).
- [28] A.S. Kukushkin, H.D. Pacher, V. Kotov, G.W. Pacher, and D. Reiter. Finalizing the ITER divertor design: The key role of SOLPS modeling. *Fusion Engineering and Design* **86**, 2865 (2011).
- [29] M.V. Umansky, T.D. Rognlien, M.E. Fenstermacher, M. Borchardt, A. Mutzke, J. Riemann, R. Schneider, and L.W. Owen. Modeling of localized neutral particle sources in 3D edge plasmas. *Journal of Nuclear Materials* **313-316**, 559 (2003).
- [30] D.P. Coster, X. Bonnin, B. Braams, D. Reiter, R. Schneider, and the ASDEX Upgrade Team. Simulation of the Edge Plasma in Tokamaks. *Physica Scripta* page 7 (2004).
- [31] N. Horsten, W. Dekeyser, G. Samaey, and M. Baelmans. Assessment of fluid neutral models for a detached ITER case. *Nuclear Materials and Energy, in press* (2016).
- [32] B.D. Dudson, M.V. Umansky, X.Q. Xu, P.B. Snyder, and H.R. Wilson. BOUT++: A framework for parallel plasma fluid simulations. *Computer Physics Communications* **180**, 1467 (2009).

## Bibliography

---

- [33] P. Tamain, H. Bufferand, G. Ciraolo, C. Colin, D. Galassi, P. Ghendrih, F. Schwander, and E. Serre. The TOKAM3X code for edge turbulence fluid simulations of tokamak plasmas in versatile magnetic geometries. *Journal of Computational Physics* **321**, 606 (2016).
- [34] J.J. Rasmussen, A.H. Nielsen, J. Madsen, V. Naulin, and G.S. Xu. Numerical modeling of the transition from low to high confinement in magnetically confined plasma. *Plasma Physics and Controlled Fusion* **58**, 014031 (2015).
- [35] A. Stegmeir, D. Coster, O. Maj, K. Hallatschek, and K. Lackner. The field line map approach for simulations of magnetically confined plasmas. *Computer Physics Communications* **198**, 139 (2016).
- [36] Y. Marandet, P. Tamain, R. Futtersack, P. Ghendrih, H. Bufferand, P. Genesio, and A. Mekkaoui. Influence of neutral particles on scrape-off layer turbulence with application to the interpretation of fast camera data. *Journal of Nuclear Materials* **438**, S518 (2013).
- [37] N. Bisai, R. Jha, and P.K. Kaw. Role of neutral gas in scrape-off layer tokamak plasma. *Physics of Plasmas* **22**, 022517 (2015).
- [38] J. Leddy, B. Dudson, and H. Willett. Simulation of the interaction between plasma turbulence and neutrals in linear devices. *Nuclear Materials and Energy*, in press (2016).
- [39] A.S. Thrysoe, L.E.H. Tophøj, V. Naulin, J.J. Rasmussen, J. Madsen, and A.H. Nielsen. The influence of blobs on neutral particles in the scrape-off layer. *Plasma Physics and Controlled Fusion* **58**, 044010 (2016).
- [40] J. Loizu, P. Ricci, F.D. Halpern, and S. Jolliet. Boundary conditions for plasma fluid models at the magnetic presheath entrance. *Physics of Plasmas* **19**, 122307 (2012).
- [41] F.D. Halpern, S. Jolliet, J. Loizu, A. Masetto, and P. Ricci. Ideal ballooning modes in the tokamak scrape-off layer. *Physics of Plasmas* **20**, 052306 (2013).
- [42] H.P. Summers, W.J. Dickson, M.G. O’Mullane, N.R. Badnell, A.D. Whiteford, D.H. Brooks, J. Lang, S.D. Loch, and D.C. Griffin. Ionization state, excited populations and emission of impurities in dynamic finite density plasmas: I. The generalized collisional–radiative model for light elements. *Plasma Physics and Controlled Fusion* **48**, 263 (2006).
- [43] R.K. Janev. *Atomic and Molecular Processes in Fusion Edge Plasmas*. Plenum Press (1995).

- 
- [44] H. Bufferand, G. Ciraolo, Y. Marandet, J. Bucalossi, P. Ghendrih, J. Gunn, N. Mellet, P. Tamain, R. Leybros, N. Fedorczak, F. Schwander, and E. Serre. Numerical modelling for divertor design of the WEST device with a focus on plasma–wall interactions. *Nuclear Fusion* **55**, 053025 (2015).
- [45] M. Knudsen. Das Cosinusgesetz in der kinetischen Gastheorie. *Annalen der Physik* **353**, 1113 (1916).
- [46] R.K. Janev, W.D. Langer, D.E. Post, and K. Evans. *Elementary Processes in Hydrogen-Helium Plasmas*. Springer Nature (1987).
- [47] D.P. Stotler, B. LaBombard, J.L. Terry, and S.J. Zweben. Neutral transport simulations of gas puff imaging experiments. *Journal of Nuclear Materials* **313-316**, 1066 (2003).
- [48] P. Helander, S.I. Krasheninnikov, and P.J. Catto. Fluid equations for a partially ionized plasma. *Physics of Plasmas* **1**, 3174 (1994).
- [49] S. Jolliet, F.D. Halpern, J. Loizu, A. Masetto, and P. Ricci. Aspect ratio effects on limited scrape-off layer plasma turbulence. *Physics of Plasmas* **21**, 022303 (2014).
- [50] W. Fundamenski. Parallel heat flux limits in the tokamak scrape-off layer. *Plasma Physics and Controlled Fusion* **47**, R163 (2005).
- [51] P. Ricci and B.N. Rogers. Plasma turbulence in the scrape-off layer of tokamak devices. *Physics of Plasmas* **20**, 010702 (2013).
- [52] A. Masetto, F.D. Halpern, S. Jolliet, J. Loizu, and P. Ricci. Turbulent regimes in the tokamak scrape-off layer. *Physics of Plasmas* **20**, 092308 (2013).
- [53] J. Loizu, P. Ricci, F.D. Halpern, S. Jolliet, and A. Masetto. Intrinsic toroidal rotation in the scrape-off layer of tokamaks. *Physics of Plasmas* **21**, 062309 (2014).
- [54] F.D. Halpern, P. Ricci, S. Jolliet, J. Loizu, and A. Masetto. Theory of the scrape-off layer width in inner-wall limited tokamak plasmas. *Nuclear Fusion* **54**, 043003 (2014).
- [55] J. Loizu, P. Ricci, F.D. Halpern, S. Jolliet, and A. Masetto. On the electrostatic potential in the scrape-off layer of magnetic confinement devices. *Plasma Physics and Controlled Fusion* **55**, 124019 (2013).
- [56] B. LaBombard. *KN1D: A 1-D space, 2-D velocity, kinetic transport algorithm for atomic and molecular hydrogen in an ionizing plasma*. Plasma Science and Fusion Center, Massachusetts Institute of Technology. Report PSFC/RR-01-03 (2001).

## Bibliography

---

- [57] Y. Marandet, A. Mekkaoui, D. Reiter, P. Boerner, P. Genesio, F. Catoire, J. Rosato, H. Capes, L. Godbert-Mouret, M. Koubiti, and R. Stamm. Transport of neutral particles in turbulent scrape-off layer plasmas. *Nuclear Fusion* **51**, 083035 (2011).
- [58] A. Arakawa. Computational design for long-term numerical integration of the equations of fluid motion: Two-dimensional incompressible flow. Part I. *Journal of Computational Physics* **1**, 119 (1966).
- [59] M.W. Kutta. Beitrag zur näherungsweise Integration totaler Differentialgleichungen. *Zeitschrift für Mathematik und Physik* **46**, 435 (1901).
- [60] F. Riva, P. Ricci, F.D. Halpern, S. Jolliet, J. Loizu, and A. Masetto. Verification methodology for plasma simulations and application to a scrape-off layer turbulence code. *Physics of Plasmas* **21**, 062301 (2014).
- [61] A. Mekkaoui, Y. Marandet, D. Reiter, P. Boerner, P. Genesio, J. Rosato, H. Capes, M. Koubiti, L. Godbert-Mouret, and R. Stamm. A coarse-grained transport model for neutral particles in turbulent plasmas. *Physics of Plasmas* **19**, 122310 (2012).
- [62] F.D. Halpern and P. Ricci. Velocity shear, turbulent saturation, and steep plasma gradients in the scrape-off layer of inner-wall limited tokamaks. *Nuclear Fusion* **57**, 034001 (2016).
- [63] C. Wersal, P. Ricci, and J. Loizu. A comparison between a refined two-point model for the limited tokamak SOL and self-consistent plasma turbulence simulations. *Plasma Physics and Controlled Fusion* **59**, 044011 (2017).
- [64] P.C. Stangeby. A tutorial on some basic aspects of divertor physics. *Plasma Physics and Controlled Fusion* **42**, B271 (2000).
- [65] M.Z. Tokar, M. Kobayashi, and Y. Feng. Improved two-point model for limiter scrape-off layer. *Physics of Plasmas* **11**, 4610 (2004).
- [66] V. Kotov and D. Reiter. Two-point analysis of the numerical modelling of detached divertor plasmas. *Plasma Physics and Controlled Fusion* **51**, 115002 (2009).
- [67] J.L. Terry, R. Maqueda, C.S. Pitcher, S.J. Zweben, B. LaBombard, E.S. Marmor, A.Y. Pigarov, and G. Wurden. Visible imaging of turbulence in the SOL of the Alcator C-Mod tokamak. *Journal of Nuclear Materials* **290**, 757 (2001).
- [68] R.J. Maqueda, G.A. Wurden, S. Zweben, L. Roquemore, H. Kugel, D. Johnson, S. Kaye, S. Sabbagh, and R. Mainigi. Edge turbulence measurements in NSTX by gas puff imaging. *Review of Scientific Instruments* **72**, 931 (2001).

- [69] S.J. Zweben, D.P. Stotler, J.L. Terry, B. LaBombard, M. Greenwald, M. Muterspaugh, C.S. Pitcher, the Alcator C-Mod Group, K. Hallatschek, R.J. Maqueda, B. Rogers, J.L. Lowrance, V.J. Mastrocola, and G.F. Renda. Edge turbulence imaging in the Alcator C-Mod tokamak. *Physics of Plasmas* **9**, 1981 (2002).
- [70] I. Shesterikov, Y. Xu, M. Berte, P. Dumortier, M.V. Schoor, M. Vergote, B. Schweer, and G.V. Oost. Development of the gas-puff imaging diagnostic in the TEXTOR tokamak. *Review of Scientific Instruments* **84**, 053501 (2013).
- [71] S.J. Zweben, B.D. Scott, J.L. Terry, B. LaBombard, J.W. Hughes, and D.P. Stotler. Comparison of scrape-off layer turbulence in Alcator C-Mod with three dimensional gyrofluid computations. *Physics of Plasmas* **16**, 082505 (2009).
- [72] F.D. Halpern, J.L. Terry, S.J. Zweben, B. LaBombard, M. Podesta, and P. Ricci. Comparison of 3D flux-driven scrape-off layer turbulence simulations with gas-puff imaging of Alcator C-Mod inner-wall limited discharges. *Plasma Physics and Controlled Fusion* **57**, 054005 (2015).
- [73] D. Moulton, Y. Marandet, P. Tamain, P. Ghendrih, and R. Futtersack. Density and Temperature Correlations in the SOL; Implications for Gas Puff Imaging of Turbulence. *Contributions to Plasma Physics* **54**, 575 (2014).
- [74] E. de la Cal and The TJ-II Team. Visualising the electron density structure of blobs and studying its possible effect on neutral turbulence. *Nuclear Fusion* **56**, 106031 (2016).
- [75] D.A. Russell, J.R. Myra, D.A. D'Ippolito, T.L. Munsat, Y. Sechrest, R.J. Maqueda, D.P. Stotler, S.J. Zweben, and The NSTX Team. Comparison of scrape-off layer turbulence simulations with experiments using a synthetic gas puff imaging diagnostic. *Physics of Plasmas* **18**, 022306 (2011).
- [76] C. Spearman. The Proof and Measurement of Association between Two Things. *The American Journal of Psychology* **15**, 72 (1904).
- [77] B.N. Rogers and P. Ricci. Low-Frequency Turbulence in a Linear Magnetized Plasma. *Physical Review Letters* **104** (2010).





# Acknowledgements

First of all, I would like to thank my advisor Paolo Ricci. He guided me for four years through the field of plasma physics and the process of becoming a scientist. His door was always open to discuss my efforts and my problems, which he did with great enthusiasm. I, and this Thesis, benefitted a lot from his vast knowledge of the field, which he shared enthusiastically.

I would also like to thank my current and former colleagues in the edge plasma theory group. Fabio, with whom I shared the office for four years and who was always there for a quick question. Federico, who was not only the person to go to for code development, but who also shared his physics knowledge and understanding with me during plenty of discussions. And, in no particular order, Paola, Joaquim, Jorge, Annamaria, Sebastien, Rogério, Carrie, and André. You were great colleagues both inside and outside the realm of plasma physics.

Thanks goes also to all my other colleagues at the Swiss Plasma Center: doctoral students, postdocs, senior scientists, engineers, administrators, and everyone else that I forgot to list. It was a pleasure to work with you, to have lunch with you, to sail with some of you, and to spend time with you also outside the office.

I also thank my former teachers and mentors, who have always encouraged me and deepened my interest in the world of science. In particular, thank you Josephine Osterkamp, Wolfgang Ringowski, and Alberto Bottino.

Finally, I would like to thank my partner, my family, and my friends, without whom I wouldn't be where I am today.

*Lausanne, 15 May 2017*

Christoph Wersal



# Christoph Wersal

Date of birth: 10.03.1987

Email: christoph.wersal@epfl.ch



## Education

- 2013–2017 **PhD in Plasma Physics**, *Swiss Plasma Center, École Fédérale de Lausanne (EPFL)*, Switzerland.
- **Research** in the field of plasma physics and controlled fusion with turbulence simulations on high performance computers
  - **Teaching assistant** in the numerical physics course
  - **Supervision** of three master level student projects
- 2007–2012 **MSc in Physics (Diplom-Physiker)**, *Technische Universität München (TUM)*, Germany.
- **Major** in plasma physics and computational physics
  - **Erasmus semester** at the Royal Institute of Technology (KTH), Stockholm, Sweden, focusing on plasma physics, numerical methods, and renewable energy

## PhD thesis

- title *Neutral atom dynamics and plasma turbulence in the tokamak periphery*
- supervisor Prof. Paolo Ricci
- description Study on the interaction between neutral particles and turbulent plasma in the outermost region of a fusion device. A kinetic neutral atom model is developed and implemented in the plasma turbulence code GBS. The analysis of self-consistent simulations provides insights into the physics at play.

## Master thesis

- title *Spectral and spatial diagnostics on fluid moments in global particle-in-cell simulations*
- supervisors Prof. Sibylle Günter, Dr. Alberto Bottino
- description A set of three-dimensional diagnostics for gyrokinetic particle-in-cell simulations is developed and applied to the core region of fusion devices. Numerical investigations are carried out on the convergence properties of plasma turbulence simulations.

## Other Research Experience

- 2011 **Working student**, *Max-Planck-Institut for Plasma Physics*, Munich, Germany.  
Characterization and initial operation of a room temperature solid state pellet injector for fusion experiments.  
**Acquired skills:** vacuum systems, Siemens Simatic
- 2010 **Working student**, *TUM: Physics of Hadrons and Nuclei*, Munich, Germany.  
Redesigning and manufacturing of a circuit board for a detector's pre-amplifier.  
**Acquired skills:** circuit board design with EAGLE
- 2009 **Working student**, *TUM: Energy Conversion and Storage*, Munich, Germany.  
Investigation of hydrogen diffusion around the electrodes of a fuel cell by electrochemical experiments and Monte Carlo simulations.  
**Acquired skills:** electrochemistry, scanning tunneling microscopy, Visual Basic, Origin

## Languages

German **native**  
English **fluent**  
French **basic**

## Computer Skills

Programming Fortran, Matlab, Python, basic knowledge of C/C++, Java, PHP, SQL  
Parallelization MPI, OpenMP, OpenACC  
Others HPC, Linux, Windows, Servers, Office, LaTeX, Git

## Peer-reviewed publications

C. Wersal and P. Ricci. Impact of neutral density fluctuations on gas puff imaging diagnostics. *submitted to Nuclear Fusion* (2017).

C. Wersal, P. Ricci, and J. Loizu. A comparison between a refined two-point model for the limited tokamak SOL and self-consistent plasma turbulence simulations. *Plasma Physics and Controlled Fusion* **59**, 044011 (2017).

F.D. Halpern, P. Ricci, S. Jolliet, J. Loizu, J. Morales, A. Masetto, F. Musil, F. Riva, T.M. Tran, and C. Wersal. The GBS code for tokamak scrape-off layer simulations. *Journal of Computational Physics* **315**, 388 (2016).

C. Wersal and P. Ricci. A first-principles self-consistent model of plasma turbulence and kinetic neutral dynamics in the tokamak scrape-off layer. *Nuclear Fusion* **55**, 123014 (2015).

C. Wersal, A. Bottino, P. Angelino, and B.D. Scott. Fluid moments and spectral diagnostics in global particle-in-cell simulations. *Journal of Physics: Conference Series* **401**, 012025 (2012).

## Conference contributions (as first author)

C. Wersal, P. Ricci, R. Jorge, J. Morales, P. Paruta, and F. Riva. Interaction of neutral atoms and plasma turbulence in the tokamak edge region. *Poster*

*presentation at the 58th Annual Meeting of the APS Division of Plasma Physics. San Jose, CA, 2016.*

C. Wersal, P. Ricci, F. Halpern, R. Jorge, J. Morales, P. Paruta, and F. Riva. Impact of neutral atoms on plasma turbulence in the tokamak edge region. *Invited talk at the Theory of Fusion Plasma Joint Varenna-Lausanne International Workshop. Varenna, Italy, 2016.*

C. Wersal, T.M. Tran, P. Emonts, F.D. Halpern, R. Jorge, J. Morales, P. Paruta, P. Ricci, and F. Riva. Parallelization on a Hybrid Architecture of GBS, a Simulation Code for Plasma Turbulence at the Edge of Fusion Devices. *Poster presentation at the Platform for Advanced Scientific Computing Conference. Lausanne, Switzerland, 2016.*

C. Wersal, P. Ricci, F.D. Halpern, and F. Riva. The interaction between neutral particles and turbulent plasma in the tokamak SOL. *Poster presentation at the 42nd European Physical Society Conference on Plasma Physics. Lisbon, Portugal, 2015.*

C. Wersal, P. Ricci, F.D. Halpern, and F. Riva. A kinetic neutral atom model for tokamak SOL turbulence simulations. *Poster presentation at the Theory of Fusion Plasma Joint Varenna-Lausanne International Workshop. Varenna, Italy, 2014.*

C. Wersal, P. Ricci, F.D. Halpern, and F. Riva. A kinetic neutral atom model for tokamak scrape-off layer turbulence simulations. *Oral presentation at the SPS Annual Meeting. Fribourg, Switzerland, 2014.*